NOAA Technical Report NESDIS 152

DOI: 10.25923/scyb-qf42

Report for
Dedicated JPSS VIIRS Ocean Color Calibration/Validation Cruise
May 2018

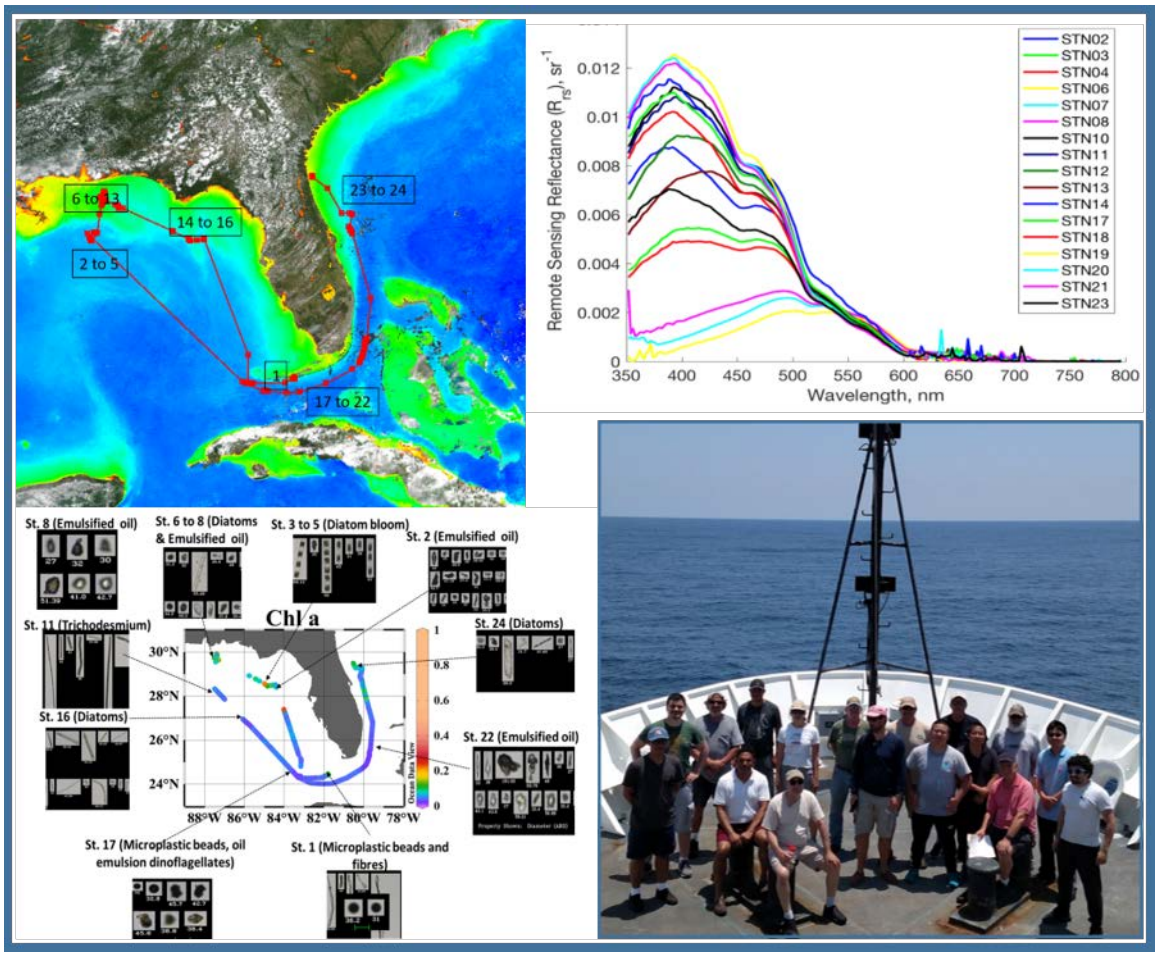

Washington, D.C.
May 2019

US DEPARTMENT OF COMMERCE
National Oceanic and Atmospheric Administration
National Environmental Satellite, Data, and Information Service

NOAA TECHNICAL REPORTS
National Environmental Satellite, Data, and Information Service

The National Environmental Satellite, Data, and Information Service (NESDIS) manages the Nation's civil Earth-observing satellite systems, as well as global national data bases for meteorology, oceanography, geophysics, and solar-terrestrial sciences. From these sources, it develops and disseminates environmental data and information products critical to the protection of life and property, national defense, the national economy, energy development and distribution, global food supplies, and the development of natural resources.

Publication in the NOAA Technical Report series does not preclude later publication in scientific journals in expanded or modified form. The NESDIS series of NOAA Technical Reports is a continuation of the former NESS and EDIS series of NOAA Technical Reports and the NESC and EDS series of Environmental Science Services Administration (ESSA) Technical Reports.

Copies of other NESDIS Technical reports may be available by contacting NESDIS Chief of Staff, NOAA/ NESDIS, 1335 East-West Highway, SSMC1, Silver Spring, MD 20910, (301) 713-3578.

Previous NESDIS Technical Reports on the Dedicated JPSS-VIIRS-Ocean Color Calibration/Validation Cruise Series:

Report #146	**November 2014**	**doi:10.7289/V52B8W0Z**
Report #148	**December 2015**	**doi:10.7289/V5/TR-NESDIS-148**
Report #151	**October 2016**	**doi: 10.7289/V5/TR-NESDIS-151**

*Cover image: (Clockwise from top left): 1) Cruise track and stations overlaid onto VIIRS SNPP chlorophyll-*a* temporally binned for the month of May 2018 (see Figure 2); 2) representative remote sensing reflectance spectra for all stations (see Figure 53); 3) Photo of scientific crew; 4) representative images of phytoplankton types at stations and underway chlorophyll-*a* (see Figure 29).

NOAA Technical Report NESDIS 152

DOI: 10.25923/scyb-qf42

Report for Dedicated JPSS VIIRS Ocean Color Calibration/Validation Cruise May 2018

Edited by Veronica P. Lance[1,2*]
[1]NOAA/NESDIS Center for Satellite Applications and Research (STAR), 5830 University Research Court, College Park, MD 20740, USA
[2]Earth System Science Interdisciplinary Center/Cooperative Institute for Climate and Satellites-Maryland, University of Maryland, College Park, MD 20740, USA

*Corresponding author: veronica.lance@noaa.gov

Contributing authors:

Michael Ondrusek[1]*, Veronica P. Lance[1,2], Menghua Wang[1], Eric Stengel[1], Charles Kovach[1,3],
[1]NOAA/NESDIS Center for Satellite Applications and Research (STAR), 5830 University Research Court, College Park, MD 20740, USA
[2]Earth System Science Interdisciplinary Center/Cooperative Institute for Climate and Satellites-Maryland, University of Maryland, College Park, MD 20740, USA
[3]Global Science and Technology, Inc., 7855 Walker Drive, Suite 200, Greenbelt, MD 20770, USA
*michael.ondrusek@noaa.gov

And (alphabetical by group lead last name):

Robert Arnone[1]*, Sherwin Ladner[2], Wesley Goode[2]
[1]University of Southern Mississippi, Stennis Space Center, MS 39529, USA
[2]Naval Research Laboratory, Stennis Space Center, MS 39529, USA
*robert.arnone@usm.edu

Alex Gilerson*, Ahmed El-Habashi, Carlos Carrizo, Eder Herrera, Sam Ahmed
City College of the City University of New York, 160 Convent Ave, New York, NY 10031, USA
*gilerson@ccny.cuny.edu

Joaquim I. Goes*, Helga do Rosario Gomes, Kali McKee
Lamont Doherty Earth Observatory at Columbia University, 61 Route 9W, Palisades, NY, 10964, USA
*jig@ldeo.columbia.edu

Chuanmin Hu*, Jennifer Cannizzaro, Yingjun Zhang, Chih-Wei Huang, David English
College of Marine Science, University of South Florida, 140 7th Avenue South, St. Petersburg, FL 33701, USA
*huc@usf.edu

B. Carol Johnson
National Institute of Standards and Technology, Physical Measurement Laboratory,100 Bureau Drive, Stop 8441, Gaithersburg, MD 20899-8441, USA
*carol.johnson@nist.gov

Zhongping Lee*, Xiaolong Yu, Zhehai Shang
School for the Environment, University of Massachusetts Boston, 100 Morrissey Blvd, Boston, MA 02125, USA
*zhongping.lee@umb.edu

Nicholas Tufillaro*[1], Ivan Lalovic[2]
[1] College of Earth, Ocean and Atmospheric Sciences, Oregon State University, Corvallis, OR 97331, USA
[2] GYBE LLC
*nbt@coas.oregonstate.edu

Kenneth J. Voss
Department of Physics, University of Miami, Knight Physics Building, Coral Gables, FL 33124, USA
*voss@physics.miami.edu

*Group corresponding contact

Washington, DC
May 2019

US DEPARTMENT OF COMMERCE
Wilbur Ross, Secretary

National Oceanic and Atmospheric Administration
Dr. Neil Jacobs, Assistant Secretary of Commerce for Oceans and Atmosphere and Performing the Duties of Under Secretary of Commerce for Oceans and Atmosphere

National Environmental Satellite, Data, and Information Service
Dr. Stephen Volz, Assistant Administrator

Contents

List of Figures

List of Tables

List of Equations

Preface

We are pleased to report that the fourth National Oceanic and Atmospheric Administration (NOAA) dedicated calibration and validation (Cal/Val) cruise on the NOAA Ship *Okeanos Explorer* has been successfully carried out from 9 May to 18 May 2018. Nine research groups with 17 investigators participated the cruise. This report provides details about activities and measurement procedures in the May 2018 Cal/Val cruise.

The Ocean Color Team at the NOAA Center for Satellite Applications and Research (STAR) is focused on "end-to-end" production of high quality satellite ocean color products. In situ validation of satellite data is essential to produce the high quality, fit-for-purpose remotely sensed ocean color products that are required and expected by all NOAA line offices, as well as by external (both applied and research) users. In addition to serving the needs of its diverse users within the US, NOAA has an ever-increasing role in supporting the international ocean color community and is actively engaged in the International Ocean-Colour Coordinating Group (IOCCG).

NOAA/STAR scientists have been acquiring in situ data throughout all of the ocean color satellite missions. Since the launch in October 2011 of the Visible Infrared Imaging Radiometer Suite (VIIRS) aboard the Suomi National Polar-orbiting Partnership (SNPP) platform, part of the US Joint Polar Satellite System (JPSS) program, the NOAA/STAR Ocean Color Team has been making in situ measurements routinely in support of validation and algorithm development activities. The second VIIRS sensor onboard the NOAA-20 satellite was successfully launched in November 2017. To date, four Dedicated JPSS VIIRS Ocean Color Calibration/Validation (Cal/Val) Cruises have been conducted, supported by: 1) NOAA Office of Marine and Aviation Operations (OMAO) for ship time, 2) the JPSS program for funding many of the participating groups and 3) NOAA/NESDIS/STAR. The first three cruises off the US mid-Atlantic and southeast coasts were in November 2014, December 2015 and October 2016 as detailed in NESDIS Technical Report #146, Report #148, and Report #151, respectively. This report covers the fourth dedicated VIIRS Cal/Val cruise in May 2018. The fifth dedicated VIIRS Cal/Val cruise is planned for September 2019.

These annual dedicated ocean color validation field campaigns provide in situ measurements needed to produce the best quality, fit-for-purpose ocean color remote sensing data and data products for NOAA applications and for users beyond NOAA. These observations support validation activities for the current JPSS VIIRS sensors on SNPP and NOAA-20 satellites, which are now the primary sources for NOAA operational remotely sensed ocean color data products. Future cruises will support VIIRS on all the JPSS platforms as well as non-NOAA US (e.g., National Aeronautics and Space Administration (NASA) and United States Geological Survey (USGS)) and international ocean color related satellite missions (e.g., the Ocean and Land Colour Instrument (OLCI) aboard Sentinel-3 of the European Union's Copernicus mission and the Second Generation Global Imager (SGLI) aboard Global Climate Observation Mission-Climate (GCOM-C) mission from the Japan Aerospace Exploration Agency). Through the NOAA mission of science, service and stewardship, and in collaboration with the international ocean community, we aim to provide ocean satellite data products that improve our understanding of global and coastal ocean and inland water optical, biological, and biogeochemical properties and that support applications to benefit society.

Menghua Wang
Chief, Marine Ecosystems & Climate Branch; VIIRS Ocean Color Cal/Val Team Lead; NOAA Representative to the IOCCG
Paul DiGiacomo
Chief, Satellite Oceanography & Climatology Division; OCR-VC Co-Chair

NOAA Technical Report NESDIS 152
Report for
Dedicated JPSS VIIRS Ocean Color Calibration/Validation Cruise
May 2018

1 Overview and Summary of Purpose, Project, Principal Investigators and Participants

The overall aim of the annual NOAA Dedicated JPSS VIIRS Ocean Color Calibration/Validation (Cal/Val) Cruises [Ondrusek et al., 2017; Ondrusek et al., 2016; Ondrusek et al., 2015] is to support improvements in the extent and accuracy of satellite remotely sensed ocean color parameters in the near surface ocean. The primary objective of these cruises is to collect high quality in situ optical and related biological and biogeochemical data for the purpose of validating satellite ocean color radiometry and derived products from VIIRS on SNPP [Wang et al., 2017; Wang et al., 2014; Wang et al., 2013], NOAA-20 and the follow-on JPSS missions. The second objective is to quantify the confidence intervals of optical measurement protocols. The third objective is to characterize the optical signatures of a variety of water masses (i.e., coastal, near-shore, cross-shelf, eddies, fronts, filaments, blue water, etc.).

The NOAA Office of Marine and Aviation Operations (OMAO) allocated ship time for the 2018 cruise aboard the NOAA Ship *Okeanos Explorer* (OMAO cruise identification #EX-18-04). The plan allowed for 10 days at sea, departing 9 May 2018 from Key West, Florida and returning to Jacksonville, Florida on 18 May 2018. Overall, 24 stations were occupied in a variety of water types during the cruise, including oligotrophic and near-shore waters in the Gulf of Mexico, the Florida Straits and in the coastal Atlantic. Despite a cloud system that covered most of Florida's coasts, strategic planning around weather forecasts, enabled satellite validation matchups with VIIRS overpasses at likely 18 of 24 stations.

Nine research groups participated in the cruise. Most of the principle investigators were funded partly through JPSS program with some additional financial support provided by NOAA/STAR Satellite Oceanography and Climatology Division (SOCD) research funds. Table 1 lists the principal investigators, the associated institutions and abbreviations for the groups. These abbreviations will be used throughout this report. Seventeen scientists (Table 2) including seven PhD students, sailed and conducted measurements with the support of officers and crew of the *Okeanos Explorer*. In addition to onboard activities, optical instruments were calibrated before and after the cruise at the NOAA/STAR optical laboratory in College Park, MD. The NOAA/STAR optical laboratory maintains an ongoing collaboration with NIST to validate the NOAA/STAR radiometric scales in support of cruise activities, and to provide traceable calibration services. NIST also provided a reference plaque currently in development (known as the "blue tile") which was used in the field for instrument inter-comparison exercises.

All results shown in this report should be considered preliminary and are included here to illustrate examples of measurements and observations. Post-processing and sample analyses are on-going. Results are expected to be published as peer-reviewed literature in scientific journals as work is completed. The cruise dataset will be formally archived through NOAA/NESDIS National Centers for Environmental Information (NCEI) as required by NOAA. Cruise data will also be available to the ocean community through NOAA CoastWatch/OceanWatch.

Table 1. Principal investigators (PIs), participating institutions and institution abbreviations.

PI Name (Last, First)	Participating Institutions	Research Group Abbreviation
Arnone, Robert	University of Southern Mississippi (USM) and Naval Research Center (NRL)	Stennis
Gilerson, Alex	City College of New York	CCNY
Goes, Joaquim	Lamont-Doherty Earth Observatory at Columbia University	LDEO
Hu, Chuanmin	University of South Florida	USF
Johnson, B. Carol	National Institute of Standards and Technology	NIST
Lee, ZhongPing	University of Massachusetts, Boston	UMB
Ondrusek, Michael*	NOAA/NESDIS/Center for Satellite Applications and Research	NOAA/STAR
Tufillaro, Nicholas	Oregon State University	OSU
Voss, Kenneth	University of Miami	U. Miami

*Chief Scientist

Table 2. List of science party personnel aboard the NOAA Ship *Okeanos Explorer* (alphabetical order).

Name (Last, First)	Title	Research Group/Home Institution*
Arnone, Robert	Research Professor	Stennis/USM
Carrizo, Carlos	Student	CCNY
Goes, Joaquim	Professor	LDEO
Goode, Wesley	Researcher	Stennis/NRL
el Habashi, Ahmed	Student	CCNY
Herrera, Eder	Student	CCNY
Huang, Chih-Wei	Student	USF
Johnson, Carol	Researcher	NIST
Kovach, Charles	Researcher	NOAA
Ladner, Sherwin	Researcher	Stennis/NRL
Lalovic, Ivan	Researcher	OSU
Ondrusek, Michael	Chief Scientist	NOAA/STAR
Shang, Zhehai	Student	UMB
Stengel, Eric	Researcher	NOAA/STAR
Tufillaro, Nick	Researcher	OSU
Yu, Xiaolong	Student	UMB
Zhang, Yingiun	Student	USF

*See Table 1 for institution abbreviations.

2 Introduction

NOAA has been supporting satellite ocean color validation and calibration since the development and launch of the Coastal Zone Color Scanner (CZCS) [Gordon et al., 1980; Hovis et al., 1980] in the late 1970's and was instrumental in the development of the Marine Optical BuoY (MOBY) [Clark et al., 1997] in the Sea-viewing Wide Field-of-view Sensor (SeaWiFS) era [Gordon, 2010]. MOBY, now supported by NOAA, is the primary vicarious calibration reference standard for satellite ocean color sensors worldwide. In addition to high quality satellite sensor and vicarious calibrations from MOBY, in situ radiometric measurements from a variety of ocean optical conditions are essential to the production of accurate remotely sensed ocean color products.

The JPSS VIIRS-SNPP satellite ocean color Cal/Val science plan calls for in situ observations for developing and validating ocean color Environmental Data Records (EDRs) for global and coastal regions. Since 2014, the NOAA/STAR ocean color group has been conducting annual dedicated NOAA VIIRS Ocean Color Cal/Val Cruises [Ondrusek et al., 2017; Ondrusek et al., 2016; Ondrusek et al., 2015] to validate VIIRS satellite ocean color data [Arnone et al., 2014; Arnone et al., 2012; Wang et al., 2014; Wang et al., 2013], quantify the variability of in situ measurements and study the optical signatures of oceanic processes.

To date, four dedicated VIIRS validation cruises have been conducted. The first three cruises were aboard the NOAA Ship *Nancy Foster* and were staged from Charleston, SC. The first (OMAO cruise identification NF-14-09) took place in November 2014 along the US Mid-Atlantic Coast and across the Gulf Stream [Ondrusek et al., 2015]. The second (NF-15-13) was during December 2015 also along the US Mid-Atlantic Coast and across the Gulf Stream and included some stations in the Tongue of the Ocean (Bahamian waters) [Ondrusek et al., 2016]. The third (NF-16-08), was during October 2016, and took place off the coast of Charleston directly following Hurricane Mathew [Ondrusek et al., 2017]. The fourth cruise in May 2018 is the subject of this report.

3 Cruise Objectives

Shipboard observations of apparent optical properties (AOPs, i.e., radiances) and inherent optical properties (IOPs, e.g., absorption, beam attenuation and backscattering) as well as biological and biogeochemical measurements support three major objectives: 1) the validation of the VIIRS ocean color observations and derived products; 2) the characterization of the sources of uncertainty of in situ ocean color (remote sensing reflectance and IOPs) associated with nearly concurrent measurements by a variety of instruments and protocols; and 3) the characterization of optical properties of ocean variability (i.e., coastal, near-shore, cross-shelf, eddies, fronts, filaments, blue water) toward the future aim of using remotely sensed satellite ocean color data to monitor and study various ocean processes. Objectives are briefly discussed below. Greater detail can be found in earlier cruise reports [Ondrusek et al., 2017; Ondrusek et al., 2016; Ondrusek et al., 2015].

1) Validate VIIRS ocean color satellite remote sensing

Satellite sensor performance is evaluated, or validated, by matching up satellite observations with in situ observations, which are considered as the "true" values for this purpose. The primary properties derived from ocean color satellite observations are AOPs including spectral normalized water-leaving radiance ($nL_w(\lambda)$) and spectral remote sensing reflectance ($R_{rs}(\lambda)$), where λ represents the specified nominal center wavelength being measured. Therefore, in situ measurements for satellite validation are focused primarily on these AOP radiometric properties. By applying algorithms to $nL_w(\lambda)$ spectra, other satellite ocean color remote sensing products can be estimated. Products including the concentration of chlorophyll-*a* (Chl-*a*) and IOPs such as coefficients of spectral absorption ($a(\lambda)$), scattering ($b(\lambda)$), backscattering ($bb(\lambda)$) and beam attenuation ($c(\lambda)$) are also validated using the in situ measurements of these parameters. The sub-pixel variability of the IOP within VIIRS satellite pixels is examined using continuous flow-through measurements to validate satellite ocean color.

2) Characterize and quantify sources of uncertainty associated with in situ ocean color measurements

Sources of uncertainty for in situ measurements include errors associated with instruments, deployment and processing protocol differences and variances associated with the variability of the natural environment. Laboratory calibration of instruments (measurement conditions of repeatability [GUM, 1995]) and shipboard experiments (measurements conditions of reproducibility [GUM, 1995]) were conducted to quantify these differences [Johnson et al., 2014]. The following approaches, which represent conditions of reproducibility, were used to quantify measurement differences associated with: a) parallel observations from multiple instruments of the same or similar models deployed at the same time and in a

small spatial range (within meters of each other); b) observations of the same in situ parameters by using different types of instruments (i.e., profiling in-water versus above-water versus hybrid floating instruments); c) different deployment protocols for sample collection; d) different post-processing methods for the in situ data; and e) observations made under different environmental conditions (i.e., stations in different water masses and sky conditions).

3) Characterize the optical properties of dynamic ocean processes
The third objective of this cruise is to observe in situ optical characteristics of ocean variability related to dynamic processes in the open ocean and coastal waters for exploring the utility of VIIRS ocean color satellite products in identifying and monitoring oceanographic processes from space. The cruise data will be used to evaluate and demonstrate the ability of VIIRS ocean color products to differentiate the variations of spectral features produced by physical and biological states and processes.

4 Cruise Track, Overall Conditions and JPSS VIIRS Coverage

The *Okeanos Explorer* departed from Key West, Florida on 9 May 2018. The sampling plan and cruise track were dictated in response to cloud cover expectations. Sampling was conducted along the west coast of Florida, the offshore oligotrophic waters in the Gulf of Mexico and along Florida's Atlantic coast ending in Jacksonville, Florida on 18 May 2018. The original 10-day cruise plan included making measurements in the Bahamian waters of the Tongue of the Ocean but due to on-going operations by the United States Navy's Atlantic Undersea Test and Evaluation Center (AUTEC), sampling in that area during those dates was not permitted.

The initial checkout station (Station 1) was conducted south of Key West on 9 May. Because weather forecasts showed that the entire southern two-thirds of coastal Florida would be engulfed in clouds for the next week, the decision was made to transit during 10 May to the northeast Gulf of Mexico which was predicted to be cloud free (Figure 1). Stations 2 through 5 were sampled on 11 May west-northwest of Tampa Bay and south of Tallahassee near the Florida Middle Grounds in near-shore waters where a phytoplankton bloom, predominately diatoms (preliminary results suggest the species *Odontella sinensis*) was occurring. A cloud bank covering the coast of Florida encroached from the east, forcing sampling of Stations 6 through 9 on 12 May to the northeast in coastal waters influenced by the Mississippi River plume. Due to time constraints, the ship then headed south toward Key West for the transit back to Jacksonville. Stations 10 to 13 were occupied on 13 May approximately 75 nautical miles to the south-southwest near the vicinity of the Deepwater Horizon oil spill in oligotrophic, blue water. Stations 14 through 16 were sampled to the southeast on 14 May near the northeast corner of the Loop Current. Skies remained mostly clear with just some scattered clouds during these three days. Stations 17 and 18 on 15 May were in cloudy conditions covering the Loop Current Eddy and west of the Florida Keys. Stations 19 to 22 were sampled during the transit around Florida just south of Miami in mixed skies on 16 May. The ship then followed the Gulf Stream north in the Western Atlantic. Finally, Stations 23 and 24 were occupied on the 17 May off the coast of Jacksonville before heading to port on the morning of 18 May. Figure 2 shows the cruise track and approximate station locations overlaid on VIIRS SNPP satellite chlorophyll monthly merged data for May 2018.

Observations by the VIIRS sensors aboard the JPSS polar-orbiting satellites SNPP and NOAA-20 occur daily, crossing the equator at local time of approximately 13:30 and crossing the cruise region approximately 2 h earlier. The orbit patterns of each satellite provide the opportunity for occasional overlapping of coverage at a particular location. With both SNPP and NOAA-20 flying, between two and four overpasses per day at a given location are possible. Not every overpass will result in an ocean color observation mainly due to clouds, sunglint or high sensor-zenith angle [Mikelsons and Wang, 2019]. Out of the 24 stations, at least 18 stations had at least one good observation from a VIIRS sensor qualifying as

a “matchup”. Satellite overlaps occurred for SNPP on 11 May and 17 May and for NOAA-20 on 9 May, 13 May and 14 May. See Table 3 for tabulated station information.

Figure 1. True color imagery of the Gulf of Mexico from May 12, 2018 showing the extent of the cloud cover over Florida. On this day we were sampling in the clear region in the northeast Gulf of Mexico. This is a VIIRS SNPP true color image taken from NOAA/STAR Ocean Color team’s viewing and monitoring tool, “OCView”: (https://www.star.nesdis.noaa.gov/sod/mecb/color/ocview/ocview.html).

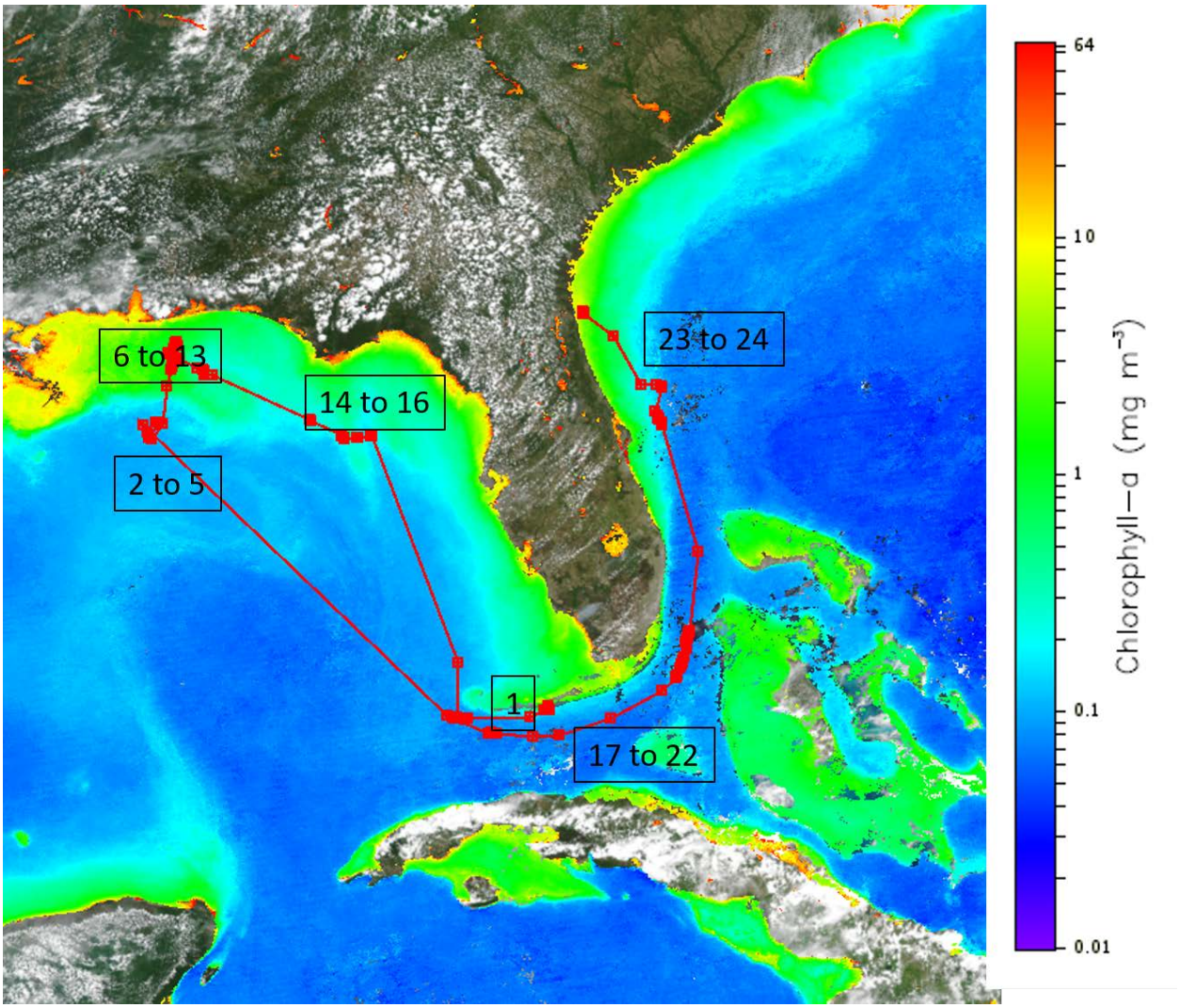

Figure 2. Cruise track and general station locations (station numbers in boxes) overlaid onto an image of VIIRS MSL12 Science Quality Chl-*a* merged for the month of May 2018.

Table 3. Station identification numbers, dates, times, locations and nominal description. All matchups listed in this table are preliminary and correspond with the HyperPro profiling observations. Matchup criteria are discussed in Section 10.

EX-18-04 Station ID#	Date in May 2018	Day of Year	Start Time UTC	Start Latitude ° N	Start Longitude °E	End Time UTC	End Latitude °N	End Longitude °E	SNPP Matchups [*n*]	NOAA-20 Matchups [*n*]	Station Description
1	9	129	1814	24.409	-81.800	2210	24.414	-81.800	x		Checkout station in Key West offshore waters at Gulf Stream's edge
2	11	131	1316	28.521	-84.442	1445	28.519	-84.462	x	x	Coastal waters across northern Gulf of Mexico shelf break
3	11	131	1606	28.492	-84.651	1740	28.490	-84.673	x	x	
4	11	131	1900	28.466	-84.856	2030	28.492	-84.855	x	x	
5	11	131	2125	28.519	-84.915	2130	28.528	-84.912	x	x	
6	12	132	1252	29.671	-87.349	1445	29.667	-87.352	x	x	Coastal waters across river plumes in northern Gulf of Mexico
7	12	132	1553	29.747	-87.498	1736	29.742	-87.517	x	x	
8	12	132	1855	29.859	-87.368	2106	29.886	-87.398	x	x	
9	12	132	2141	29.927	-87.388	2205	29.923	-87.391	x	x	
10	13	133	1230	28.685	-87.880	1412	28.693	-87.879	x	x	Offshore waters near the BP Deep Water Horizon oil spill site.
11	13	133	1520	28.568	-87.753	1713	28.569	-87.751	x	x	
12	13	133	1822	28.455	-87.641	2000	28.476	-87.661	x	x	
13	13	133	2043	28.401	-87.580	2128	28.394	-87.579	x	x	
14	14	134	1240	26.988	-86.112	1420	26.995	-86.129	x	x	Offshore waters at Loop Current Eddy
15	14	134	1600	26.866	-85.972	1735	26.878	-85.979	x	x	
16	14	134	1901	26.731	-85.813	1931	26.731	-85.800	x	x	
17	15	135	1402	24.544	-83.541	1554	24.578	-83.559		x	Offshore waters at Loop Current Edge and including a Gulf Stream Eddy
18	15	135	1804	24.371	-83.362	1912	24.391	-83.337			
19	16	136	1305	24.878	-79.891	1430	24.904	-79.875			Offshore waters along the western Atlantic Gulf Stream
20	16	136	1535	25.093	-79.794	1640	25.136	-79.783	x		
21	16	136	1802	25.336	-79.717	1920	25.400	-79.728	x		
22	16	136	2022	25.509	-79.697	2120	25.552	-79.693	x		
23	17	137	1358	28.762	-80.133	1524	28.800	-80.155			Near the Gulf Stream and in coastal waters near Jacksonville, Florida
24	17	137	1756	29.244	-80.090	1900	29.245	-80.100			

5 Sampling Strategies

At each station, simultaneous measurements were made with a suite of radiometric instruments to enable comparisons among the most widely utilized validation measurement techniques, including in-water profiling and floating radiometers and handheld above-water radiometers. Optical properties were also surveyed continuously while underway by instruments plumbed into the ship's flow-through sea water system and other instruments mounted on telescoping poles the side (mid to aft) rail of the ship. Additionally, water samples were collected at stations and from the flow-through sea water system for biogeochemical analyses of several environmental properties. More details regarding measurements follow in Section 6 and in the individual reports on each group's activities in Section 11.

Discrete Station Activities

Discrete stations, where the ship maintains a relatively stable location for the period of time it takes to execute measurements, were conducted daily, weather conditions permitting, during daylight hours between ≈0900 EDT and ≈1700 EDT local time (between ≈1300 UTC and ≈2100 UTC). A total of 24 stations were occupied over the course of the 10 days at sea with likely18 of those resulting in match-ups with VIIRS satellite observations. Generally, several activities, listed below, took place at each station,

- Profiling instrument packages that measured continuously and/or at discrete depths vertically through the water column, generally within the first 2 optical depths or to the physical mixed layer
- Floating instrument packages configured to float at the water's surface
- Above water instruments deployed by hand on deck
- Conductivity Temperature Depth (CTD)/Rosette package that collected water samples into 12 Niskin bottles (5 L), usually from two discrete depths, nominally one near surface and a second near the chlorophyll maximum depth within the first optical depth. The CTD instruments collect profile data as well.
- Deck mounted instruments and instruments plumbed into ships flow-through system collected surface measurements continuously while on station as well as underway.

Underway and Flow-Through Sampling

A series of bio-optical and hydrographic instruments for continuous (underway and during station operations) sampling were mounted on deck and also plumbed into the ship's sea water flow-through system. The sea chest intake was at a depth of 3 m. Observational data were synchronized with time and location and were monitored in real time for determining station locations. The flow-through data will also be used for spatial variability analyses.

6 Observations and Measured Parameters

6.1 Introduction to Observations and Measured Parameters

Brief descriptions of the various observations and measurements are itemized in this section, including instruments deployed or common methods used. Table 4 shows observations made at each station and underway (continuously). Further details of instruments and deployment and processing protocols are provided in Section 8 and in individual group sub-sections within Section 11. An instrument list is consolidated in Table A- 2 of the Appendix. *Note that commercial equipment, instruments, or materials are identified in this report to foster understanding. Such identification does not imply recommendation or endorsement by NOAA, NIST or any of the participating institutions, nor does it imply that the materials or equipment identified are necessarily the best available for the purpose.*

6.2 AOPs

AOPs measured include downwelling irradiance ($E_d(\lambda)$), upwelling radiance ($L_u(\lambda)$) and incoming solar irradiance ($E_s(\lambda)$) spectrally (λ) across a range of wavelengths (e.g., 300 nm to 900 nm). These properties are used to determine in situ $nL_w(\lambda)$ and $R_{rs}(\lambda)$ (which are comparable with the satellite products).

- $nL_w(\lambda)$, $R_{rs}(\lambda)$ measured using multiple instruments representing several sampling types deployed in a variety of ways:
    - On station
        - Water column profiles: four free-falling hyperspectral AOP profiling packages;
        - Sea surface, floating: three instrument packages with hyperspectral radiometric sensors configured to float at the sea surface

- Above surface, on deck: seven handheld radiometers deployed to make concurrent observations under identical environmental conditions using common deployment protocols

o Continuous, on deck: an imaging camera system for continuous measurements from the 02-deck

- Secchi depth (Z_{sd})
- Aerosol optical thickness (AOT, a component of atmospheric correction algorithms) using handheld sun photometers
- Radiance distribution of $L_u(\lambda)$
- Daily solar $E_d(\lambda)$ integrated from 400 nm to 700 nm, the photosynthetically available radiation (PAR) spectral region (E_d (PAR)) and $E_s(\lambda)$

6.3 IOPs

Several optical in situ instrument packages measured IOPs. During stations, some packages profiled the water column, others floated at the water surface and still others were plumbed into the underway, flow-through system. Instrument packages had unique combinations of sensors and are described in more detail within the specific group's sub section in Section 11.

6.3.1 Water Column – profiling (on station)

Measurements from dedicated IOP packages:

- Hyperspectral total absorption coefficient ($a(\lambda)$)
- Hyperspectral beam attenuation coefficient ($c(\lambda)$)
- Hyperspectral Chromophoric Dissolved Organic Material (CDOM) absorption coefficient ($a_{CDOM}(\lambda)$)
- Backscatter coefficient ($b_b(\lambda)$)
- Fluorescence

IOPs included on AOP packages:

- Chlorophyll fluorescence
- CDOM fluorescence
- Phycoerythrin fluorescence
- Scattering ($b(\lambda)$) at 443 nm, 530 nm and 860 nm by NOAA/STAR and at 660 nm by USF).

IOP on the *Explorer's* CTD/Rosette package:

- Chlorophyll fluorescence

6.3.2 Continuous – near surface (underway flow-through and deck-mounted)

Flow-through:

- Hyperspectral $a(\lambda)$ and $c(\lambda)$
- $b_b(\lambda)$ at 470 nm, 572 nm and 670 nm
- Chlorophyll and UV fluorescence (ship)
- CDOM fluorescence
- Phycobilipigments fluorescence
- Phytoplankton functional types (PFTs; imaging)
- Phytoplankton photo-physiology from variable fluorescence

Deck mounted:

- E_d(PAR)

6.3.3 Discrete water sampling

These parameters were determined from analyses of discrete water samples collected from Niskin bottles on the CTD/Rosette or from the underway flow-through system:

- Extracted fluorometric Chl-*a* (fluorometry)
- Suspended Particulate Material (SPM; mass)
- Particle absorption by filter pad technique (FPT; spectrophotometry)
- CDOM (spectrophotometry)
- Phytoplankton pigments by high performance liquid chromatography (HPLC)
- Particulate organic carbon (POC) and particulate organic nitrogen (PON); (C H N combustion elemental analyzer)
- Nutrients; N (nitrate and nitrite), P and Si (colorimetry)
- Preserved samples for phytoplankton assemblage characterization (microscopy)
- Phytoplankton automated imagery
- Phytoplankton size
- Phycobilipigment types
- Photosynthetic efficiency (F_v/F_m; variable fluorometry)

6.3.4 Other ship measurements

These additional parameters were observed by onboard instrumentation maintained by the ship.

- Profiling CTD-rosette package
    - Salinity
    - Sea surface temperature
    - Dissolved O_2
- Air temperature Currents (Acoustic Doppler Current Profiler; ADCP)
- Meteorology
    - Wind speed
    - Wind direction
    - Sea state
    - Air temperature

Table 4. Parameters observed by station number and underway.

EX-18-04 Station ID#	**1**	**2**	**3**	**4**	**5**	**6**	**7**	**8**	**9**	**10**	**11**	**12**	**13**	**14**	**15**	**16**	**17**	**18**	**19**	**20**	**21**	**22**	**23**	**24**	**Underway**
Date in May 2018	**9**	**11**	**11**	**11**	**11**	**12**	**12**	**12**	**12**	**13**	**13**	**13**	**13**	**14**	**14**	**14**	**15**	**15**	**16**	**16**	**16**	**16**	**17**	**17**	**9 to 17**
Day of Year	**129**	**131**	**131**	**131**	**131**	**132**	**132**	**132**	**132**	**133**	**133**	**133**	**133**	**134**	**134**	**134**	**135**	**135**	**136**	**136**	**136**	**136**	**137**	**137**	**129 to 137**
***$L_u(\lambda)$, $R_{rs}(\lambda)$, $nL_w(\lambda)$, $E_s(\lambda)$* profiles**																									
NOAA/STAR-1	x	x	x	x	x	x	x	x	x	x	x	x	x	x	x	x	x	x	x	x	x	x	x		
NOAA/STAR-2		x	x	x	x	x	x	x		x	x	x	x	x	x	x	x	x	x	x	x	x	x		
USF	x	x	x	x	x	x	x	x		x	x	x	x	x	x	x	x	x	x	x	x	x	x		
OSU	x	x	x	x	x	x	x	x		x	x	x	x	x	x	x	x	x	x	x	x	x	x		
***$L_u(\lambda)$, $R_{rs}(\lambda)$, $nL_w(\lambda)$, E_s* surface, imager**																									
CCNY	x	x	x	x	x	x	x	x	x	x	x	x	x	x	x	x	x	x	x	x	x	x	x	x	x
***$L_u(\lambda)$, $R_{rs}(\lambda)$, $nL_w(\lambda)$, $E_s(\lambda)$* surface, in-water floating**																									
Stennis/USM	x	x	x	x		x	x	x		x	x	x	x	x	x		x	x	x	x	x	x	x		
Stennis/NRL		x		x		x	x	x		x	x	x	x	x	x		x	x	x	x	x	x	x		
RISBA UMB	x	x	x	x		x	x	x		x	x	x	x	x	x		x	x	x	x	x	x	x		
NURADS	x	x	x	x			x	x																	
***$L_u(\lambda)$, $R_{rs}(\lambda)$, $nL_w(\lambda)$, $E_s(\lambda)$* surface, handheld**																									
SEV OSU	x	x	x	x		x	x	x		x	x	x	x	x	x	x	x	x	x	x	x	x	x	x	
SEV Stennis/NRL	x	x	x	x		x	x	x		x	x	x	x	x	x	x	x	x	x	x	x	x	x	x	
SEV UMB	x	x	x	x		x	x	x		x	x	x	x	x	x	x	x	x	x	x	x	x	x	x	
ASD Stennis/NRL	x	x	x	x		x	x	x		x	x	x	x	x	x	x	x	x	x	x	x	x	x	x	
ASD USF		x	x					x		x	x					x	x					x	x		
ASD NOAA	x	x	x	x		x	x	x		x	x	x	x	x	x	x	x	x	x	x	x	x	x	x	
SVC NOAA	x	x	x	x		x	x	x		x	x	x	x	x	x	x	x	x	x	x	x	x	x	x	
GER CCNY	x	x	x	x		x	x	x		x	x	x	x	x	x	x	x	x	x	x		x		x	
***$L_u(\lambda)$, $R_{rs}(\lambda)$, $nL_w(\lambda)$* reference plaques**																									
NOAA white	x		x	x		x	x	x		x	x	x	x	x	x	x	x	x	x	x	x	x	x	x	
NOAA gray	x		x	x		x	x	x		x	x	x													
NIST blue	x		x	x		x	x	x		x	x	x		x	x	x	x	x	x	x	x	x	x	x	
CCNY white			x	x		x	x	x		x	x	x		x	x	x	x	x	x	x	x	x	x	x	
USF gray			x	x		x	x	x		x	x	x		x	x	x	x	x	x	x	x	x	x	x	
OSU white	x		x	x		x	x	x		x	x	x		x	x	x	x	x	x	x	x	x	x	x	
AOT (Microtops)																									
NOAA/STAR	x		x		x	x	x		x	x	x	x	x	x											
CCNY	x	x	x	x		x	x	x	x	x	x	x	x	x	x	x	x		x	x	x	x			

EX-18-04 Station ID#	1	2	3	4	5	6	7	8	9	10	11	12	13	14	15	16	17	18	19	20	21	22	23	24	Underway
Date in May 2018	9	11	11	11	11	12	12	12	12	13	13	13	13	14	14	14	15	15	16	16	16	16	17	17	9 to 17
Day of Year	129	131	131	131	131	132	132	132	132	133	133	133	133	134	134	134	135	135	136	136	136	136	137	137	129 to 137
Radiance distribution of L_u	x	x	x				x																		
E_d(PAR)	x	x	x	x	x	x	x	x	x	x	x	x	x	x	x	x	x	x	x	x	x	x	x		
$a_p(\lambda)$, $a_d(\lambda)$, $a_g(\lambda)$, optical sensors	x	x	x	x	x	x	x	x	x	x	x	x	x	x	x	x	x	x	x	x	x	x	x		x
$c(\lambda)$	x	x	x	x	x	x	x	x	x	x	x	x	x	x	x	x	x	x	x	x	x	x	x		x
$a_{CDOM}(\lambda)$	x	x	x	x	x	x	x	x	x	x	x	x	x	x	x	x	x	x	x	x	x	x	x		
$b_b(\lambda)$	x	x	x	x	x	x	x	x	x	x	x	x	x	x	x	x	x	x	x	x	x	x	x		x
$b(\lambda)$	x	x	x	x	x	x	x	x	x	x	x	x	x	x	x	x	x	x	x	x	x	x	x		x
CDOM fluorescence	x	x	x	x	x	x	x	x	x	x	x	x	x	x	x	x	x	x	x	x	x	x	x		x
CDOM (spectrophotometry)	x	x	x	x	x	x	x	x	x	x	x	x	x	x	x	x	x	x	x	x	x	x	x		
$a_p(\lambda)$, $a_d(\lambda)$, $a_g(\lambda)$, filter pad technique	x	x	x	x	x	x	x	x	x	x	x	x	x	x	x	x	x	x	x	x	x	x	x		
Chl-*a* and UV fluorescence	x	x	x	x	x	x	x	x	x	x	x	x	x	x	x	x	x	x	x	x	x	x	x		x
Chl-*a* extracted	x	x	x	x	x	x	x	x	x	x	x	x	x	x	x	x	x	x	x	x	x	x	x	x	
POC	x	x	x	x		x	x	x		x	x	x		x	x	x	x								
SPM	x	x	x	x																					
HPLC pigments	x	x	x	x	x	x	x	x	x	x	x	x	x	x	x	x	x	x	x	x	x	x	x		
Nutrient concentrations (N, P, Si)	x	x	x	x	x	x	x	x	x	x	x	x	x	x	x	x	x	x	x	x	x	x	x		
Microscopy	x	x	x	x	x	x	x	x	x	x	x	x	x	x	x	x	x	x	x	x	x	x	x		
Phycoerythrin fluorescence	x	x	x	x	x	x	x	x	x	x	x	x	x	x	x	x	x	x	x	x	x	x	x		x
F_v/F_m and σ_{PSII}	x	x	x	x	x	x	x	x	x	x	x	x	x	x	x	x	x	x	x	x	x	x	x		x
Phycobiligment types (PE1, PE2, PE3)	x	x	x	x	x	x	x	x	x	x	x	x	x	x	x	x	x	x	x	x	x	x	x		x
Secchi depth	x	x	x	x		x	x	x	x	x	x	x	x	x	x	x	x	x	x	x	x	x	x		
Air temperature	ship																								
Wind speed and direction	x	x	x	x	x	x	x	x	x	x	x	x		x	x	x	x	x	x	x	x	x	x	x	x
Currents	ship																								
Salinity	x	x	x	x		x	x	x		x	x	x		x	x	x	x	x	x	x	x	x	x	x	x
SST	x	x	x	x	x	x	x	x	x	x	x	x	x	x	x	x	x	x	x	x	x	x	x	x	x
Dissolved O2	x	x	x	x	x	x	x	x	x	x	x	x	x	x	x	x	x	x	x	x	x	x	x		
Water depth	x	x	x	x		x	x	x		x	x	x	x	x	x	x	x	x	x	x	x	x	x	x	x
Cloud cover	x	x	x	x	x	x	x	x	x	x	x	x	x	x	x	x	x	x	x	x	x	x	x	x	

7 Laboratory Calibration of Radiometers

Pre- and/or post-cruise calibrations of several radiometers used in this cruise were conducted at the NOAA/STAR Optical Characterization Experiment Laboratory in College Park, Maryland using a secondary lamp with the calibration transferred from a FEL type 1000 W standard irradiance lamp (#39040C, F667) and an Optronic Laboratories OL-455-18 integrating sphere both with radiometric values traceable to NIST (Figure 3). A discussion of the theoretical basis for radiometric instrument calibration was included in the 2014 cruise Technical Report [Ondrusek et al., 2015] as based on primary research by Zibordi and Voss [2014] and by Johnson et al. [2014] and others. Before the cruise, on 28 April 2018, and then again shortly after the cruise, on 13 June 2018, a total of 14 sensors from several instrument packages as listed below were calibrated.

- 4 Satlantic HyperPro Profiler IIs (i.e., HyperPro; two from NOAA/STAR, and one each from USF and OSU)
- 2 floating HyperPro radiometers (USM and NRL)
- The UMB HyperPro modified Radiometer Incorporated Sky Blocked Apparatus (RISBA; [Lee et al., 2013])

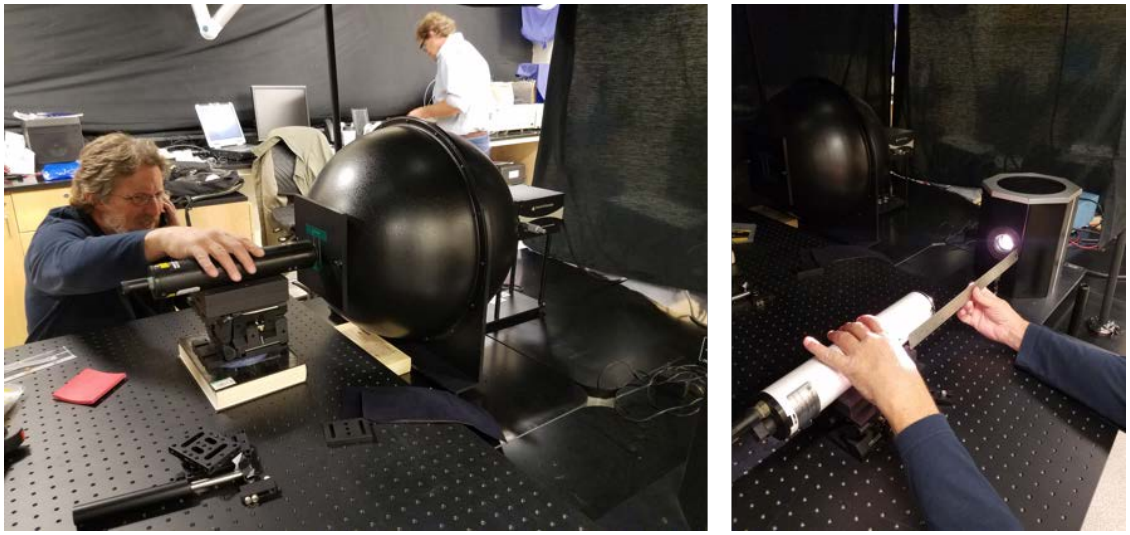

Figure 3. Calibration activities at the NOAA/STAR optical laboratory.

Figure 4 shows an example of calibration source measurement results demonstrating the importance of utilizing cruise specific response functions. In this example the NOAA/STAR *Es* 234 irradiance sensor is used. The NIST determined calibration values are overlaid with the spectral radiance of the lamp source measured with the *Es* 234 sensor using the calibration coefficients from the old and current calibrations. Figure 5 shows the percent difference between the lamp spectral output and that measured by the radiometer using the old calibration. This indicates the errors mitigated by updating the calibration for the cruise.

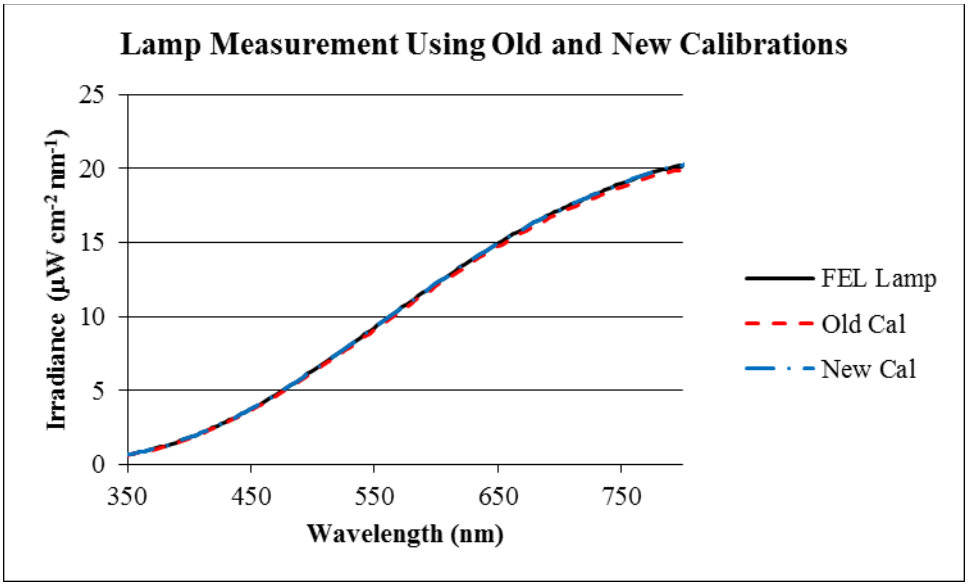

Figure 4. The NIST FEL calibration source output overlaid with the measurements of that same source with the NOAA OCR234 irradiance sensor using the old (2017) and new (6/13/2018) calibrations.

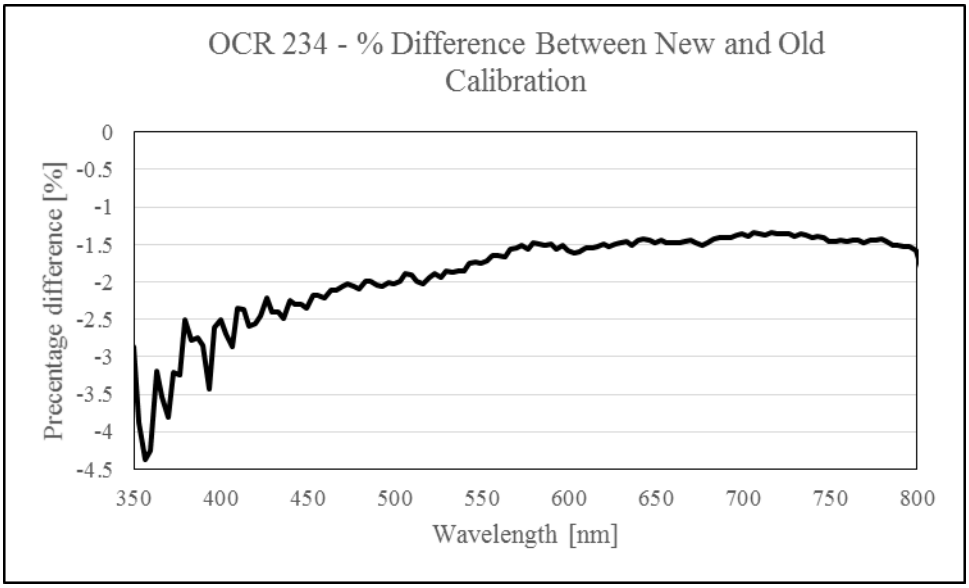

Figure 5. The percent difference between the calibration source output and that measured by the NOAA OCR234 irradiance sensor using the 2017 calibration.

8 Common Radiometric Measurements: Methods and Protocols

8.1 Overview of in situ radiometry methods

As light from the sun passes through seawater, its spectral shape and intensity are changed. Some of the light that enters the ocean is eventually re-emitted. This re-emitted light is part of the light that the ocean color satellite sensor "sees". An in-water profiling radiometer is essentially a pair of spectrometers, one, upward looking, which measures $E_d(\lambda)$, and another, downward looking, which measures $L_u(\lambda)$, both mounted on an instrument that is dropped through the water column. An above-water reference sensor simultaneously measures $E_s(\lambda)$. These measurements are used to calculate $nL_w(\lambda)$, which is the parameter retrieved from ocean color satellites. Above-water radiometers measure water leaving radiances which are used in the calculation of $nL_w(\lambda)$. These $nL_w(\lambda)$ are used to validate satellite ocean color radiances and

to derive other ocean color products such as Chl-*a* or SPM concentrations used in ecological studies [Ondrusek et al., 2012].

During this 2018 Cal/Val cruise, in situ observations were made using multiple spectroradiometric instruments that can be grouped by three distinct operational approaches: 1) in-water profiling, 2) surface floating, and 3) above-water, handheld. Each approach has fundamental strengths and weaknesses. In-water profiling radiometers provide depth-resolved optical information about the water column below the surface. To calculate $nL_w(\lambda)$, values must be extrapolated, or modeled, from below the water's surface to above the water's surface. Sensors can be (and have been for this cruise) calibrated with NIST traceable reference sources. Deployment is not difficult but requires dedicated ship activity to put the cable-tethered instrument over the side. A complete series of measurements acquired (integrated) might take 10's of minutes to an hour, for example, during which time varying sky conditions are to be avoided. Additional sensors (to simultaneously measure IOPs, for example) are often included with the instrument package. The floating radiometers are the same basic instrument as the profiling radiometers but are mounted with a buoyant collar so they remain in place near the sea surface. This arrangement allows for simultaneous above-water $E_d(\lambda)$ and below water $L_u(\lambda)$ measurements very close to the actual sea surface, or, in the case of the RISBA, both the $E_d(\lambda)$ and the $L_u(\lambda)$ sensors are just above the sea surface with the $L_u(\lambda)$ sensor shielded to block sky light. The above-water, handheld devices are relatively inexpensive and deployment logistics are not as labor or resource intensive as the in-water instruments. Sampling time integration is generally shorter (e.g., seconds to minutes), reducing risk of changes in sky conditions. The above-water observations are more directly related to the satellite observation but are subject to multiple sources of light contamination (such as sun glint, sea foam, reflections from ship structure, etc.) and sampling variation. In theory, no instrument calibration is required for the handheld instrument because a reference plaque of known reflectance is measured. See reports on this topic [IOCCG, 2018; Ruddick, 2018] for additional discussions.

Multiple profiling radiometers, floating radiometers and handheld spectrometers were deployed by groups using an agreed-upon set of protocols and common processing methods. These multi-instrument common deployments are described in the next three sections (8.2, 8.3 and 8.4). Sometimes, individual researchers made additional observations using different protocols to test the effects of protocol on measurements, which are discussed within the respective group's section.

8.2 In-water profiling radiometry

Four HyperPro profiling radiometers (USF, OSU and two by NOAA/STAR) were deployed simultaneously during this 2018 Cal/Val cruise in a similar fashion to the deployments of the previous Cal/Val cruises [Ondrusek et al., 2017; Ondrusek et al., 2016; Ondrusek et al., 2015] following recommended protocols [Satlantic, 2012, 2004], keeping them away from the ship and each other, and avoiding ship shadowing. At each station, the ship was positioned so that the sun was directly off the stern. The four profiling instruments, which were weighted to produce a descent rate of approximately 0.1 m s^{-1} to 0.3 m s^{-1}, were positioned evenly spaced at the stern (Figure 6) and lowered together to the sea surface. The ship steamed at approximately 1 knot as the cables were let out until the profilers were at least 20 m off the stern. After that, the ship maintained just enough headway to maintain the heading, to prevent the profilers from closing in on the ship and to prevent them from crossing cables while profiling. For each station, three to five multicast measurement sets were conducted. For each set, all four profilers were lowered to approximately 10 m to 15 m depth through the euphotic zone and raised together three to five times. If sky conditions changed significantly during the cast, the set was stopped and restarted when the conditions were favorable again.

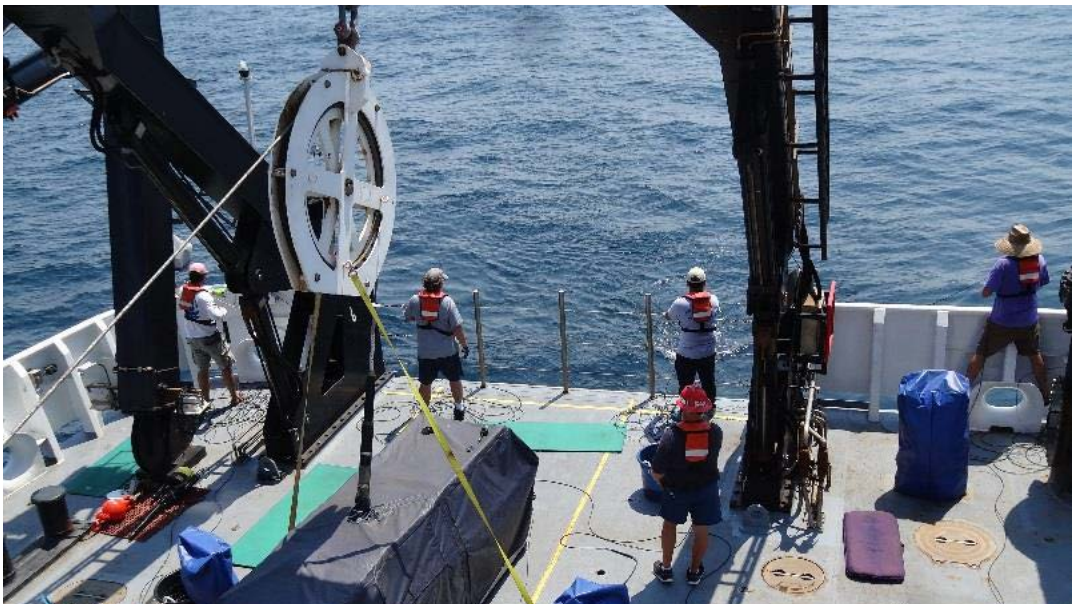

Figure 6. Four HyperPro profiling radiometers were deployed simultaneously from the stern.

Profilers were deployed during 23 of the 24 stations. On the first station, only three of the four profilers were deployed. At Station 9, only a single profiler was deployed due to time constraints and sea conditions. No profilers were deployed on the last station. The profiling radiometers were calibrated before and after the cruise from 350 nm to 900 nm as described in Section 7.

The HyperPro system has a downward looking HyperOCR radiometer that measures $L_u(\lambda)$ and an upward looking HyperOCI irradiance sensor to measure $E_d(\lambda)$ in the water column. Each HyperOCR or HyperOCI has a 256-channel silicon photodiode array detector with 10 nm spectral resolution and spectral sampling of 3.3 nm pixel^{-1}. The HyperOCRs have dark signal corrections performed using shutter dark measurements collected every fifth scan. The above-water reference sensor was an upward looking HyperOCI irradiance sensor to measure $E_s(\lambda)$ used during data reduction. All of the E_s sensors (one for each instrument package) were mounted on a telescoping tower mounted on the 02-deck as pictured in Figure 7A. Additional sensors incorporated into these profiling radiometer packages measure pressure, temperature, conductivity, and tilt. WETLabs ECO-Puck Triplet sensors for IOPs are also included in the profiling radiometer packages. Each group's ECO-Puck arrangements were unique and are described in the respective sub-sections of Section 11.

For consistency, the data processing for all of the profiling HyperPro systems followed multi-cast protocols established by Michael Ondrusek of NOAA/STAR using Satlantic ProSoft processing software version 8.1.6. The $nL_w(\lambda)$ spectra are calculated using the equation:

$$nL_w(\lambda) = L_w(\lambda, 0^+) * F_0(\lambda)/E_s(\lambda) \qquad (1)$$

where F_0 is the extraterrestrial solar irradiance at mean Earth-Sun distance and $E_s(\lambda)$ is the downwelling spectral irradiance just above the surface and is measured with the above-water HyperOCR irradiance reference sensor. $L_w(\lambda)$ is the water-leaving radiance calculated just above the surface by:

$$L_w(0^+, \lambda) = L_u(0^-, \lambda) * [(1-\rho(\lambda, \theta))/n_w(\lambda)^2] \qquad (2)$$

Here, $\rho(\lambda, \theta)$ is the sea surface Fresnel reflectance and is set as 0.021, and $n_w(\lambda)$ is the Fresnel refractive index of seawater and is set here as 1.345. $L_u(0^-, \lambda)$ is the calculated upwelling radiance just below the surface and is determined by using the diffuse attenuation coefficient ($K(L_u)$) calculated using a least squares regression fit from log transformed measured $L_u(\lambda)$ values and the intercept just below the surface.

8.3 In-water floating (surface) radiometry

The three floating radiometer systems utilized during this cruise are HyperPros outfitted with floating collars that position the sensors at the ocean surface. Two systems (Stennis/USM and Stennis/NRL) had the radiometers configured to measure $L_u(\lambda)$ just below the surface and $E_s(\lambda)$ just above the surface (Figure 7B). The third system (UMB) was configured as a RISBA ([Lee et al., 2013]) where both the L_u and the E_s sensors are positioned just above the water and the $L_u(\lambda)$ is covered with a cone extending to the water surface allowing the direct measurement of $L_w(\lambda)$ while blocking skylight reflection. The three systems were deployed simultaneously off the stern, acquiring about 5 min to 15 min of data (Figure 7C).

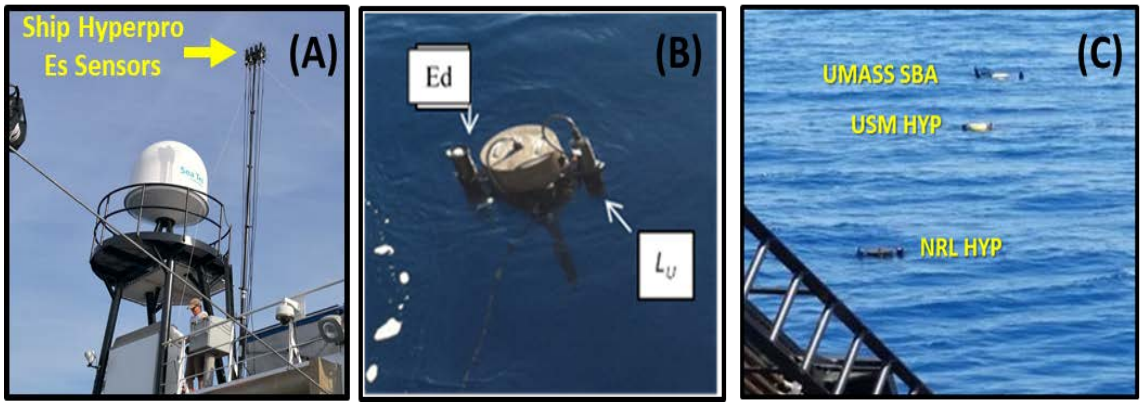

Figure 7. A) Telescoping pole on which $E_s(\lambda)$ sensors are mounted. B) Stennis/USM floating HyperPro in the water. C) The three floating HyperPros deployed.

8.4 Above water radiometry with handheld instruments

Above-water handheld radiometry measurements were conducted by the "Above Water Group" (AWG; Figure 8) using eight handheld instruments from three commercial vendors (Table 5) at 22 out of 24 stations, skipping Station 5 and Station 9 because they were late in the day and the total time for these stations was limited. In addition, OSU operated a prototype instrument as part of its development process. Also, on the bow, sun photometer data to measure AOT were collected by NOAA and CCNY.

Figure 8. AWG participants from left to right: Ahmed El-Habishi (CUNY), Carlos Carrizo (NOAA), Ivan Lalovic (GYBE/OSU), Carol Johnson (NIST), Eder Herrera (USF), Nick Tufillaro (OSU), Sherwin Ladner (NRL), Charles Kovach (NOAA), Zhehai Shang (UMB) and Xiaolong Yu (UMB).

Table 5. Participant institutions in the AWG and spectroradiometers used in the marine $R_{rs}(\lambda)$ determinations and reference plaque experiment.

Institution	Instrument	Serial Number	Spectral Range* and Resolution [nm]	FOV [°]	Fiber Coupled	Vendor**
NOAA	FieldSpecHandHeld 2	1847	350 to >1000; 3	10	No	ASD
NOAA	HR-512i	916214	350 to 1050; 3	8	No	Spectra Vista
CCNY	GER 1500	2053	350 to 1050; 3	4	No	Spectra Vista
OSU	PSR-1100F	1494439	320 to 1100; 3.2	8	Yes	Spectral Evolution
NRL	FieldSpecHandHeld 2	1897	325 to 1075; 1	10	No	ASD
NRL	PSR-1100F	178-4475	320 to 1100; 1	8	Yes	Spectral Evolution
USF	FieldSpecHandHeld 2	1886	350 to >1000; 3	7.5	No	ASD
UMB	SR-1901	14B82A3	350 to 1000; 4 and 1000 to 1900; 10	5	Yes	Spectral Evolution

*The practical range for use with seawater is approximately 350 nm to 850 nm
**For full vendor identification see Table A- 2 in the Appendix.

At each station, the AWG met on the bow with their instruments and made near-coincident (within ≈40 min) measurements of the water reflectance. Seven of the eight instruments were deployed together using an agreed-upon standardized deployment protocol and the NOAA, 99% white reference plaque (Reference #99AA08-0615, 8/h NIST traceable, calibrated by Labsphere on Jul. 8, 2015). In addition, other 10% grey and 99% white reflectance plaques, along with the NIST blue tile, were measured by individual groups for comparison. This common deployment is described further, below. Most of the measurements made with the USF ASD instrument used their own deployment protocol (see Section 11.5).

The common AWG instrument configurations, reference plaque and measurement angles are as follows.

- Integration time was optimized for each target prior to collection (i.e., integration time of sensor was changed based on relative brightness of the target and new dark counts were taken to correct for instrument noise). Integration times ranged from 68 ms to 4352 ms. USF protocol (for the ASD-HH2) uses a measurement series optimization, rather than optimization for each component of the $R_{rs}(\lambda)$ estimate.

- The reflectance plaque, referred to here as the "NOAA white plaque," is a 99% white Spectralon® card with a known directional/hemispherical reflectance and assumed to be a near-Lambertian surface. Its radiance is measured to provide a quantity proportional to E_s.
- Instruments were positioned to make the reference measurement at between ≈30 cm and ≈60 cm above the NOAA white plaque.
- Fore-optic attachments with FOV angles unique to each instrument were used.
- Five to ten consecutive radiometric spectral measurements were taken of each of the following targets: NOAA white plaque (S_{white}), water (S_{sfc}), and sky (S_{sky}).
- All measurements were made on the bow of the ship. The exact location of sampling was dependent on the orientation of the ship relative to the sun to eliminate shadowing from the vessel and surface contamination.
- The desired optical sensor zenith angles (θ) for the NOAA white plaque (θ_{white}), water (θ_{sfc}) and sky (θ_{sky}) measurements were 135°, 135° and 45°, respectively. The desired relative azimuth angle of the sensor to the sun ($\Delta\varphi$) was 90° up to 135° depending on sea conditions and ship orientation.

Processing of AWG data to retrieve $R_{rs}(\lambda)$ is being conducted using group specific processing software that follows the guidelines of Mueller et al. [2003a] and utilizes different processing models for comparison including: R_{rs} _sfc (no NIR reflectance correction), R_{rs}_fresnel (Fresnel correction omitted), R_{rs} [Carder and Steward, 1985], R_{rs}_Lee [Lee et al., 1997], and R_{rs}_Gould [Gould et al., 2001]. More discussion of the methods can be found in earlier dedicated VIIRS Cal/Val cruise reports [Ondrusek et al., 2017; Ondrusek et al., 2016; Ondrusek et al., 2015].

In addition to this common group activity, some AWG group members made additional measurements using their own established protocols with variations involving, for example, reference plaques, scan angles, number of scans, integration times and post-processing methods. These variations are described within each of the collaborating groups' sections.

8.5 AWG measurements of the reference standards

To test the performance of the above-water radiometers with a colored reflectance standard and evaluate the reproducibility of in situ transfers of reflectance scales between reflectance targets, the AWG measured additional targets during the normal sky, water, and reference plaque sequence for deriving the marine $R_{rs}(\lambda)$. These additional targets function as Device Under Test (DUT) in this experiment. As in the *Nancy Foster* cruises [Ondrusek et al., 2017; Ondrusek et al., 2016; Ondrusek et al., 2015] the NIST blue reference tile (described in Section 11.6) was the primary DUT and it was measured at all AWG stations by all participants, as was the NOAA white plaque (see Table 6). The NOAA white plaque will serve as the reference standard for these AWG intercomparison measurements. CCNY, OSU, and USF measured their reference plaques in addition to the NOAA plaques and the NIST blue tile, so these plaques serve as DUTs for the respective teams when referenced to the NOAA white plaque. Note for the retrieval of R_{rs}, NOAA and NRL will use the NOAA white plaque while CCNY, OSU, and USF will use their reference plaques, (see Section 11 and relevant sub-sections).

Table 6. Diffuse reflectance plaques used by the AWG, where R_X is the 8/h reflectance factor (dimensionless) and the dimensions are width by length by thickness of the scattering material.

Institution	Nominal R_X	Dimensions, cm	Material	Vendor*	Model Number	Serial Number
NOAA	0.99	30.5x30.5x1.0	Spectralon	Labsphere, Inc.	SRT-99-120	99AA08-0615
NOAA	0.10	30.5x30.5x1.0	Spectralon	Labsphere, Inc.	SRT-10-120	DF83F-7522
CCNY	0.95	20x20x0.2	Zenith Lite	Sphere Optics	SG 3151	#17022310 S/N 1
OSU	0.99	12.7x12.7x1.0	Spectralon	Labsphere, Inc.	SRT-99-050	99AA03-0818-8375
USF	0.10	25.4x25.4x?	n/a	n/a	n/a	USF #5, 13879-A
NIST	0.12 at 409nm	16.5x16.5x0.4	F65 plate glass	NIST	NaN	NaN

*For full vendor identification see Table A- 2 in the Appendix.

With the NOAA white plaque as the reference standard for the intercomparisons, the apparent reflectance, (R_{DUT}) of the DUT plaque is determined from

$$R_{\mathrm{DUT}}(\lambda) = R_{\mathrm{NW}}(\lambda)\frac{S_{\mathrm{DUT}}(\lambda)}{S_{\mathrm{NW}}(\lambda)} \qquad (3)$$

In Equation 3, the symbol $S(\lambda)$ is used for the output of the radiance radiometer, and the subscripts refer to the NOAA white plaque (NW) or one of the five DUT plaques, see Table 6. If all the plaques are perfect Lambertian diffusers, the reflected radiance is independent of the solar zenith angle (SZA) and sky radiance distribution, and the spectral directional/hemispherical reflectance factors that are supplied as calibration values equate to $R_{DUT}(\lambda)$ and $R_{NW}(\lambda)$ in Equation 7, see [Nicodemus et al., 1977]. If the plaques are not perfect Lambertian diffusers, e.g. the bi-directional reflectance distribution function (BRDF, reported in units of inverse steradian) depends on incident and view geometries, then the reflectance factors are AOPs and we can expect to see departures consistent with the target BRDF, SZA, sky conditions, and observing geometry [Castagna et al., 2019].

Departures from Lambertian behavior for gray and white sintered polytetrafluoroethylene (PTFE, the material in the AWG plaques) are documented [Georgiev and Butler, 2008; Germer, 2017; Patrick et al., 2013], and measurements on the blue tile at NIST and the National Aeronautics and Space Administration Goddard Space Flight Center (NASA/GSFC) show the blue tile is not Lambertian. However, for nearly simultaneous measurements under similar illumination conditions, all researchers should derive the same reflectance values for the DUTs target when using NOAA white reflectance standard as the reference. This will provide an estimate of the reproducibility of the derived DUT reflectance values. The blue tile increases the parameter space to include the instrument sensitivity to stray light, which is exacerbated by differences between the spectral distribution of the calibration source (sunlight) and the unknown source (sky and water).

The large intercomparison plaques were placed on the *Okeanos Explorer* bow bollard posts and made level using a small spirit level (Figure 9) since holding them at shoulder level for the length of time necessary for all participants to measure them was not practical. Labels were placed on the sides of the NOAA white, NOAA gray, and NIST blue tile to indicate which side to point to the Sun and from which

direction to observe the target at relative azimuths of 90° or 135°. If the ship repositioned during a station, the plaques were realigned to the sun as rapidly as possible. Figure 9 illustrates that the bridge, the participants, and the bow rail prevented the plaques from seeing the full hemisphere. The magnitude of this bias will depend on how much of the diffuse component is blocked by these bodies [Castagna et al., 2019].

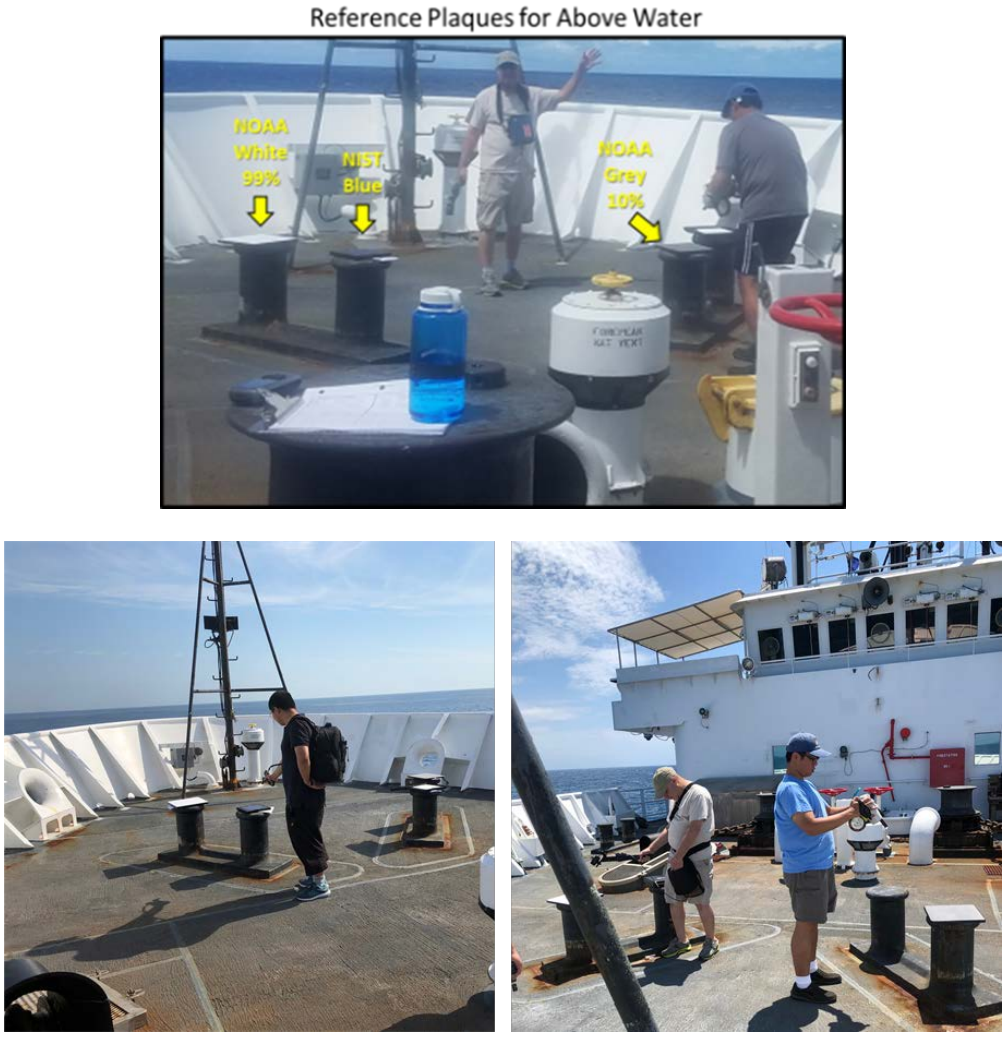

Figure 9. AWG activities on the bow of the Okeanos Explorer: (Top) Bow of *Okeanos Explorer* used for collecting above-water handheld radiometry. Different reference plaques were measured at each station including NOAA's 10% grey Spectralon, NOAA's 99% reflective white Spectralon and NIST's 12% reflective at 409 nm (blue) Spectralon. (Bottom left) UMB measuring the NIST blue tile; (Bottom right) OSU measuring the USF 10% gray plaque and USF measuring the NOAA 10% gray plaque.

At the start of each station, the targets were placed on the bollard posts, oriented with the identified side into the Sun (to eliminate effects of BRDF asymmetry), and leveled using shims. NIST operated a Garmin GPSMAP 78sc global positioning mapping instrument, saving waypoints at selected locations as well as recording the entire track during the station. NIST recorded observations on hand written log sheets during each station and took photographs of the sky conditions and the participants in action. NOAA and NRL attempted to make concurrent measurements, starting with the ASDs; the operators were Kovach and Ladner. CCNY and USF usually acquired data over the entire station; the operators were El-Habashi and Huang. OSU's SEI was operated by Tufillaro and the OSU prototype by Lalovic, who also took images of the sky using a fisheye lens attached to a smartphone. If feasible, they operated as a team,

with one person holding their small reference plaque while the other measured. UMB performed as a team, with operators Shang and Yu. Because OSU and UMB deployed profilers, which often were simultaneous with the AWG measurements, Lalovic, Shang, and Yu typically joined the AWG after the measurements were underway. At the end of each station, the plaques were returned to their containers and the radiometers were secured. At the end of the day, all equipment was stored in a ship compartment on the bow.

All the spectroradiometer raw data will be delivered to NIST, and the $R_{DUT}(\lambda)$ values for the different targets will be computed using the NOAA white plaque as the reference. Because three (the OSU SEI, the CCNY GER, and the NOAA HR-512i) out of the 8 spectroradiometers were calibrated for spectral radiance responsivity, it is possible to derive $E_s(\lambda)$ from those solar-illuminated plaque data. These values can be compared to the $E_s(\lambda)$ values from the sensors mounted on the telescoping mast as part of the in-water profiling protocol.

9 Intercomparison of in-situ measured nL_w

Up to 13 instruments are shown (Figure 10 through Figure 12) in the comparisons of $nL_w(\lambda)$ including four profiling HyperPros, three floating HyperPros including the RISBA, and six out of eight handheld above-water instruments described more fully in Section 8.4. Not all instruments were deployed at each station depending on conditions or time constraints. Intercomparisons of the in situ $nL_w(\lambda)$ measurements from multiple methods at each station are shown to provide an estimate of in situ measurement variability. For each station, $nL_w(\lambda)$ are displayed for each instrument along with the average $nL_w(\lambda)$ of all instruments. The number of instruments varies for each station. Since spectral resolutions differ between instruments, all data were spectrally weighted to VIIRS spectral band responses. For each station, instruments that gave measurements beyond one standard deviation (σ) from the average of all instrument measurements at that station were omitted from the results.

Table 7 gives the percent difference for each instrument at each band for all stations as well as the percent difference of individual instrument $nL_w(\lambda)$ relative to the average $nL_w(\lambda)$ of all instruments at each station.

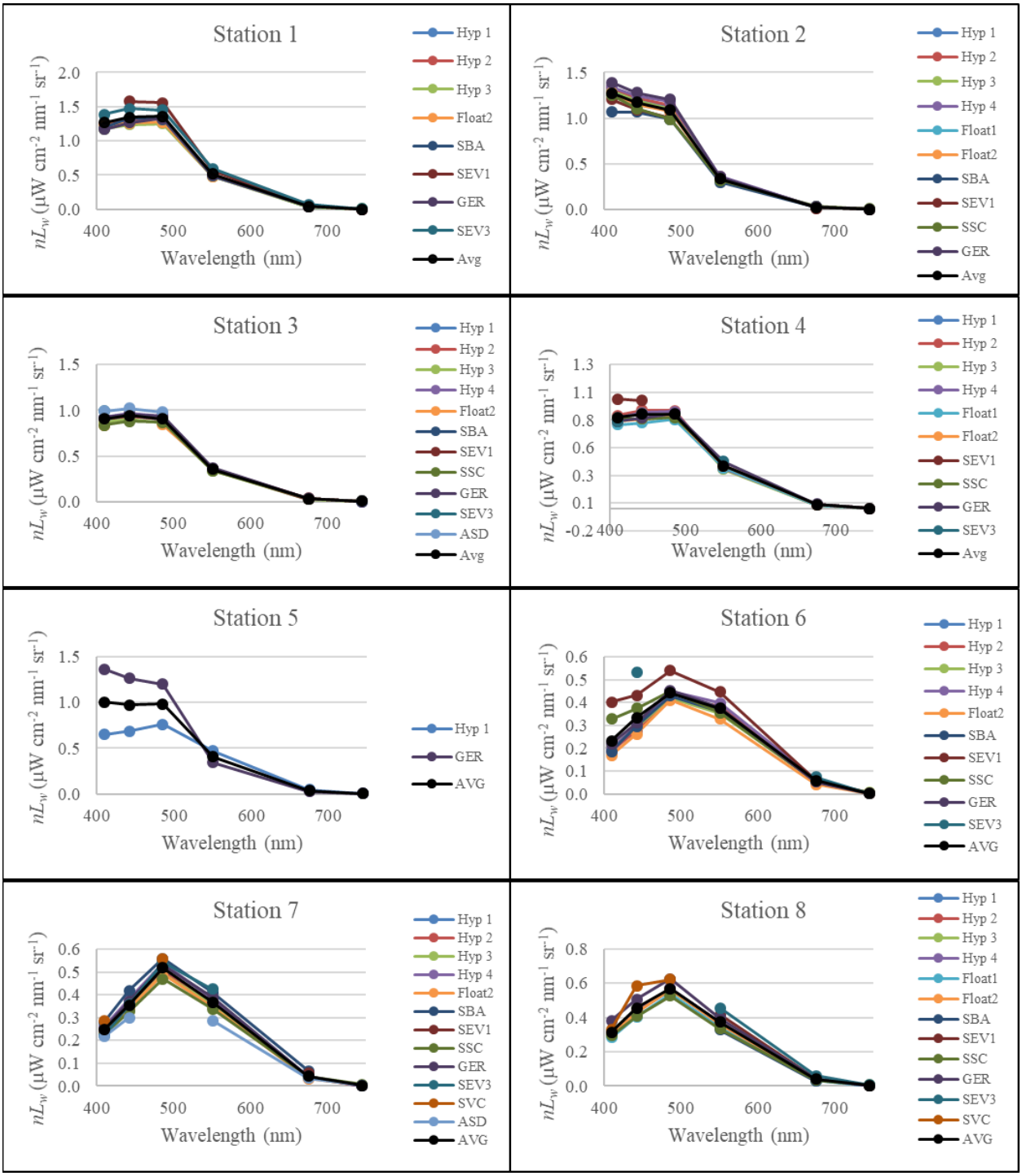

Figure 10. VIIRS band weighted $nL_w(\lambda)$ plots of each instrument (by color) and the average $nL_w(\lambda)$ of all instruments ("AVG" in black) measured at each station for Station 1 through Station 8 as labeled. Hyp 1 through Hyp 4 are the profiling HyperPros; Float1 and Float2 are the floating HyperPros; SBA is the RISBA floating HyperPro; SEV, SSC, GER, SVC and ASD are the handheld above-water instruments described in Section 8.4.

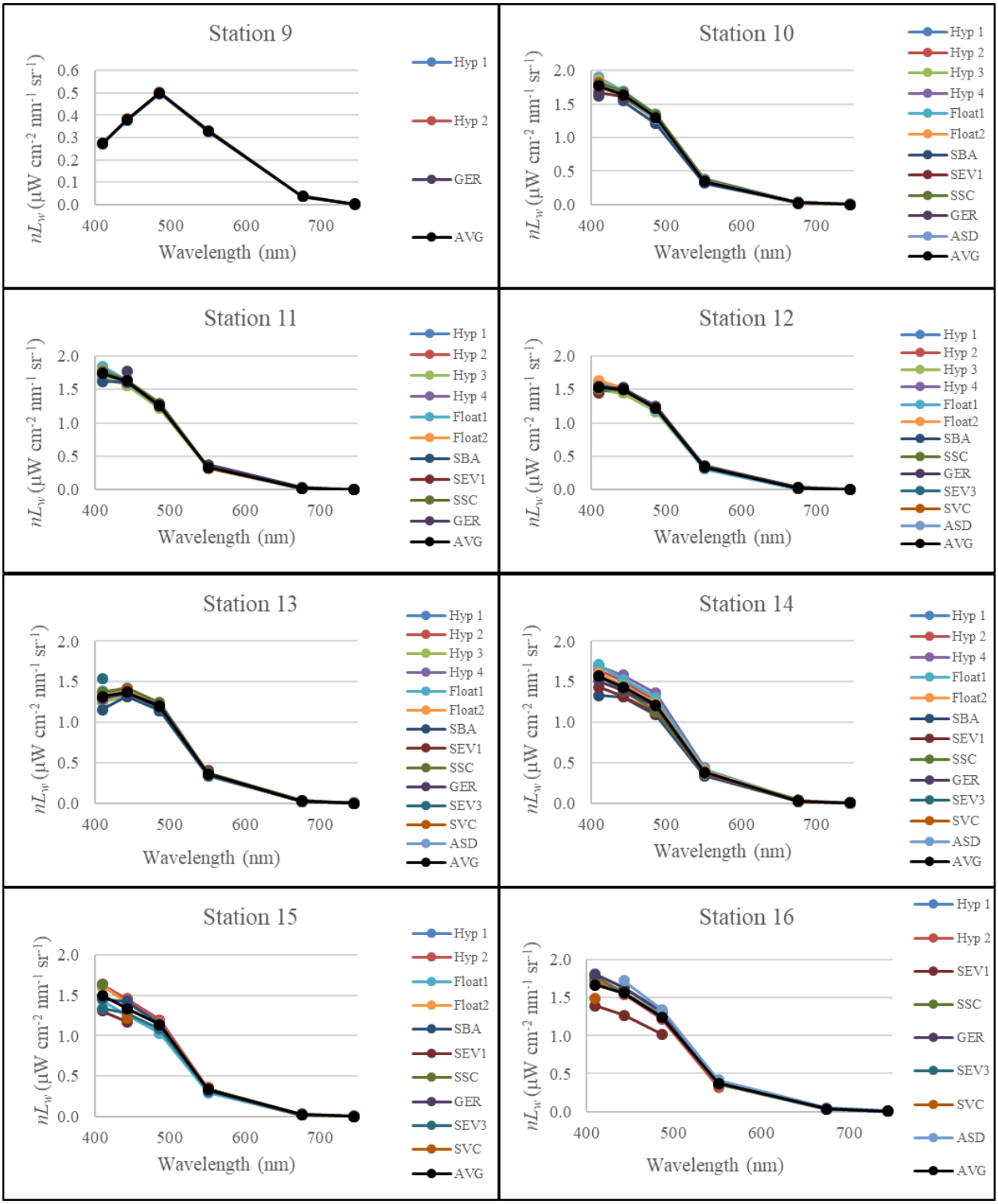

Figure 11. As for Figure 9 for Station 9 through Station 16.

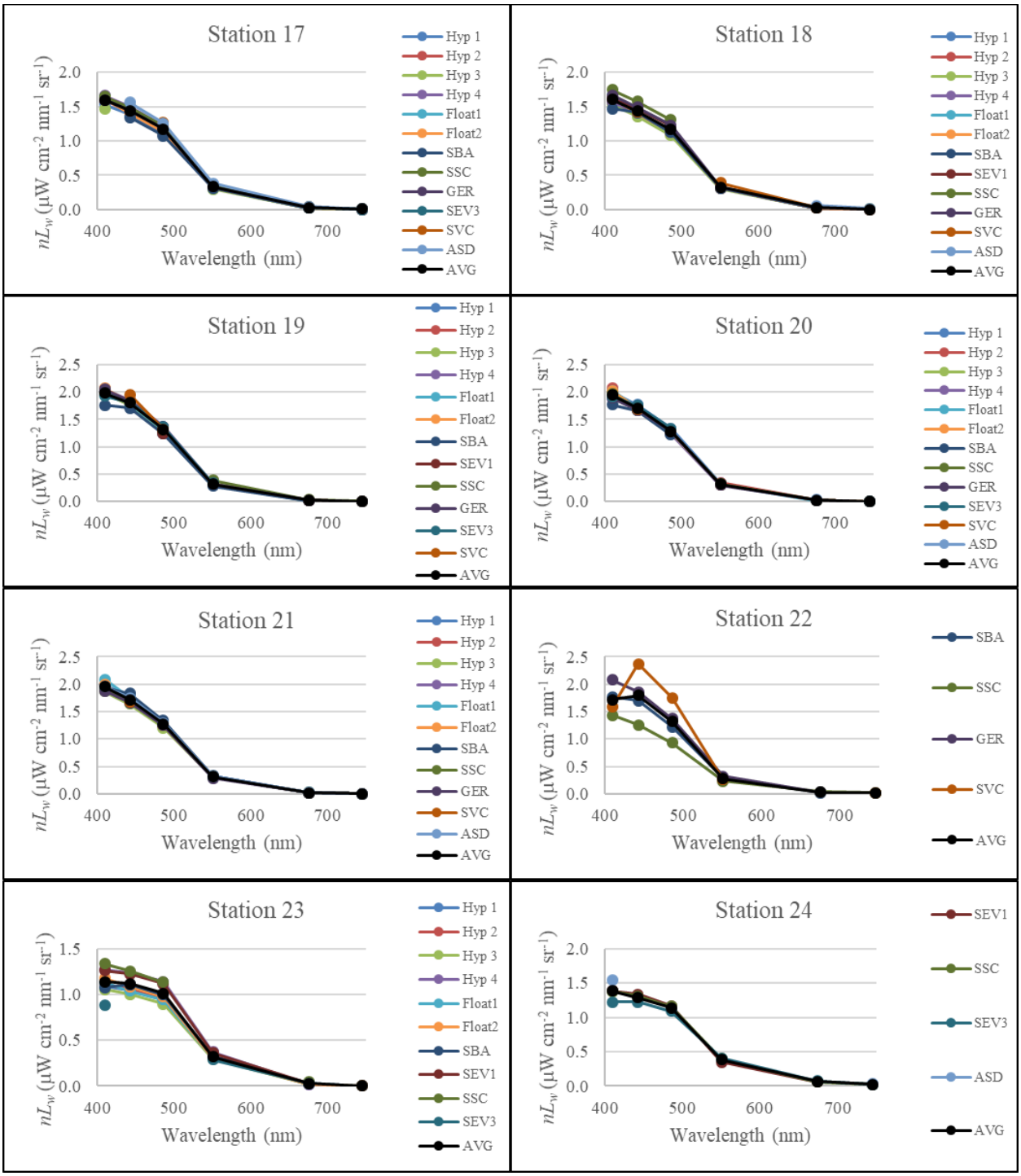

Figure 12. As for Figure 9 for Station 17 through Station 24.

Table 7. The average across all stations of the percent difference of individual instrument $nL_w(\lambda)$ relative to the average $nL_w(\lambda)$ of all instruments. Instrument abbreviations are as for Figure 10.

Band [nm]	Hyp 1	Hyp 2	Hyp 3	Hyp4	Float 1	Float 2	SBA	SEV1	SEV2	GER	SEV3	SVC	ASD
410	-2.71	0.20	-3.14	0.87	2.06	-0.49	-6.78	-4.14	2.55	3.65	-2.91	-19.28	1.85
443	-2.24	-0.67	-4.01	1.83	-1.50	-2.43	-1.78	2.57	-1.19	2.87	8.91	7.31	2.21
486	-1.14	-0.28	-4.24	3.04	-0.98	-1.81	-3.20	1.31	-1.35	3.95	1.81	9.64	4.65
551	-0.53	-0.17	-4.31	2.22	-2.06	-2.82	-3.96	7.81	0.66	2.02	7.80	5.30	2.73
675	-6.52	-6.99	-5.66	-8.77	-7.33	-3.94	-8.18	1.22	18.99	0.90	25.52	2.01	38.97
Average without 675 nm	-1.66	-0.23	-3.93	1.99	-0.62	-1.89	-3.93	1.89	0.17	3.12	3.90	0.74	2.86
Average all	-2.63	-1.59	-4.27	-0.16	-1.96	-2.30	-4.78	1.76	3.93	2.68	8.22	1.00	10.09

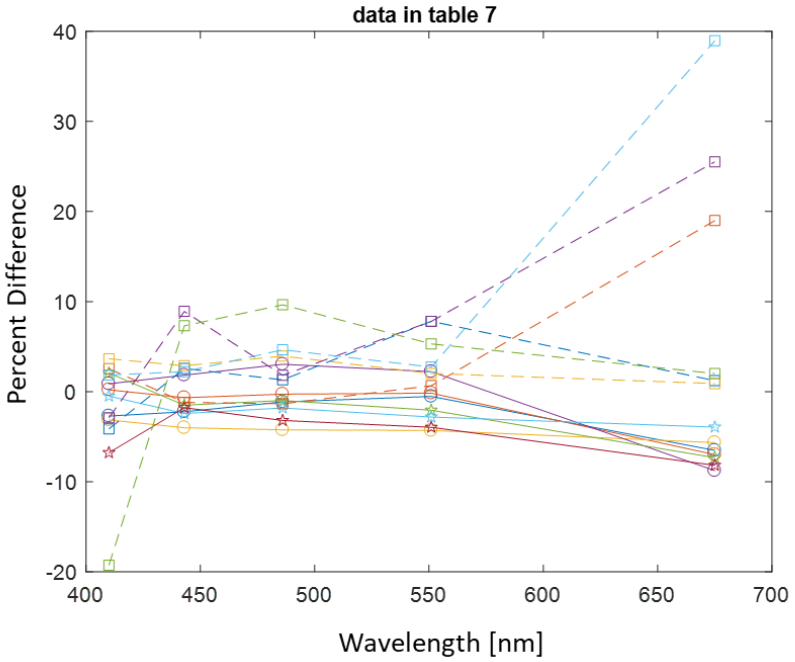

Figure 13. Data from Table 7. Circles are the profilers, stars are the floaters and SBA, and dashed lines are the AWG. The spread in AWG is about the same, but is biased a bit higher than the profilers.

10 Validation of VIIRS with in situ observations

To assess the performance of the VIIRS ocean color satellite sensors during the time of our cruise, the VIIRS SNPP and NOAA-20 $nL_w(\lambda)$ are compared to in situ data for each station. The VIIRS SNPP and NOAA-20 data are processed by the STAR Ocean Color Science Team using MSL12. Processing version for SNPP was NPPSCINIR_L2; SCI_OC04.0_v1.21 and processing for NOAA-20 was J01_SCINIR_L2; SCI_OC4.0_v1.21_v1.30. The method for determining valid satellite data to use for matchups with in situ data follows Wang et al, [2009] and is briefly described as follows: For each in situ observation, $nL_w(\lambda)$ satellite data from a 5 pixel by 5 pixel box centered on the in situ sampling location are obtained. The average and σ of the $nL_w(\lambda)$ values of the 25 pixels in the box are calculated. Next, values with 1.5 or

greater σ from the average are omitted. If the count of the remaining "good" values is greater than 50% of the original count (i.e., 13 or more out of 25), the average and σ are recalculated for the remaining "good" pixels. These results are then matched with the in situ observation. For the in situ measurements, up to 13 instruments were used to measure water-leaving radiances as described in Section 9. To remove outliers in the in situ data, the average and σ were calculated for all the instruments utilized at each station. Then, for each wavelength band, any data that were greater one σ were removed and then the final average and σ were calculated. Spectral results for each station for the two VIIRS sensors and the quality average representation of all the in situ are shown in Figure 14 and Figure 15. The spectral percent differences between satellite and each in situ instrument (i.e., (satellite – in situ)/in situ * 100) are shown in Table 8 for SNPP and Table 9 for NOAA-20. Explanations for the differences shown here will be investigated.

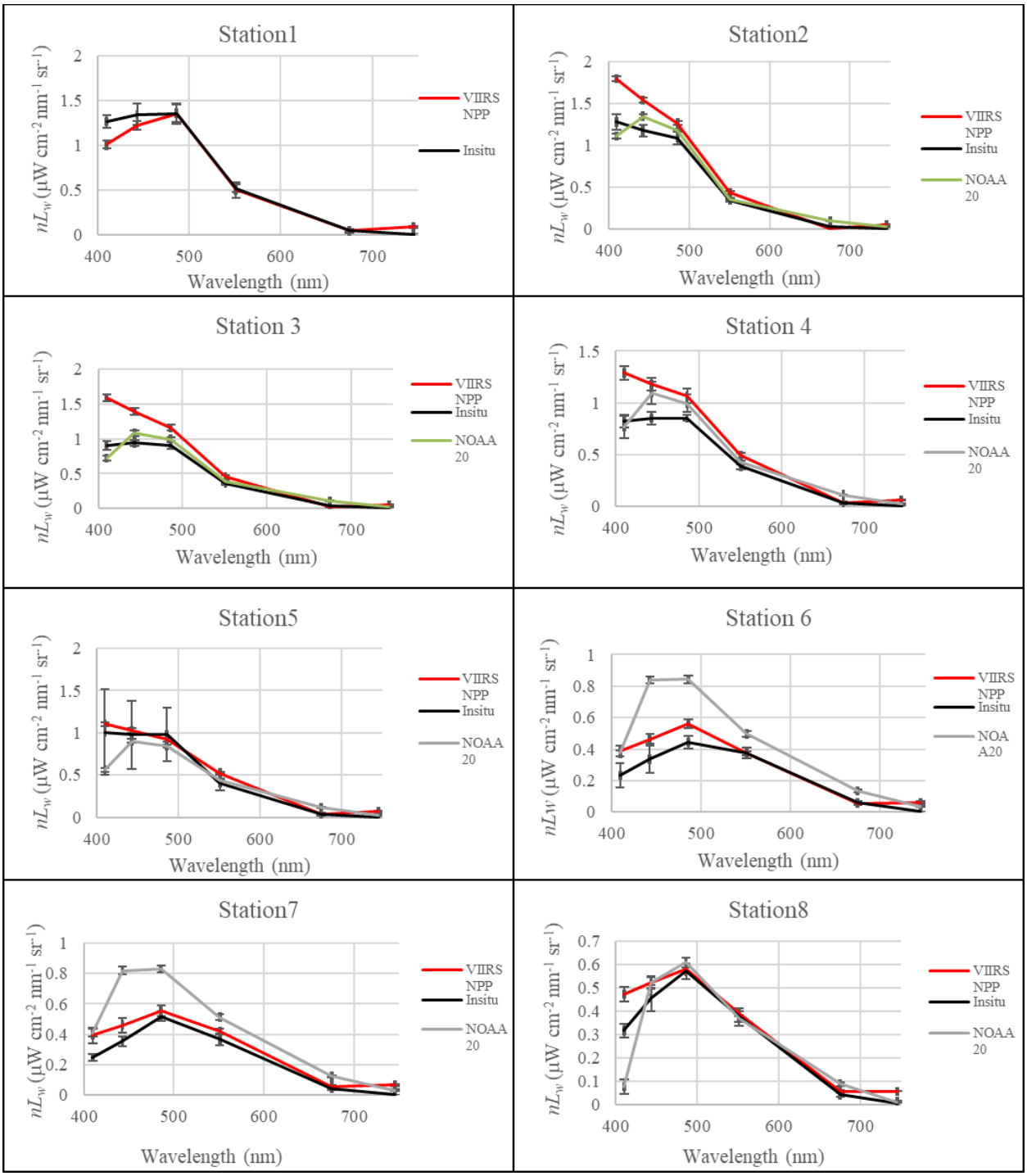

Figure 14. Preliminary MSL12 VIIRS 5 by 5 average (NPP – red, NOAA20 – grey) versus the average for all in situ measurements (Black) at each station for Station 1 through Station 8

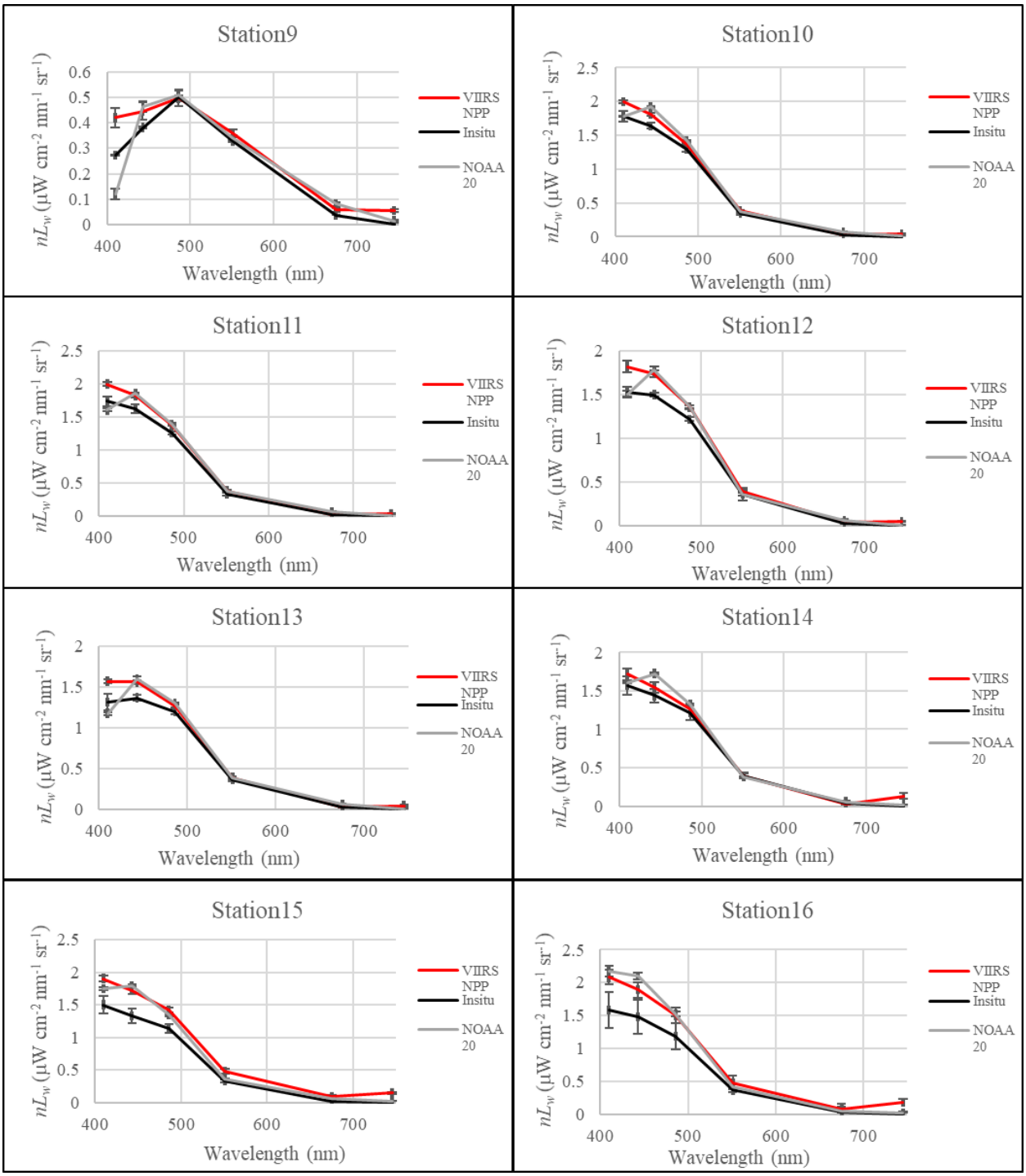

Figure 15. Same as Figure 14 but for Station 9 through Station 16.

Table 8. VIIRS SNPP percent difference relative to average of all instruments averaged for all stations.

Band	Hyp 1	Hyp 2	Hyp 3	Hyp4	Float 1	Float 2	SBA	SEV1	SEV2	GER	SEV3	SVC	ASD	NPP
410	33.49	30.10	33.29	32.90	21.01	32.80	31.68	29.28	29.13	25.28	31.80	39.59	36.77	31.32
443	21.33	20.45	23.23	20.58	17.71	20.66	16.60	21.49	22.32	15.18	6.65	8.98	21.21	18.18
486	10.73	11.12	14.43	7.90	10.21	13.11	11.98	14.48	13.82	6.03	5.55	1.37	7.98	9.90
551	13.54	12.84	14.05	8.92	15.38	14.76	15.75	-2.45	14.56	10.93	5.17	18.85	13.58	11.99
675	154.41	134.69	79.59	91.86	158.29	121.57	138.91	131.78	116.91	114.39	89.91	323.46	110.10	135.84
avg all	46.70	41.84	32.92	32.43	44.52	40.58	42.99	38.92	39.35	34.36	27.82	78.45	37.93	41.45
Avg 410-55	19.77	18.63	21.25	17.58	16.08	20.33	19.00	15.70	19.95	14.36	12.29	17.20	19.89	17.85

Table 9. NOAA-20 VIIRS percent difference relative to average of all instruments averaged for all stations.

Band	Hyp 1	Hyp 2	Hyp 3	Hyp4	Float 1	Float 2	SBA	SEV1	SEV2	GER	SEV3	SVC	ASD	NOAA20
410	-0.95	-0.37	2.14	0.34	-18.07	6.93		6.16	1.17	-2.96	8.32	6.12	20.45	2.44
443	43.27	43.72	51.17	41.98	20.03	55.74	51.90	40.94	44.86	33.26	93.99	-4.13	54.35	43.93
486	20.62	21.67	28.57	18.87	9.29	26.12	30.50	30.61	28.62	15.17	53.36	9.24	8.22	23.14
551	11.47	11.87	17.60	8.99	5.03	15.20	16.58	0.53	15.10	8.13	0.19	5.73	26.76	11.01
675	-39.05	-40.37	-38.54	-40.33	-50.06	-38.36	-43.12	-39.93	-49.76	-40.53	-57.62	-41.08	-44.00	-43.29
avg all	7.07	7.30	12.19	5.97	-6.76	13.13	13.96	7.66	8.00	2.61	19.65	-4.82	13.16	7.45
Avg 410-551	18.60	19.22	24.87	17.54	4.07	26.00	32.99	19.56	22.44	13.40	38.96	4.24	27.45	20.13

11 Participating Science Groups' Unique Activities, Methods and Protocols

11.1 NOAA/STAR – Michael Ondrusek, Eric Stengel, and Charles Kovach

In-water and above-water radiometry

In addition to organizing and planning daily operations for the cruise, NOAA/STAR led the simultaneous deployment of the in-water profiling radiometry instruments as described in Section 8.2 and participated in the AWG as described in section 8.4. NOAA/STAR operated two HyperPro Profiler II packages each equipped with depth, temperature, tilt and WET Labs ECO-Puck Triplet sensors. The first profile system (serial number #86) was equipped with one ECO-Puck sensor that measured fluorescence to estimate concentrations of chlorophyll *a*, CDOM and phycoerythrin, and one ECO-Puck sensor that measured b_b at 443 nm, 530 nm, and 860 nm. The second profiler (serial number #179) was equipped with a built-in CTD and had one Wetlab ECO-Puck equipped with chlorophyll fluorescence and two backscatter channels at 443 nm and 530 nm.

NOAA/STAR used two instruments in the AWG participation. One system was the ASD HandHeld2 and the other was the Spectra Vista 512i. The ASD has a spectral range of 325 nm to 1075 nm and a spectral resolution of less than 3 nm. This unit was equipped with a built in GPS and was equipped with fore-optics with a 10° FOV. The other NOAA system used was a Spectra Vista HR-512i. The NOAA HR-512i covers a spectral range of 350 nm to 1050 nm, a 3 nm spectral resolution, and an 8° FOV. Validation measurements were conducted at most stations on the bow with the rest of the AWG using a NOAA Spectralon white plaque with a nominal reflectance of 0.99. Auxiliary experiments were also conducted with the AWG using blue and grey reflective plaques (see Section 8.4).

Preliminary results of the two NOAA in-water profiling Hyperpros and the NOAA above-water ASD results are compared with VIIRS SNPP MSL12 science quality spectra are shown in Figure 15. Station 7 was collected in the Mississippi River plume on 12 May 2018 with the chlorophyll concentration of 0.29 mg m^{-3} and water leaving radiance signals characteristic of coastal waters. Station 10 was collected on 13 May 2018 farther to the south, where chlorophyll concentrations were lower, at 0.085 mg m^{-3}. This more oligotrophic water type is also evident in the spectral shape of the $nL_w(\lambda)$ signal with maximum spectral peaks in the 410 nm band.

.

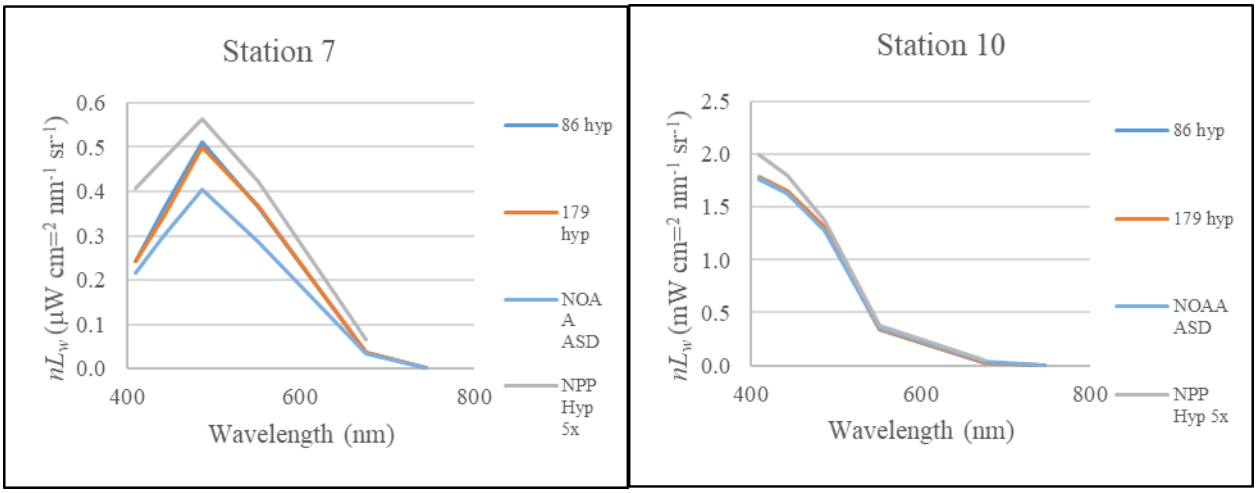

Figure 16. Preliminary results from Station 7, 12 May 2018 (left) and Station 10, 13 May 2018 (right) in situ comparisons with MSL12 VIIRS SNPP science quality spectra.

Extracted fluorometric Chl-*a*

Chl-*a* concentrations were measured using a Turner 10 AU Fluorometer [Welschmeyer, 1994]. Surface samples were collected in duplicate at each station from the Rosette Sampler and several times a day while underway from the flow-through system to calibrate the underway chlorophyll fluorometers. 100 mL to 400 mL of seawater was filtered on a 25 mm diameter, 0.7 µm glass microfiber filter (GF/F; Whatman). The filters were frozen in liquid nitrogen, then extracted in 90% acetone in a freezer for at least 48 h. The samples were vortexed and then centrifuged for 5 min before being measured on the Turner 10 AU.

Suspended Particulate Matter (SPM)

SPM samples were collected in duplicate from the surface waters for each station. Up to 2 L of water were collected for each sample and processed according to techniques outlined by Hunter et al. [2006]. Water samples were filtered on pre-weighed 47 mm diameter GF/F filters. The volume of filtrate was then measured with a graduated cylinder and recorded. Filters were rinsed three times with distilled water, placed in 47 mm diameter Petri dishes and oven dried at 60 °C for 12 h then stored in a desiccator until analysis. Filters were weighed on a Sartorius CPA 2250 balance and weighed at least three times until consecutive readings were less than 0.055% variable [EPA, 1971].

HPLC and POC/PON

Water from two hydrographic depths, one in the near-surface and the second near the chlorophyll maximum, were collected from each CTD rosette cast. Near-surface samples were also collected from the underway flow-through system and sometimes from a bucket cast. Water collected from the CTD Niskin bottles was transferred to 10 L carboys which were covered with black plastic bags to prevent high light exposure while awaiting filtration. Single or duplicate samples for each parameter were filtered. For each sample, a known volume of water was filtered under gentle vacuum (≈16.9 kPa) onto a 25 mm diameter Whatman GF/F filter (nominal pore size ≈0.7 µm). For HPLC, filter samples were wrapped in aluminum foil and stored in liquid nitrogen onboard. For POC/PON, samples were filtered onto pre-combusted Whatman GF/F 25 mm filters. POC/PON filters were placed in pre-combusted foil pouches and flash frozen in liquid nitrogen. In the laboratory, both HPLC and POC/PON samples are stored at -80°C until analysis and were analyzed at the NASA Goddard Space Flight Center, Ocean Ecology Laboratory. The HPLC method is modified from Van Heukelem and Thomas [2001]. POC/PON samples are acidified by fuming with HCl, dried and then measured using an elemental analyzer.

AOT

AOT was measured at 11 stations using a Microtops sun photometer. The data are delivered for processing to NASA as part of the AERONET Marine Aerosol Network program.

11.2 Stennis - Robert Arnone (USM), Sherwin Ladner (NRL) and Wesley Goode (NRL)

Stennis Participation Cruise

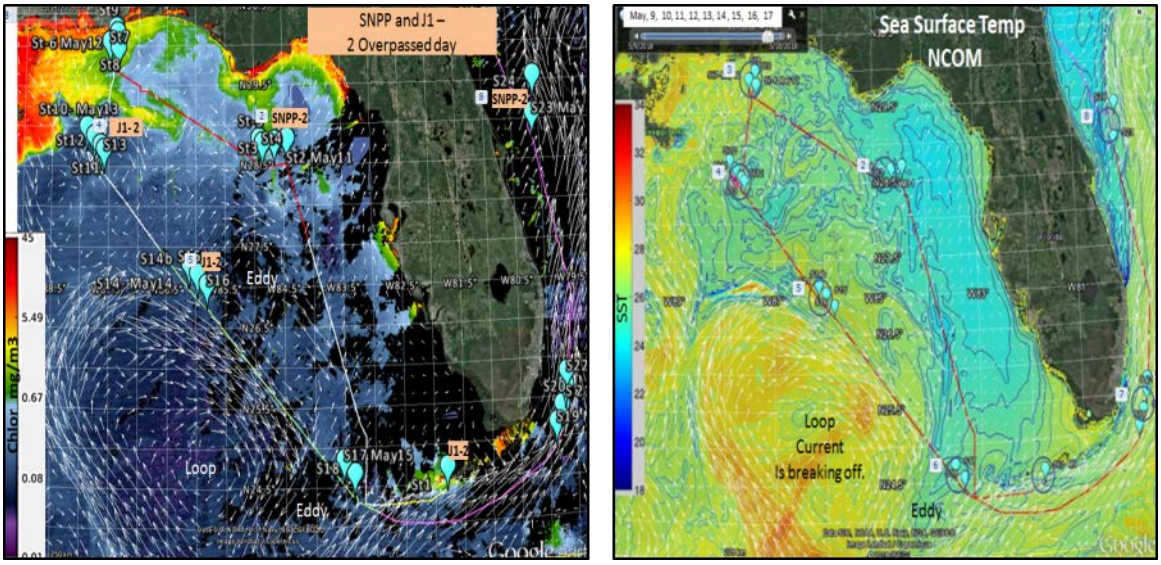

Figure 17. (Left) Chl-*a* image illustrating the *Okeanos Explorer* cruise track (solid line) and 24 stations (cyan symbols) for the time period 9 to 17 May 2018. Days when two VIIRS overlaps occurred are labeled SNPP-2 for SNPP and J1-2 for NOAA-20 at station locations collected for that day. Stations for a particular day are labeled with month (May) and day (9 to 17). (Right) Sea Surface Temperature (color map in units of °C) and currents (white vectors) from the Navy Coastal Ocean Model (NCOM) with stations (cyan symbols) and cruise track (solid line).

The *Okeanos Explorer* cruise track on 9 May 2018 to 17 May 2018 (Figure 17) consisted of a total of 24 stations over the 9 day period with station collection omitted on 10 May 2018 due to cloud cover in the southeastern Gulf of Mexico near Key West, FL forcing operations to be relocated to the Northern Gulf of Mexico where clear sky conditions were forecasted. Future stations were adaptively planned and selected based on weather forecasts and clear sky conditions so that satellite matchups could be obtained.

The goals for the cruise sampling included testing methods for collection and processing protocols for in situ ocean color measurements from different instruments to determine uncertainty in measurements and improve in situ and satellite matchups for consistent and accurate satellite Cal/Val. Stennis group participation and measurements during the cruise included coordination with NOAA and other Cal/Val teams for adaptive daily planning of the cruise track and sampling locations using real time satellite and ocean model data, winds and cloud cover forecasts from the US NOAA Global Forecast System and the European Centre for Medium-Range Weather Forecasts models using the Windy (European) website (https://www.windy.com) for the Gulf of Mexico and Western Atlantic along the U.S. East Coast.

The Stennis Group Cal/Val sensor measurements included: 1) $R_{rs}(\lambda)$ using two floating Hyperpros, one from NRL and the other from USM; 2) Z_{sd} using a 30.5 cm white Secchi disk from USM; 3) continuous underway IOPs from the flow-through using two ac-s instruments from NRL and USF, BB3 sensor from

NOAA and ship's CTD and fluorometer; and 4) L_w using two handheld hyperspectral radiometers (ASD and Spectral Evolution Inc.).

The collection protocols for the instruments were planned and modified based on results from previous Cal/Val cruises and agreed upon by participants to be used to test for variability between multiple in-water and above-water in situ optical ocean measurements from different instruments. By using similar data collection protocols, the observed variability between instruments due to instrument differences and characteristics, changing environment, collection geometry (sensor, solar and satellite), contamination from the ocean surface and ship, etc. can be determined.

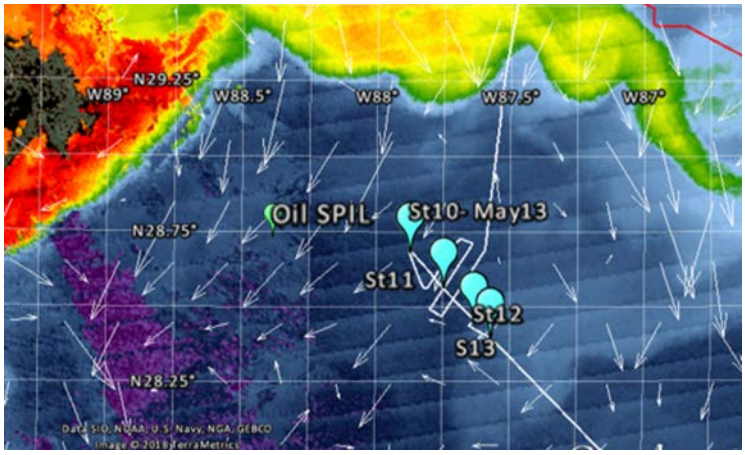

Figure 18. Possible satellite overlaps on 13 May covering Stations 10, 11, 12 and 13 near the Deep Water Horizon oil spill site had 3 VIIRS overpasses (one from SNPP and two from NOAA-20).

Stennis Measurements

Floating Hyperpro (In-Water) Measurements

The Stennis team utilized two floating Hyperpros (USM and NRL) on the cruise. The USM instrument was deployed at 20 stations including Stations 1, 2, 3, 4, 5, 7, 8, 10, 11, 12, 13, 14, 15, 17, 18, 19, 20, 21, 22 and 23 and the NRL instrument was deployed at 18 stations including Stations 2, 4, 6, 7, 8, 10, 11, 12, 13, 14, 15, 17, 18, 19, 20, 21, 22 and 23. The spectral range of both E_d and L_u sensors is from 350 nm to 805 nm at 3.3 nm ±0.1 nm increments. These instruments were used with a molded floatation collar (Figure 7B), allowing the observation of temporal variability of in-water surface measurements, at a fixed depth, just beneath the sea surface. The downwelling E_d sensor uses a cosine collector and is approximately 30 cm above the water surface, but it was not used for final $R_{rs}(\lambda)$ calculations. The L_u sensor is mounted approximately 30 cm below the water surface. The ship's E_s sensor also uses a cosine collector and was mounted along with all the participating groups' E_s sensors on the deck on a pole which was elevated above the ship's superstructure while on station for consistency (Figure 7A). E_s from the ship mounted sensors was combined with L_u from floating Hyperpro for computation of R_{rs}.. Both the USM and NRL Hyperpro L_u, E_s and E_d sensors were calibrated by NOAA/STAR (Mike Ondrusek) based on NIST calibration protocols (see Section 7). The sensors were calibrated within a month of the cruise and those values calibration was used for processing.

The floating Hyperpros were deployed from the stern of the ship on the starboard side. The instruments were allowed to float out a sufficient distance from the boat (20 m to 30 m) to prevent contamination from vessel-generated bubbles, ship shadowing and other potential disturbances. Once the instrument was at a sufficient distance from the vessel, data were recorded for each floating Hyperpro for approximately 10 min. Post processing of this dataset from level 1 to level 4 was done using Satlantic's Prosoft v8.1.5 with pre-established protocols limiting the sensor tilt to 2° from nadir.

The pre-established processing protocols for deriving $R_{rs}(\lambda)$ from in-water radiometry follow Chapter 2 of Mueller, et al. [2003a]. $R_{rs}(\lambda)$ is computed as for Equation 8 below, where $\rho = 0.021$ is the Fresnel reflectance of the air sea interface, and $n = 1.34$ is the refractive index of seawater.

$$R_{rs} = L_u * factor / E_s, \text{ where } factor = (1 - \rho) / (n^2) \quad (4)$$

The floating Hyperpro data for stations where both instruments were deployed show strong similarity in the spectral $R_{rs}(\lambda)$ for the USM and NRL sensors (Table 10 and Figure 19). $R_{rs}(\lambda)$ was computed based on the protocols used for processing and calibration by the pre-established procedure by Michael Ondrusek (NOAA/STAR). The E_s sensor for Station 22 had poor E_s values resulting in bad $R_{rs}(\lambda)$ estimates. The low variability in $R_{rs}(\lambda)$ between the floating sensors indicates confidence in data representing the stations. The $R_{rs}(\lambda)$ spectra from the two floating Hyperpros also agree with the profiling Hyperpro $R_{rs}(\lambda)$ (also discussed in Section 9).

Table 10. Ratios of mean $R_{rs}(\lambda)$ for the NRL/USM floating Hyperpro to show comparative performance.

Station ID	s02	s04	s08	s10	s11	s12	s13	s14	s15	s17	s18	s19	s20	s21	s23	Overall Mean
Ratio of mean $R_{rs}(\lambda)$ for NRL/USM Floating Hyperpros	1.029	0.953	0.945	1.026	1.034	0.957	1.026	1.055	0.898	1.028	1.021	0.967	1.015	1.020	0.995	0.998

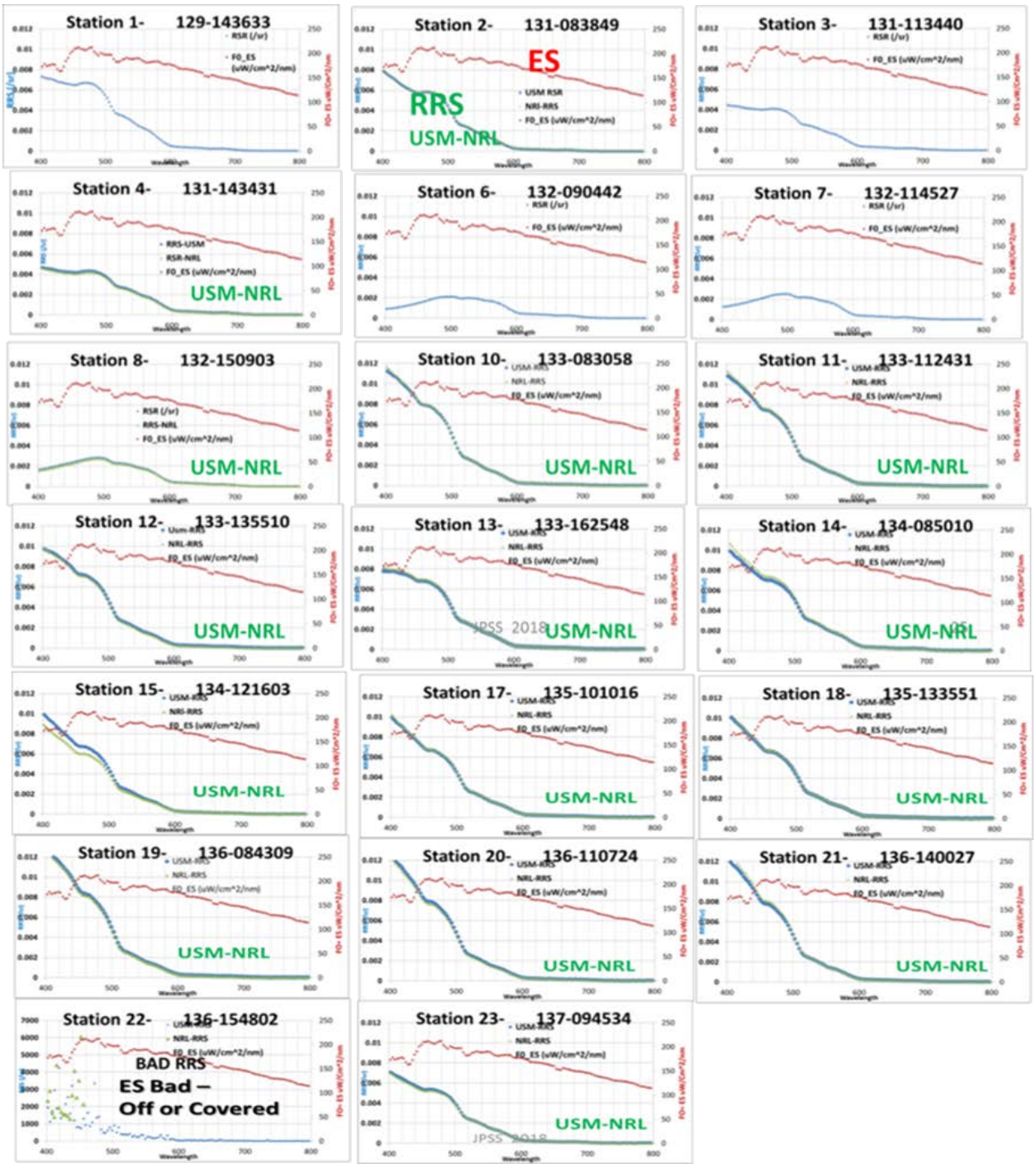

Figure 19. Floating Hyperpro spectral plots (horizontal axis is wavelength from 400 nm to 800 nm) of a ship mounted E_s sensor (red line, vertical axis on right, E_s from 0 μW cm^{-2} nm^{-1} to 250 μW cm^{-2} nm^{-1}) and the resulting $R_{rs}(\lambda)$ for both the USM and NRL instruments (blue is USM line and green is NRL line, vertical axis on left from 0 sr^{-1} to 0.012 sr^{-1}) at the 20 coincident stations as labeled on each plot. The year day and the nominal file timestamp are also shown for each plot. The $R_{rs}(\lambda)$ and E_s spectral response for all the stations are very similar and agree very well (blue and green lines overlap; means for most stations are within a few percent; see Table 10) except for Station 22 which is a result of a bad E_s measurement.

Z_d Measurements

Above water vertical visibility was characterized by Z_d. Z_d measurements were collected at Stations 1, 2, 3, 4, 6, 7, 8, 10, 11, 12, 13, 14, 15, 16, 17, 18, 19, 20, 21, 22 and 23 at different times of the day similar to the floating Hyperpros. This measurement was made by lowering a 30.5 cm diameter white Secchi disk using a calibrated rope with tape at 1 m increments into the water until the disk was no longer visible (Figure 20).

Figure 20. USM white Secchi Disk being lowered into the water.

Continuous Underway Flow-through Measurements of IOPs

IOP flow-through measurements were collected to address specific objectives as follows but will be used for other analyses as well:

a. Characterize the spatial variability of IOPs (a, b converted to b_b, c) along the cruise track and how the variability impacts the uncertainty of in situ measurements at each station along with sub-pixel variability and matchup uncertainty used for VIIRS calibration and validation.

b. Evaluate the vertical optical changes in coastal and offshore waters. The flow-through data at a source depth of 3 m can be different from the surface IOP which is what is sensed by the satellite ocean color products. Vertical profiles with CTD and IOPs can be used to evaluate the vertical changes and the effect on surface IOP validation.

c. Determine the a_t and attenuation properties at specific wavelengths to validate the IOPs derived from the VIIRS ocean color satellite.

d. Determine the optical water mass characteristics using spectral b and a to identify response of ocean color.

e. Define coastal/shelf frontal boundaries, ocean processes and water mass types using thermal, biological and optical properties.

f. Validate VIIRS Chl-a and IOP products.

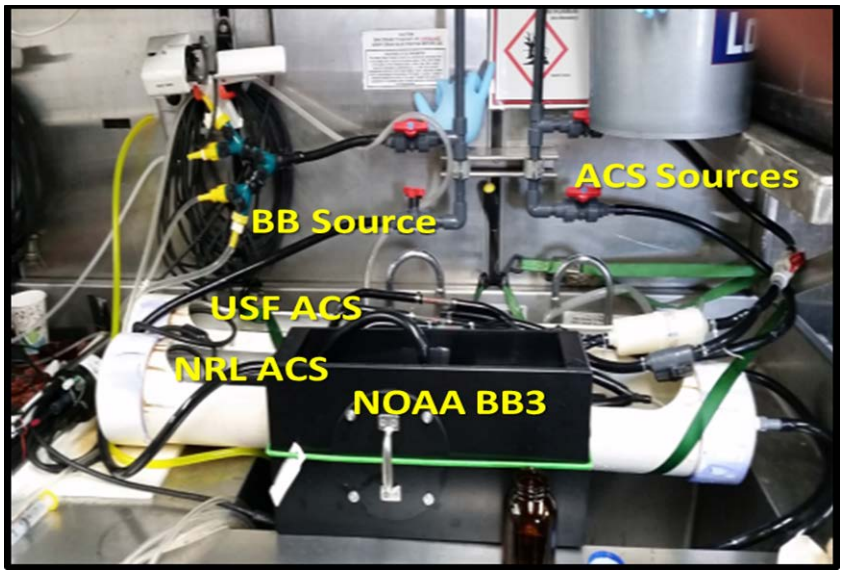

Figure 21. The Stennis group IOP continuous flow-through wet lab setup on the NOAA Ship *Okeanos Explorer*, which included two hyperspectral ac-s instruments (NRL and USF) and a BB3 sensor (NOAA). The two ac-s instruments were placed inside PVC tubes to maintain a constant temperature bath during operation. The BB3 instrument was placed inside a flow cell. Both the PVC tubes and the BB3 flow cells were designed specifically for those instruments.

IOPs were collected extensively using an underway flow-through system on the *Okeanos Explorer* designed and set up by the Stennis group including two WetLabs hyperspectral AC-S instruments (NRL SN 024 and USF SN 029) and a WetLabs BB3 backscattering instrument (NOAA) designed with three channels (440 nm, 532 nm and 650 nm) connected to the ship's seawater flow-through system where the water intake was located at 3 m below ocean surface. To ensure stability and reliability, both AC-S instruments were placed in a controlled temperature water bath to dissipate the instruments' heat and stabilize instrument temperature (Figure 21). The instruments were allowed a warm up time at the set temperature to allow them to stabilize and measure consistently. Data were collected continuously (day and night) every 10 seconds along the cruise track starting at Station 1 and ending at Station 24. Approximately 1.1 GB of data per 24 h period and 8 GB over the 9 d period were amassed for a large variety of water masses enabling the study of a variety of ocean processes.

The two ac-s instruments (NRL and USF) were interfaced with the *Okeanos Explorer* WetLabs DH4 data logger with additional inputs from the ship's flow-through system and the BB3 sensor from NOAA. The ship's flow-through system data stream included position, time, date, heading, water temperature, salinity, and fluorescence (voltage). These inputs are required for the standard processing protocol corrections during the post processing of the ac-s data. The WetLabs DH4 host software was used to combine and store all these data inputs and allowed a display capability in real-time to evaluate the ac-s and BB3 data to ensure the systems were operating correctly and producing reliable and consistent data. The data sample rate of the ac-s meters was 4 Hz. Output data files from the DH4 were saved hourly for the entire cruise.

The two ac-s sensors were calibrated daily with new device files during the cruise to correct for sensor drift. Calibration of the ac-s sensors included running Nanopure water through the instruments using a gravity feed and after the instruments were allowed to stabilize for 5 min to 10 min, recording data. This clean water calibration was done before and after cleaning the absorption and scattering tubes. An update to instrument device files was applied in real-time if it was deemed that new corrections were necessary

to assure good quality measurements using a visual display. The BB3 was maintained using the WetLabs pre-calibration which did not change during the cruise.

The hyperspectral ac-s instruments (Figure 21) measure $c(\lambda)$ and $a(\lambda)$ from 399 nm to 755 nm at 4.0 nm spacing and the BB3 instrument returns total volume scattering (β), volume scattering of particles (β_p), backscattering of particles (b_{bp}) and b_b at 3 channels (440 nm, 532 nm and 650nm). Concurrent flow-through measurements of time, latitude, longitude and temperature and salinity from a thermo-salinograph (CTD) will be used for correction of the ac-s $a(\lambda)$. This is important in order to correctly address the thermal, salinity and scattering (c-a) corrections that must be applied [WETLabs, 2011; Zaneveld et al., 1994]. All the flow-through data collected through the DH4 were time merged using WET Labs Archive Processing program (WAP) and hourly output archive files were generated. Hourly WAP archive files were then combined to create daily files. The daily WAP archive files were binned to 1 minute time bins to reduce the amount of data for spreadsheet import and processing.

The standard order of post processing protocol used (WetLabs 2011).

1. Remove sections of the data collected during the daily ac-s cleaning and pure water calibration.
2. Apply temperature and salinity corrections to ac-s a data using the coincident ship thermo-salinograph temperature and salinity data.
3. Temperature correct pure water calibration data for a and c.
4. Subtract the pure water calibration data from the in situ data.
5. Remove spikes in data due to bubbles, etc., using a σ filter and then interpolate
6. Scatter correct a_t [Zaneveld et al., 1994].
7. Add spectral pure water absorption coefficients [Pope and Fry, 1997] to measured $a_{t\text{-}w}$ to yield a_t.
8. Compute spectral scattering $b = c_t - a_t$

The post-processed a and c collected with the two ac-s instruments in the IOP flow-through system agree very well with less than 4% spectral differences between the two instruments (Figure 22).

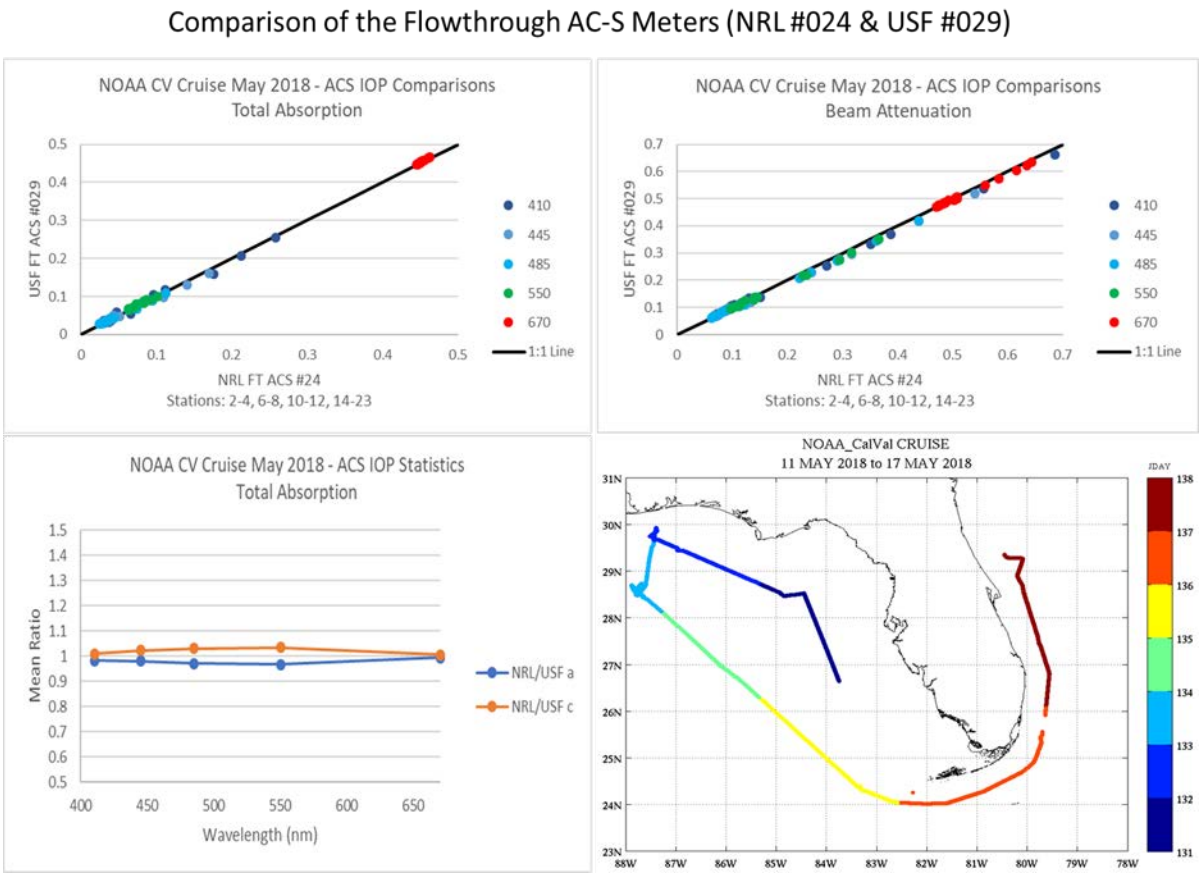

Figure 22. Comparisons of processed $a(\lambda)$ (top left) and $c(\lambda)$ (top right) of the NRL ac-s SN 024 and the USF ac-s SN 029. (Bottom left) The spectral ratio (NRL/USF) of both ac-s instruments for both $a(\lambda)$ and $c(\lambda)$. Instruments agree very well and uncertainty for both $a(\lambda)$ and $c(\lambda)$ is within 4%. (Bottom-right) The cruise track plotted with coverage by Julian Day (color bar) for the flow-through system.

Above Water Radiometry Measurements

Above-water remote sensing reflectance measurements were taken using Analytical Spectral Devices FieldSpec Handheld2 hyperspectral spectroradiometer (ASD) and Spectral Evolution Inc. PSR-1100F hyperspectral spectroradiometer on the bow of the *Okeanos Explorer*. Both spectroradiometers were calibrated for spectral radiance using NIST-traceable standards by both companies. The bow was selected to reduce the amount of contamination from the ship's structure on the collection of the calibrated reference plaques (NOAA grey, NOAA white and NIST blue) and the water's surface (Figure 9).

AWG measurements were acquired during 22 of the 24 stations, skipping Stations 5 and 9 because of time limitations (time of day, transit to next location). The AWG measured three reference plaques during the normal sky, water, and reference plaque sequence for deriving the above-water R_{rs}. These additional plaques were measured to access the uncertainty in the $R_{rs}(\lambda)$ between using the grey plaque versus the white plaque. The NOAA white plaque was appointed the standard reference to compute the above-water $R_{rs}(\lambda)$ by the AWG. The NOAA grey 10% was not collected by the Stennis Group beyond Station 12 to reduce time on station. The blue plaque (known colored reflective standard) was measured by all above-water radiometers as a Device Under Test (DUT) to test their performance and different collection protocols, i.e. if all radiometers collected the blue (known reflectance) and the white (reference) plaques at the same geometries then they should all give the same answers. The grey and white plaques have known BRDFs and are used to normalize the un-calibrated irradiance measurements for E_s. Answers may

vary due to instrument type and calibration, warm up time, shadowing of the plaques, BRDF differences for plaques, etc.

The AWG measurement activities took place on the bow of the *Okeanos Explorer*. At the start of each station, the reference plaques (grey, white, blue) were placed on the bow's bollard posts and made level using a small spirit level (Figure 9). The plaques were labeled to indicate which side to point to the Sun and from which direction to observe the target at relative azimuths of 90° or 135° and oriented accordingly. Plaques were monitored frequently for ship repositioning, movement, etc. and repositioned if necessary. The plaques were partially obscured from the full hemisphere by the ship's bridge, participants, and the bow rail. The magnitude of this bias will depend on how much of the diffuse component is blocked. The Stennis Group recorded station metadata (time, latitude, longitude, instrument base filenames, spectra target assignments and numbers, ocean parameters from ship's and IOP flow-through, physical water characteristics, meteorology, etc.) on hand written log sheets during each station. Other AWG personnel took photographs of the sky conditions and the participants in action. NOAA (C. Kovach) and NRL (S. Ladner) attempted to make concurrent measurements, starting with the ASDs. At the end of each station, the plaques and the radiometers (powered off) were placed in a water tight storage box on the bow.

The Stennis Group ASD instrument was configured to average five spectra and save five spectra for each target. The Spectral Evolution is designed to collect one spectra at a time and has to be triggered for each individual scan (10 scans per target). During each station, five consecutive radiometric spectrum with dark measurements subtracted were taken of each of the following targets: 1) grey/white plaques, 2) water, and 3) sky for the ASD. The same sequence was collected for the Spectral Evolution with 10 radiometric spectra per target. For both instruments, a fore optic (see Table 5) was attached, integration time was optimized for each target prior to collection (i.e., integration time of sensor was changed based on relative brightness of the target and new dark counts were taken to correct for instrument noise). The optical sensor zenith angles for the water (θ_{sfc}), gray card (θ_g), and sky (θ_{sky}) measurements were 40°, 40° and 40°, respectively. The relative azimuth angle of the sensor to the sun ranged from 90° to 135° depending on visual surface contamination (sea foam, glint, bubble, etc.).

Figure 23. Example ASD shooting the NOAA grey plaque and ASD shooting the water surface for water leaving radiance.

The post processing of the ASD and Spectral Evolution above-water data collected by the Stennis Group was performed by NRL using code developed by Nicholas Tufillaro (Oregon State University) and Ivan

Lalovic (GYBE LLC, Oregon State University) for the 22 stations collected and $R_{rs}(\lambda)$ was computed using the NOAA grey and white plaques with same protocols to look at inter-sensor uncertainty. Note that the five scans of ASD data for each target and station was averaged into three individual files (one for each target) and reformatted to an ASCII data format similar to the Spectral Evolution (.sed) file outputs for processing using the OSU / GYBE LLC software. Data from all groups/sensors for Stations 3, 7 and 10 were selected and will be processed by Ivan Lalovic to evaluate measurement differences between sensors using the same processing protocol/software. This post-processing software was selected as the standard because of the automated removal of outlier spectra, baseline-subtraction protocol used and the application of the surface reflectance correction ρ, based on the solar azimuth and wind speed calculation [Mobley, 2015]. This approach is a substantial improvement over using a constant ρ of 0.021 to minimize the reflected sunlight contribution.

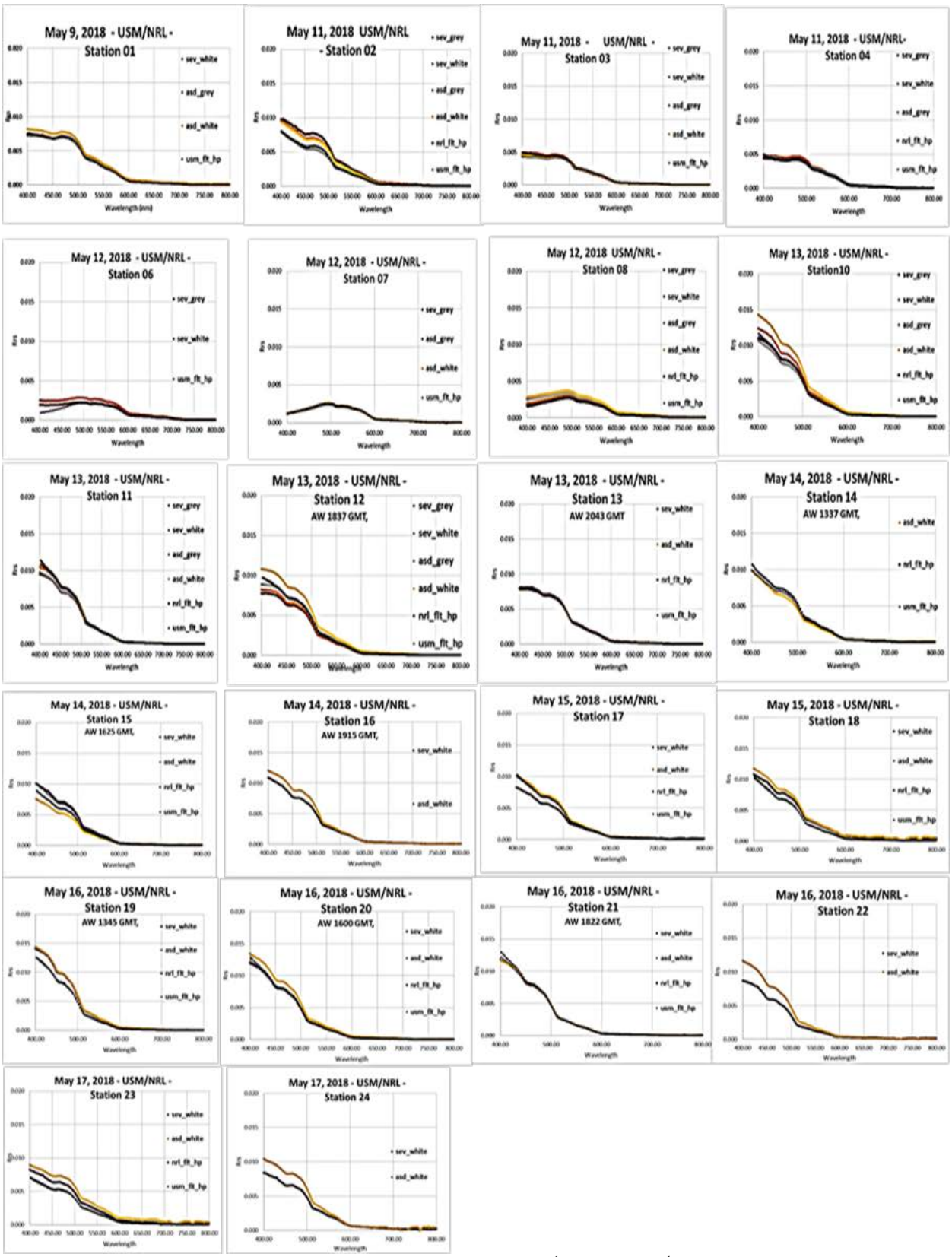

Figure 24. Above-water $R_{rs}(\lambda)$ (vertical axis on left from 0 sr^{-1} to 0.020 sr^{-1}) plotted for 22 individual stations for four different sensors and measurement types collected by the Stennis Group: Above Water

ASD with white plaque (gold line); Above Water ASD with grey plaque (grey line); Above Water Spectral Evolution with white plaque (orange line); Above Water Spectral Evolution with grey plaque (red line); NRL Hyperpro Float (black line); USM Hyperpro float (purple line). Horizontal axis is wavelength from 400 nm to 800 nm. Note for most stations the inner-sensor/plaque measurements agree very well. The same instrument ASD vice Spectral Evolution gave similar results with both the white and grey plaques.

Above Water Processing Protocols

The ASD Spectroradiometer measures light at 1.0 nm sampling over the 325 nm to 1075 nm spectral range. The SE PSR-1100-F Spectroradiometer measures light at 1.0 nm sampling over the 320 nm to 1100 nm spectral range. Processing follows the equation

$$R_{rs} = (S_{w+s} - S_{sky}\,\rho(\theta))/(\,\pi S_p/refl) \qquad (5)$$

where

- S_{w+s} is the measured signal from the water and includes both L_w and reflected skylight;
- S_{sky} is the measured signal from the sky;
- S_p is the average measured signal from the white and grey Spectralon plaques;
- *refl* is the reflectivity of the plaque (approximately 99% white and 10% grey; actual measured spectral values are used in the calculation); and
- π (p) converts the reflected radiance values to irradiance for these "Lambertian" diffusers.
- The measured sky radiance is multiplied by $\rho(\theta)$ which is the proportionality factor that relates the radiance measured when the detector views the sky to the reflected sky radiance measured when the detector views the sea surface.

The value of $\rho(\theta)$ is dependent on wind speed and direction, detector FOV, and sky radiance distribution. Only in the case of a level sea surface and a uniform sky radiance distribution does $\rho(\theta)$ equal the average of the Fresnel reflectance over the detector FOV. For our measurement angles under nominal sky and wind conditions, we pull $\rho(\theta)$ from Table 1 in Appendix 1 of Mobley [2015]. Note that these values are always significantly higher than the value 0.023 used for conditions of complete overcast and can vary both in magnitude and spectrally as a function of sea and sky conditions, wind speed and water type [Mobley, 2015; Mobley, 1999].

The computed R_{rs} should be "black" at about 750 nm due to water absorption. If not zero, then it is assumed that the S_{sky} was not estimated correctly. Following the "quick and easy" algorithm of [Carder and Steward, 1985], it is further assumed that any error in the skylight reflection term is white (not wavelength dependent) and one may simply subtract the computed $R_{rs}(750)$ from the entire spectrum. In practice, this may lead to negative reflectance values R_{rs} near 750 nm. Therefore, the processing subtracts the smallest $R_{rs}(\lambda)$ in the range from 700 nm to 800 nm (Equation 6). To compare the in situ reflectance with satellite-derived reflectance, the mean reflectance is computed using the relative spectral response tables for each band of the sensor (VIIRS).

Cruise Comparison of In-water Floating Hyperpros and Above-water R_{rs}

The $R_{rs}(\lambda)$ station data collected for the Stennis in-water Floats (pictured in Figure 7B) and above-water handheld sensors (as pictured in Figure 9) show similar spectral shapes and are within about 20% at Station 11 with a bit wider spread at Station 12 (Figure 25). Other stations show similar results.

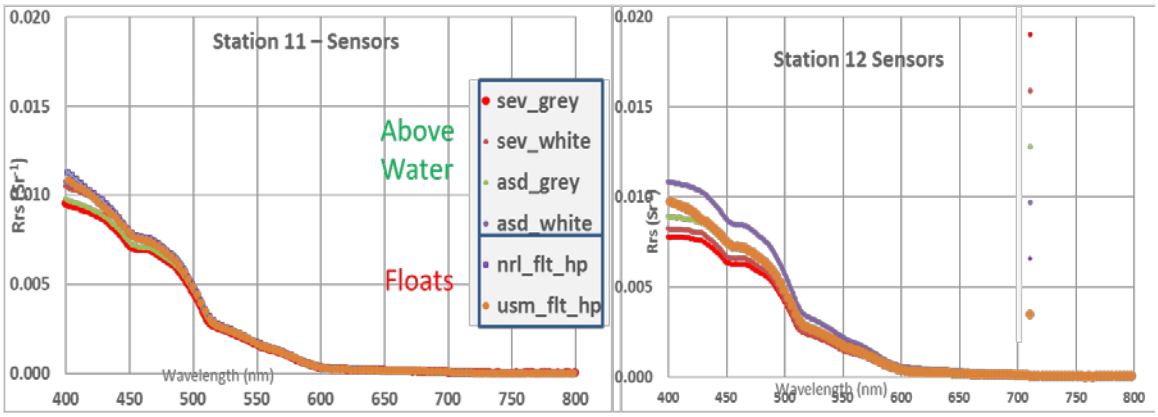

Figure 25. Comparison of $R_{rs}(\lambda)$ for all above- and in-water Stennis sensors at Station 11 (left) and Station 12 (right) for floating Hyperpros (USM_flt_hp and NRL_flt_hp) and above-water ASD, Spectral Evolution (sev) using grey and white plaques. Similar results found at the other stations.

Brief Collection Summary

- The cruise departed Key West, FL and adaptively transited into the northern Gulf of Mexico for increase chances of station collection in cloud free areas. The cruise track sampling occurred in the northern Gulf of Mexico, Loop Current and eddies and finally followed the Gulf Stream to Jacksonville, FL.
- The Stennis Group successfully collected 22 stations of in-water and above-water $R_{rs}(\lambda)$ measurements and 9 consecutive days of continuous underway flow-through IOP data. SNPP and NOAA-20 had a combined 21 overpasses from May 9 to May 17 for matchups with the NOAA MSL12 processed data.
- Comparisons of $R_{rs}(\lambda)$ from the two floating Hyperpros (NRL and USM), collected at the same station time and locations, showed excellent agreement, within about 0.2% overall. The floating Hyperpro $R_{rs}(\lambda)$ data were processed similar and calibrated using the same NIST traceable source at NOAA as the profiling Hyperpros.
- The processed above-water $R_{rs}(\lambda)$ data for both the ASD and Spectral Evolution using both the grey (when available) and white plaques was compared with the in-water $R_{rs}(\lambda)$ data collected by both the USM and NRL floating Hyperpros. Comparisons resulted in good agreement, within about 20%, between the above-water and in-water instruments collected and processed by the Stennis Group and are being evaluated.
- The location of the ship during the sensor deployment at each station can change which may lead to a change in center satellite pixel. We have recorded the location and time of deployment and completion for each sensor group that was deployed at each station in the cruise log. Some stations do not all have the same center satellite pixel to be used for a matchup. We have plots of the differences in the center pixel for different locations at the stations. This can also be used for matchup uncertainty.
- The flow-through IOP data post processing is complete and inter-sensor comparisons and matchups with VIIRS sensors are being evaluated and quality controlled to provide continuous measurements along the ship track to determine the spatial variability at each station location for the duration of sampling and the entire cruise track for establishing water masses and features. These data are being processed using the Wet Labs 2011 IOP protocol.

11.3 CCNY – Alex Gilerson, Ahmed El-Habashi, Carlos Carrizo, Eder Herrera and Sam Ahmed

The primary instrument used by the CCNY group for above-water observations in the validation process was the GER (SpectraVista, NY). On this cruise, the first measurements were made with the novel snapshot hyperspectral imager, UHD285, (Cubert, GmbH Germany). In addition, AOT was measured by a Microtops sunphotometer (Solar Light, PA) at 5 wavelengths: 380 nm, 500 nm, 675 nm, 870 nm and 1020 nm.

Handheld spectroradiometer

The GER 1500, Field Portable Spectroradiometer, is a handheld spectroradiometer designed to provide fast spectral measurements covering the UV, Visible and NIR wavelengths from 350 nm to 1050 nm at 3 nm full width half maximum (FWHM) resolution. It uses a diffraction grating with a silicon diode array that has 512 discrete detectors and provides the capacity of reading 512 spectral bands. A total of 482 spectral readings can be stored within its memory. Subsequent download and analysis is done using a personal computer with a standard RS232 serial port and the GER 1500 licensed operating software. The GER 1500 is equipped and operated with a standard lens with 4° nominal FOV for above-water observations. The GER 1500 is used in the field to calculate $R_{rs}(\lambda)$ by measuring the L_t above the sea surface, L_{sky} and L_d.

The instrument has undergone radiometric and wavelength calibration in the optics mode (with the lens) at the manufacturer in November 2016. Generally, due to the nature of the measurement, calibration is not necessary.

In order to acquire L_t, the instrument was placed at the azimuth angle 90° from the sun and 40° viewing angle from the nadir and four consecutive measurements were made. The sky radiance was measured by pointing the instrument at the sky at the same azimuth angle and 40° viewing angle from the nadir also with four consecutive measurements. L_d data were obtained by pointing the instrument at the Spectralon reference plaque at 40° viewing angle; also four consecutive measurements were made. Typically, a white reference plaque was used. In addition, at some stations a grey plaque (from other groups) and the NIST blue plaque were used as well. All measurements were executed in TAR (target) mode. Downwelling irradiance is determined as $E_d = \pi * L_d/A$ where $A \approx 0.97$ (the full spectrum from the manufacturer was used in the processing) and is the reflectance factor of the white target according to the manufacturer calibration for the whole spectral range (ZenithLiteTM, SphereOptics GmbH). $R_{rs}(\lambda)$ is calculated by the following equation $R_{rs} = (L_t - r*L_s)/E_d$ where r is the sea surface reflectance factor. Values of r for un-polarized reflectance [Mobley, 1999] and polarized reflectance [Mobley, 2015] were used and resultant R_{rs} spectra were compared. For each station, the averages of all individual scans for L_t, L_s and L_d were used in $R_{rs}(\lambda)$ calculations. Since most of measurements were carried out in relatively clear and light coastal waters, $R_{rs}(750)$ was subtracted from the entire R_{rs} spectrum to eliminate sun glint effects [Mobley, 1999]. Integration time is self-adjusted by the instrument and was typically 160 ms for water observations. It should be noticed that in Mobley [1999] and Mobley [Mobley, 2015], r coefficients were calculated for one wavelength at 550 nm and without taking into account impact of AOT, which can change r values at 550 nm and spectrally [Gilerson et al., 2018]. Additional processing will be carried out to analyze these effects.

Snapshot Hyperspectral Imager

A Snapshot Imaging Spectrometer UHD285 (Cubert, Germany; Figure 26) with no moving parts permits acquisition of the spectral cube in the visible/NIR with a FOV of 40°. Following the objective lens, a 50:50 cubic non-polarizing beam splitter divides the light with half the flux from the object directed to the first photo-detector matrix for acquisition of a panchromatic image in 450 nm to 1000 nm wavelength range with a spatial resolution of 1000 x 1000 pixels while the other half of the flux is modified by a microlens array, collimated, spectrally split using a prism and finally focused on the second detector matrix. After processing with Cubert's proprietary algorithm, spectra are available for 50 x 50 spatial

pixels and 138 wavelengths with a sampling interval of 4 nm. The entire system can collect images with a frame rate of up to 20 cubes s^{-1} and 14 bit digitization. The instrument weighs about 3 kg and its dimensions are 280 mm in length and 100 mm in diameter, which makes it suitable for various field measurements.

Because a prism is used as the dispersive element in the imager, the spectral bandwidth strongly depends on the wavelength with FWHM of ≈5 nm at 450 nm and ≈30 nm at 900 nm. The non-scanning feature eliminates the necessity of the continual movement required by push-broom imagers. The UHD285 imager underwent laboratory calibration at CCNY by the comparison of radiances reflected from a white Lambertian plate standard (ZenithLiteTM, SphereOptics GmbH) with the radiances measured by the GER spectroradiometer. A typical integration time for ocean observations with the imager is 20 ms to 50 ms. The imager was installed on the tripod with the main axis at 90° (270°) azimuth angle from the Sun, typically 40° viewing angle from the nadir (with some measured deviations) for L_t measurements and at 40° viewing angle from the zenith for the L_{sky} measurements. E_s was measured independently by the HyperOCR E_d sensor (Satlantic, Canada) installed on the pole in an unobstructed area on the ship. All L_t, L_s and L_d sensors were calibrated at CCNY with a NIST traceable radiance source. E_s sensors were calibrated at Satlantic before the 2015 cruise and at the NOAA facility after the 2015 cruise.

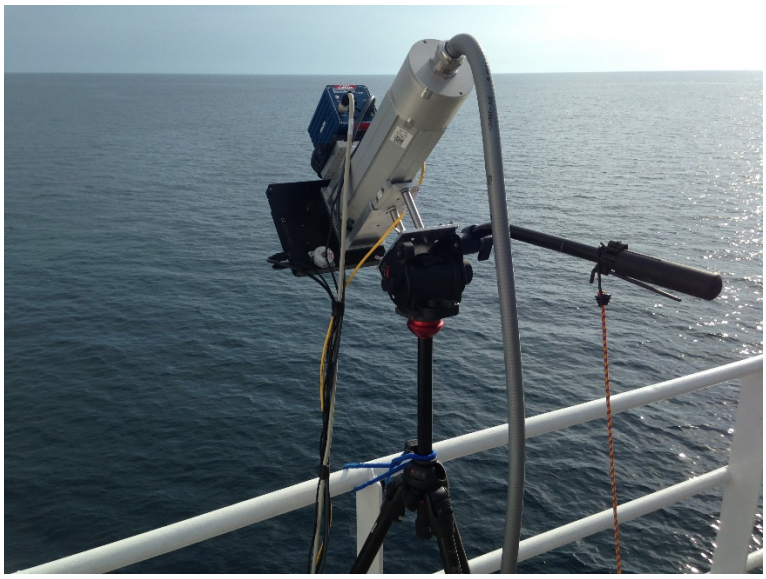

Figure 26. Snapshot Hyperspectral Imager on the ship mounted along the rail of the ship.

Preliminary results

Comparison of spectra measured by GER with VIIRS/SNPP and VIIRS/NOAA-20 satellite data for Station 8 (coastal water) and Station 11 (blue water) are shown in Figure 27. Satellite data are from MSL12 science quality processed by the NOAA Ocean Color team (Dr. M. Wang group). Figure 28 demonstrates the high potential of the UHD285 for accurate above-water observations as compare with GER results from Station 11 in the Gulf of Mexico. Sky images (not shown) are taken by the camera installed on the UHD285 snapshot imager.

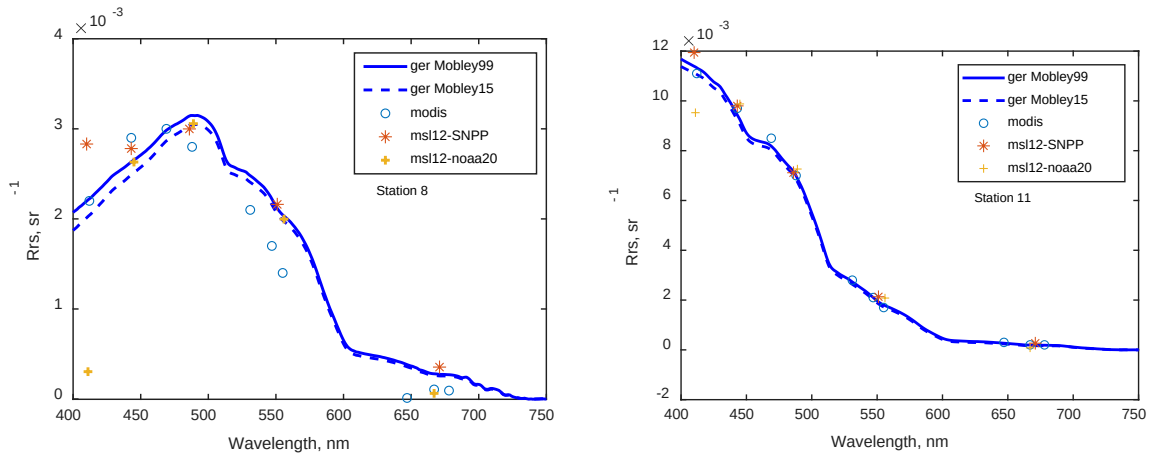

Figure 27. Comparison of measured spectra by GER with satellite data: (left) for coastal waters at Station 8 and (right) for open ocean at Station 11. GER spectra are processed with *r* from Mobley [1999] and Mobley [2015].

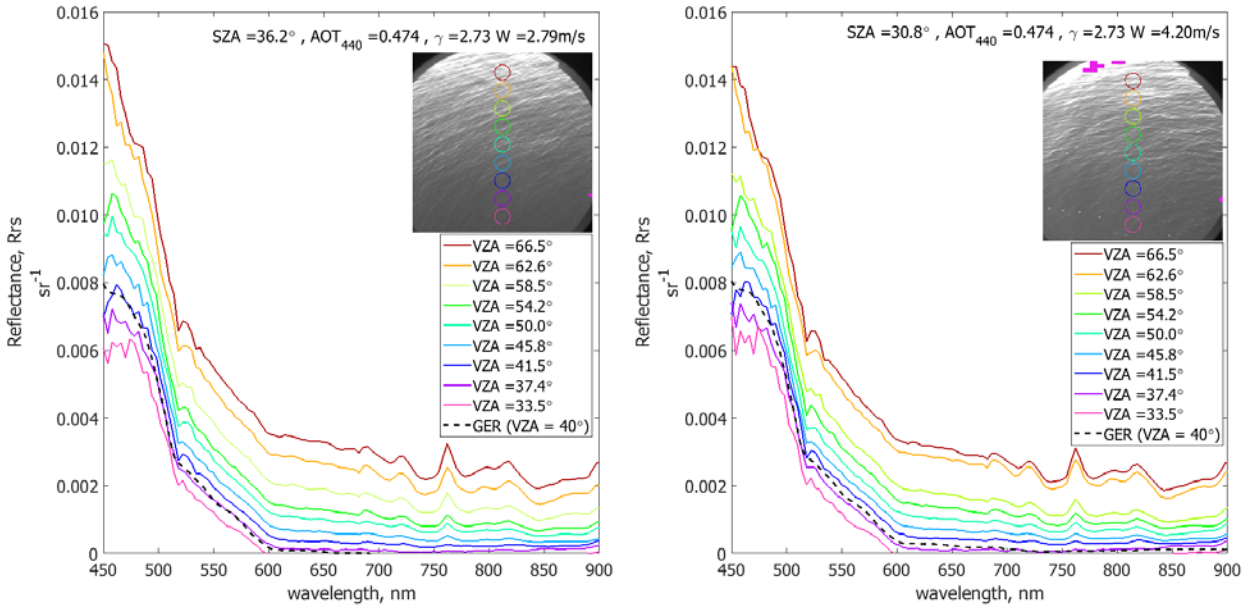

Figure 28. Example of the snapshot imager R_{rs} spectra for different viewing angles plotted with GER for two observations on 13 May 2018 at Station 11 in the Gulf of Mexico: a) 16:13 UTC b) 16:38 UTC

11.4 LDEO – Joaquim I. Goes, Helga do Rosario Gomes and Kali McKee

Phytoplankton community composition, size structure and photosynthetic efficiency measurements were made 1) from discrete water samples collected from the CTD and collected from the underway flow-through system and 2) from the continuous near surface water supply from the underway flow-through system. Water samples for nutrient analyses were also collected at stations. The resources for analyzing these have yet to be identified.

Discrete Samples

At each station, aliquots of seawater samples from the CTD rosette (coincident with sampling for HPLC pigments) were collected for the following:

i) Microscopic analysis of phytoplankton community composition and sizes.
ii) Counting, imaging and size estimations of phytoplankton and other detrital particles using a Fluid Imaging Technologies, Inc., FlowCAM.
iii) Estimates of phycobilipigments
iv) Fluorescence based estimates of

- Chl-*a*
- CDOM
- Phycobilipigments: Phycoerythrin-1 (PE-1; peak at 565 nm), Phycoerythrin-2 (PE-2; peak 578 nm) and Phycoerythrin-3 (PE-3; peak at 590 nm)
- Variable fluorescence (F_v/F_m, a measure of phytoplankton photosynthetic efficiency) using a WET Labs Advanced Laser Fluorometer (ALF) [Chekalyuk et al., 2012; Chekalyuk and Hafez, 2008; Goes et al., 2014a]

v) Measurements of F_v/F_m and the functional absorption cross-section (σ) of Photosystem II (PSII) in a mini-Fluorescence Induction and Relaxation (FIRe)® Fast Repetition Rate Fluorometer (FRRF) [Gorbunov and Falkowski, 2004] as well as the electron transport rates (ETR) essential for measurements of net primary productivity.

i. Microscopy based phytoplankton identification and cell counts

For microscopic identification and enumeration of phytoplankton, samples were collected in 100 mL screw top hard plastic bottles from three depths and at 24 stations (coincident with HPLC pigment analysis). Samples were fixed with 1% alkaline Lugol's iodine, preserved in 1.5% solution and were stored under dark and cool conditions. Microscopic analysis is currently underway and includes overnight settling of 10 mL samples in an Ultermohl counting chamber and then counting the samples using a Nikon® inverted microscope at 200X and 400X magnifications. The smallest cells that can be enumerated by this method are <5 μm in diameter. Phytoplankton identifications are based on standard taxonomic keys [Tomas, 1997]. Cryptophytes are being identified by epifluorescence microscopy using their yellow-orange fluorescence signatures [Booth, 1993; Goes et al., 2014b; MacIssac and Stockner, 1993].

ii. FlowCAM based phytoplankton identification, cell counts and cell sizes

In addition to the microscopic analysis of phytoplankton, 2 × 25 mL aliquots of the preserved samples are being analyzed for phytoplankton community composition and size structure analysis using a FlowCAM particle imaging system equipped with a 4X objective (UPlan FLN, Olympus®) and a 300 μm Field-of-View flow cell. Field-of-View flow cells ensure that the liquid passing through the flow cell is entirely encompassed within the camera's FOV. Phytoplankton cells within the preserved samples will be counted and imaged in auto-image mode with a peristaltic pump rate of approximately 0.32 mL min^{-1} to 0.44 mL min^{-1} as specified by the manufacturer. Cells will be classified to the genus-level using the Visual Spreadsheet program (v. 2.2.2, Fluid Imaging). The instrument provides the total number of particles imaged, together with the dimensions of each particle allowing estimations of phytoplankton community structure, particle size distribution of both phytoplankton and of detrital particles (Figure 29).

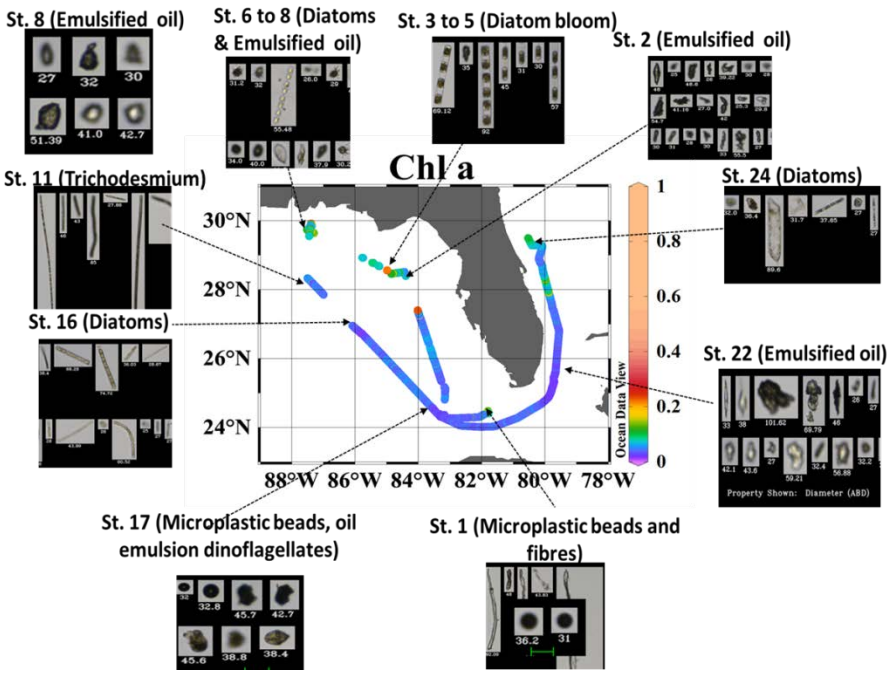

Figure 29. Preliminary particle imaging data (10 images) are shown with an underway map of Chl-*a* concentration from the ALF (color bar in relative fluorescence units (RFU)) revealed that the surface waters of the central and southern Gulf of Mexico are dominated by emulsified oil particles and microplastic beads. Stations 3 to 5 were dominated by the diatom *Hemiaulus* sp. *Trichodesmium* sp. was the dominant species at Station 11.

iii. Phycobilipigment collection and analysis

Approximately 1 L to 2 L of seawater samples from three depths (coincident with the depths sampled for HPLC pigment analysis) at each station were carefully filtered onto four 25 mm Whatman GF/F, glass microfiber filters for analysis of estimating phycoerythrin and phycourobilin pigments. Samples were immediately stored in liquid nitrogen for later analysis at LDEO which rely on freezing, sonication and extraction of the phycobilipigments in phosphate buffer and analysis in a spectrofluorometer.

iv. Automated Laser Fluorescence (ALF) measurements of phytoplankton groups

The ALF combines high-resolution spectral measurements of blue (405 nm) and green (532 nm) laser-stimulated fluorescence with spectral deconvolution techniques to quantify fluorescence of Chl-*a* (peak at 679 nm), three phycobilipigment types (PE-1, PE-2 and PE-3), CDOM (peak at 508 nm) and variable fluorescence (F_v/F_m). All fluorescence values obtained are normalized to the Raman spectra of seawater and generally expressed as relative fluorescence units (RFU), whereas F_v/F_m is dimensionless. PE-1 type pigments are associated with blue water or oligotrophic cyanobacteria with high phycourobilin/phycoerythrobilin (PUB/PEB) ratios, PE-2 type phytoplankton with low-PUB/PEB ratios are generally associated with green water cyanobacteria that usually thrive in coastal mesohaline waters, and PE-3 attributable to eukaryotic photoautotrophic cryptophytes [Chekalyuk et al., 2012; Chekalyuk and Hafez, 2008; Goes et al., 2014b]. RFU values for Chl-*a* can be converted into mg m^{-3} Chl-*a* values using least square regressions of extracted Chl-*a* analyzed by HPLC or fluorometry vs. RFU values for Chl-*a* measured in an ALF.

All samples for the ALF were collected directly from the Niskin samplers into 500 mL acid-washed amber glass bottles and stored for about 30 min in the dark at temperatures close to the average surface seawater temperature at each station. Dark adaptation allows all the PSII reaction centres and electron acceptor molecules of phytoplankton to become fully oxidised and hence available for photochemistry

thus minimizing the impacts of non-photochemical quenching before analysis.

v. Fluorescence Induction and Relaxation (FIRe) measurements of photosynthetic efficiency

The FIRe technique was developed to measure a comprehensive suite of photosynthetic and physiological characteristics of photosynthetic organisms [Bibby et al., 2008; Gorbunov and Falkowski, 2004]. This technique provides a set of parameters that characterize photosynthetic light-harvesting processes, photochemistry in PSII, and the photosynthetic electron transport down to carbon fixation (see Figure 30 for example of flow-through FIRe data). Because these processes are particularly sensitive to environmental factors, the FIRe technique can be utilized to provide a measure of natural (nutrient limitation, photoacclimation and photoinhibition, thermal and light stress, etc.) and anthropogenic stressors (such as pollution). One property that is unique and the most sensitive to environmental stressors is F_v/F_m (or the photosynthetic quantum yield of photochemistry in PSII). In addition to F_v/F_m, we measured the σ_{PSII}, which is a product of the optical absorption cross section or the physical size of PSII unit and the quantum yield. In addition, we made measurements of the connectivity factor (*p*), which is a measure of excitation energy transfer between individual photosynthetic units of PSII. All optical measurements by the FIRe are sensitive, fast, non-destructive, and can be done in real time and in situ and can provide an instant measure of the photosynthetic competency of the cells.

Underway flow-through measurements

Between stations, the ALF, the FlowCAM and the mini-FIRe were connected in parallel to the ship's seawater flow-through system, allowing for continuous in-water measurements of phytoplankton community composition, phytoplankton size, phycobilipigment types and F_v/F_m. With the exception of a few breaks during stations and for reconditioning, all four instruments were operated over the entire cruise track, providing several thousand fluorescence based measurements of F_v/F_m and σ_{PSII} and *p* (Figure 30**.**), Chl-*a* and CDOM (Figure 31), PE-1, PE-2, PE-3, as well as continuous FlowCAM images that will allow high resolution measurements of phytoplankton composition and cell size distribution necessary for interpreting the optical measurements within and outside of physical oceanographic features encountered in the Gulf of Mexico and along the East coast Florida shelf.

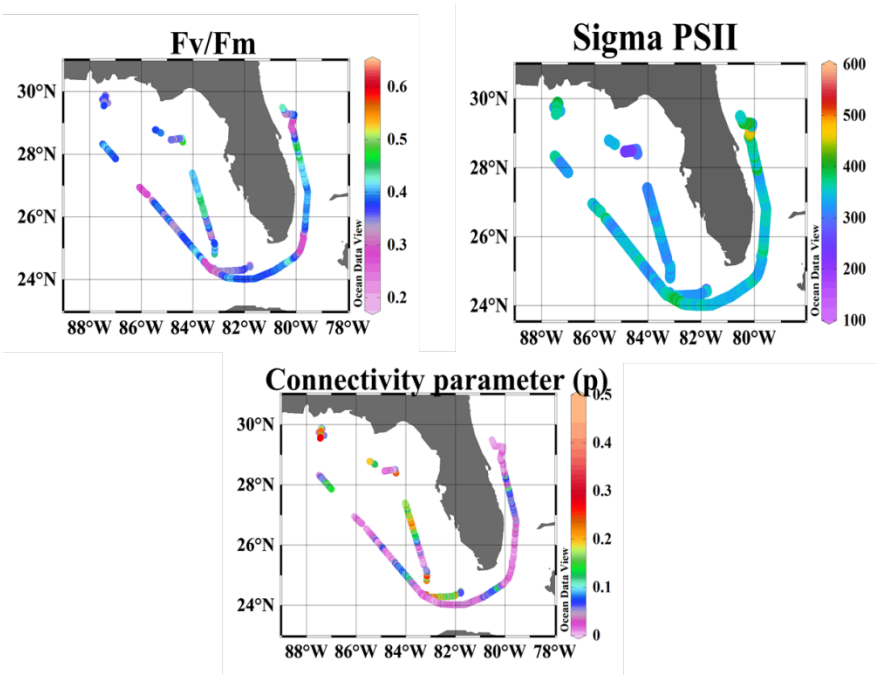

Figure 30. Preliminary analysis of flow-through FIRe data along the A) cruise track showing the photo-physiological characteristics of: (top left) F_v/F_m (dimensionless), (top right) σ_{PSII} ($Å^2$ $quanta^{-1}$, which is equivalent to SI units of 10^{-10} m^2 $electron^{-1}$) and (bottom) *p* (the connectivity factor, unitless).

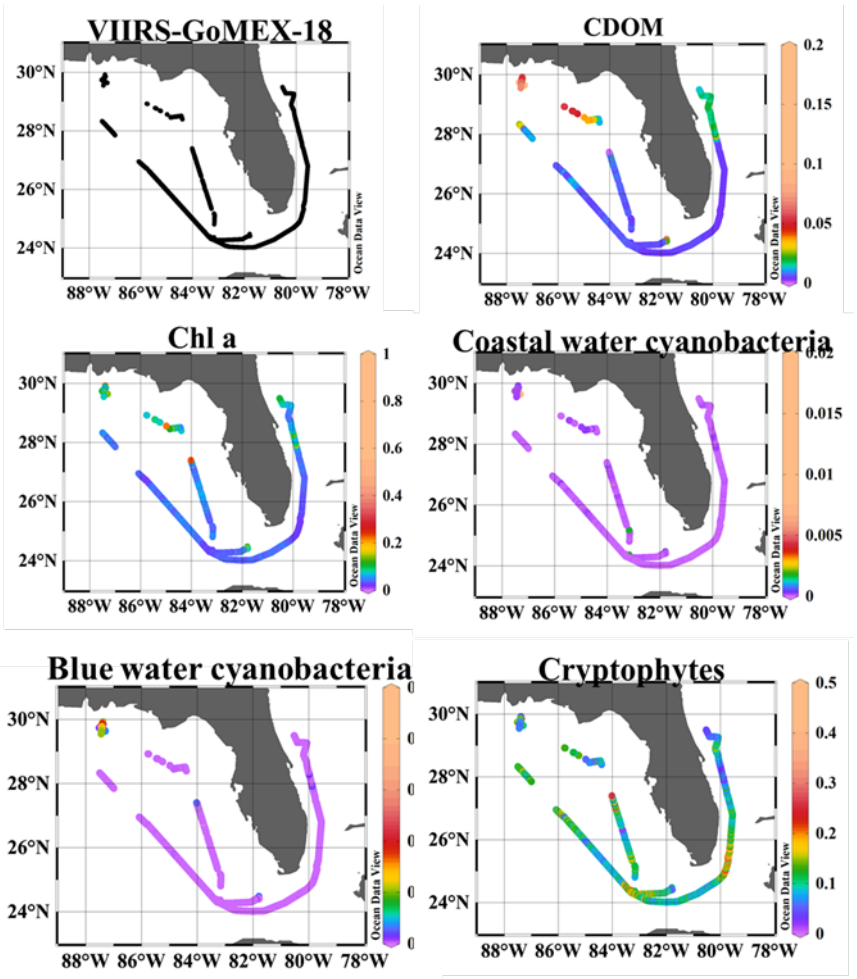

Figure 31. Preliminary analysis of flow-through ALF data along the (top left) cruise track showing the distribution of (top right) CDOM, (middle left) Chl-*a*, (middle right) coastal cyanobacteria, (bottom left) open water cyanobacteria, and (bottom right) cryptophytes measured as RFU.

11.5 USF Optical Oceanography Laboratory - Chuanmin Hu, Jennifer Cannizzaro, Yingjun Zhang, Chih-Wei Huang, and David English

Spectral absorption and pigment determinations

Measurements of the light absorption due to the particulate and dissolved components of water samples are used for understanding and modeling of the underwater light field, as well as the development of remote sensing and primary productivity algorithms. Shortly after collection, a subset of the water samples from the CTD rosette or surface underway system were filtered through a glass fiber filter to allow later spectral measurements of the light absorption by particles in the water. A portion of the filtrate was also reserved for a shore-based measurement of the spectral absorption of the dissolved material, $a_g(\lambda)$, in these water samples. The extraction of the particulate pigments allows the separation of the total

particulate absorption, $a_p(\lambda)$, into a living or pigmented fraction, $a_{ph}(\lambda)$, and detrital fraction, $a_d(\lambda)$ [Kishino et al., 1985]. The extraction of the pigments also allows a fluorometric determination of the Chl-*a* concentration [Holm-Hansen and Riemann, 1978; Welschmeyer, 1994].

During this EX-18-04 cruise, 54 water samples were filtered for particulate absorption analysis. There were 31 samples collected from surface waters and 23 from waters located at depths greater than 15 m (Table 1). These samples have been processed to determine $a_p(\lambda)$, $a_d(\lambda)$, $a_{ph}(\lambda)$, $a_g(\lambda)$ and Chl-*a* concentrations. Additional filter samples are reserved for possible HPLC pigment analysis at NASA/GSFC.

Table 11. Time and depth of water samples collected for particulate absorption analysis.

Date (UTC)	Time (UTC)	Cast or underway ID	Sample Depths (m)
5/9	21:25	1	1,45, 65
5/10	22:30	ALFA 001	near-surface
5/11	13:25	2	3,34
5/11	16:23	3	4,35,45
5/11	20:39	4	3,19, 38,50
5/11	21:48	5	near-surface
5/12	13:17	6	4,33, 52
5/12	16:28	7	4,27
5/12	20:37	8	3,15,24
5/12	21:50	9	near-surface
5/13	13:13	10	4,90
5/13	15:49	11	4,81, 95
5/13	19:59	12	4,60, 85
5/13	21:18	13	near-surface
5/14	4:10	Eddy1	near-surface
5/14	4:39	Eddy2	near-surface
5/14	9:35	Eddy3	near-surface
5/14	12:59	14	3,30
5/14	16:47	15	4,50
5/14	20:10	16	4,60, 90
5/14	23:17	Eddy4	near-surface
5/14	23:56	Eddy5	near-surface
5/15	1:13	Eddy6	near-surface
5/15	2:56	Eddy7	near-surface
5/15	14:44	17	4,55
5/15	18:20	18	near-surface
5/16	13:36	19	near-surface
5/16	15:57	20	near-surface
5/16	19:24	21	near-surface
5/16	20:50	22	near-surface
5/17	14:22	23	near-surface

Above-water remote sensing reflectance

Above-water $R_{rs}(\lambda)$ was collected at most of the stations using an ASD. The $R_{rs}(\lambda)$ measurements were made by comparing spectral radiance measurements of both the water's surface and the sky to a reference plaque [Carder and Steward, 1985; Mueller et al., 2003b]. An ASD Handheld2 Pro with a 7.5° FOV and a gray reflectance plaque (≈ 10% reflectance) with measured spectral and angular reflectance characteristics were used to determine $R_{rs}(\lambda)$. The ASD viewed the reflective reference from >30 cm above the reflectance plaque from nadir, while the sea-surface and sky measurements were made with 40° to 45° nadir and zenith viewing angles.

While the ASD was able to obtain the spectral radiance measurements, a problem with the instrument prevented retrieval of all the spectra from the instrument (about 40% of the spectra could be retrieved). Because of the loss of spectra, $R_{rs}(\lambda)$ could be computed for only 9 stations. Example $R_{rs}(\lambda)$ estimates are shown in Figure 32. Additional measurements were made of several reference plaques and the NIST blue tile, but the number of measurements that could be retrieved was also reduced by the instrument problem.

In-water radiometry

Vertical profiles of the near-surface water light field were collected using a Satlantic HyperPro-II. The HyperPro-II includes $L_u(\lambda,z)$ and $E_d(\lambda,z)$ sensors, as well as sensors for measuring pressure, temperature, conductivity, $b_b(660)$, and both Chl-*a* and CDOM fluorescence. At 18 stations of EX-18-04, the $L_u(\lambda,z)$ and $E_d(\lambda,z)$, measurements from multiple casts were used to estimate sea surface conditions such as $L_w(\lambda,0+)$ and $E_d(\lambda,0+)$, $R_{rs}(\lambda)$, and $nL_w(\lambda)$. For example, Figure 33 shows some of the $R_{rs}(\lambda)$ estimates made using the HyperPro-II measurements. USF's HyperPro system was deployed using the manufacturer's recommended protocol [Satlantic, 2004, 2003] in coordination with the HyperPro profiling group.

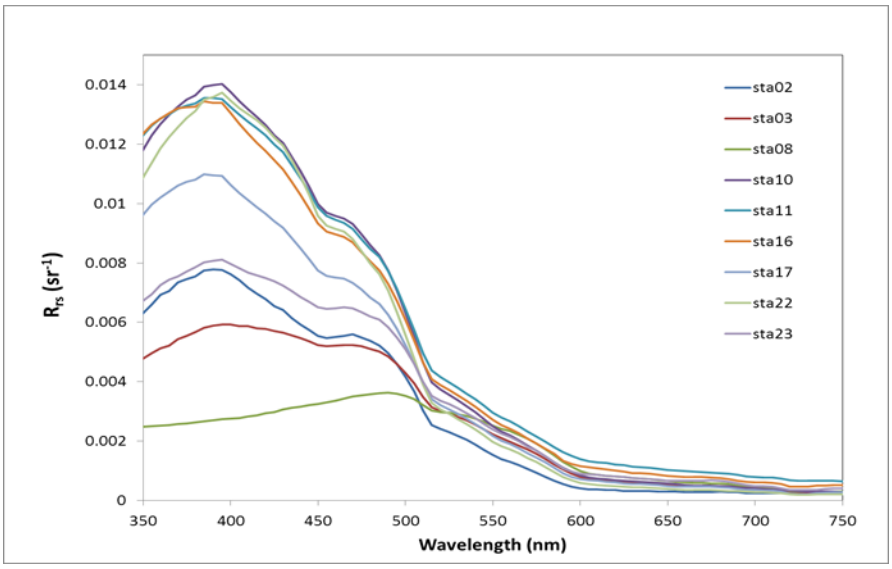

Figure 32. Preliminary above-water $R_{rs}(\lambda)$ from ASD measurements at 9 stations of EX-18-04.

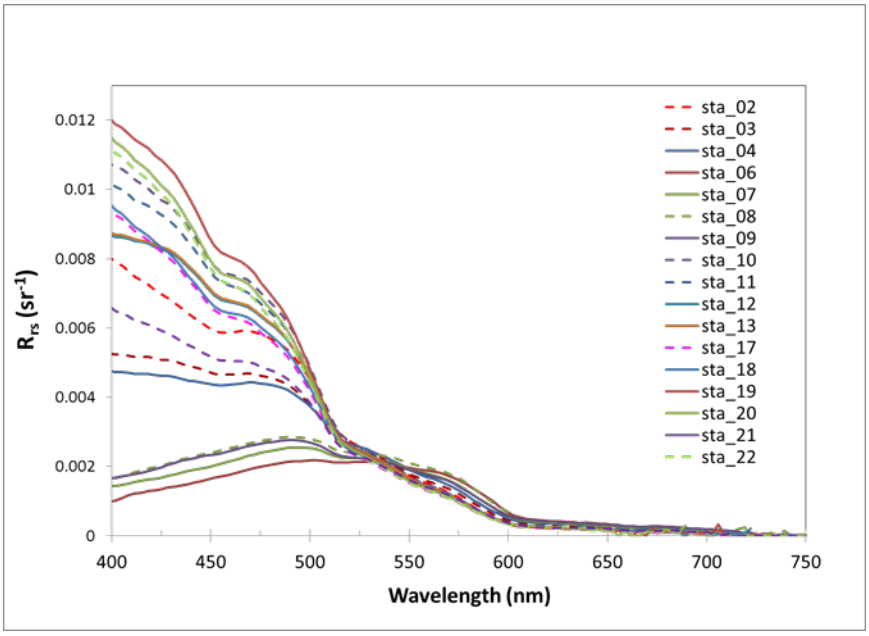

Figure 33. Preliminary $R_{rs}(\lambda)$ estimated from HyperPro-II profiles at EX-18-04 stations.

Underway flow-flow measurements using the WETLabs ALFA system

The WETLabs Aquatic Laser Fluorescence Analyzer, ALFA, is a laser stimulated fluorescence measuring system that uses blue (405 nm) and green (515 nm) lasers and spectral deconvolution software to assess phytoplankton pigment concentrations and physiological status and CDOM concentration. Some of the measurements that the ALFA system produces are fluorescence due to Chl-*a* and CDOM, F_v/F_m, and fluorescence of several phycoerythrin pigments [Chekalyuk et al., 2012; Chekalyuk and Hafez, 2008]. During EX-18-04, the ALFA system used some of the water from the ship's flowing seawater system to provide a continuous sequence of measurements throughout most of the cruise. These are combined with information about the ship's location to create plots of the near-surface water fluorescent properties (e.g. Figure 34). Analysis of the ALFA data is progressing, and the results of the water sample analysis are used to validate the ALFA estimates.

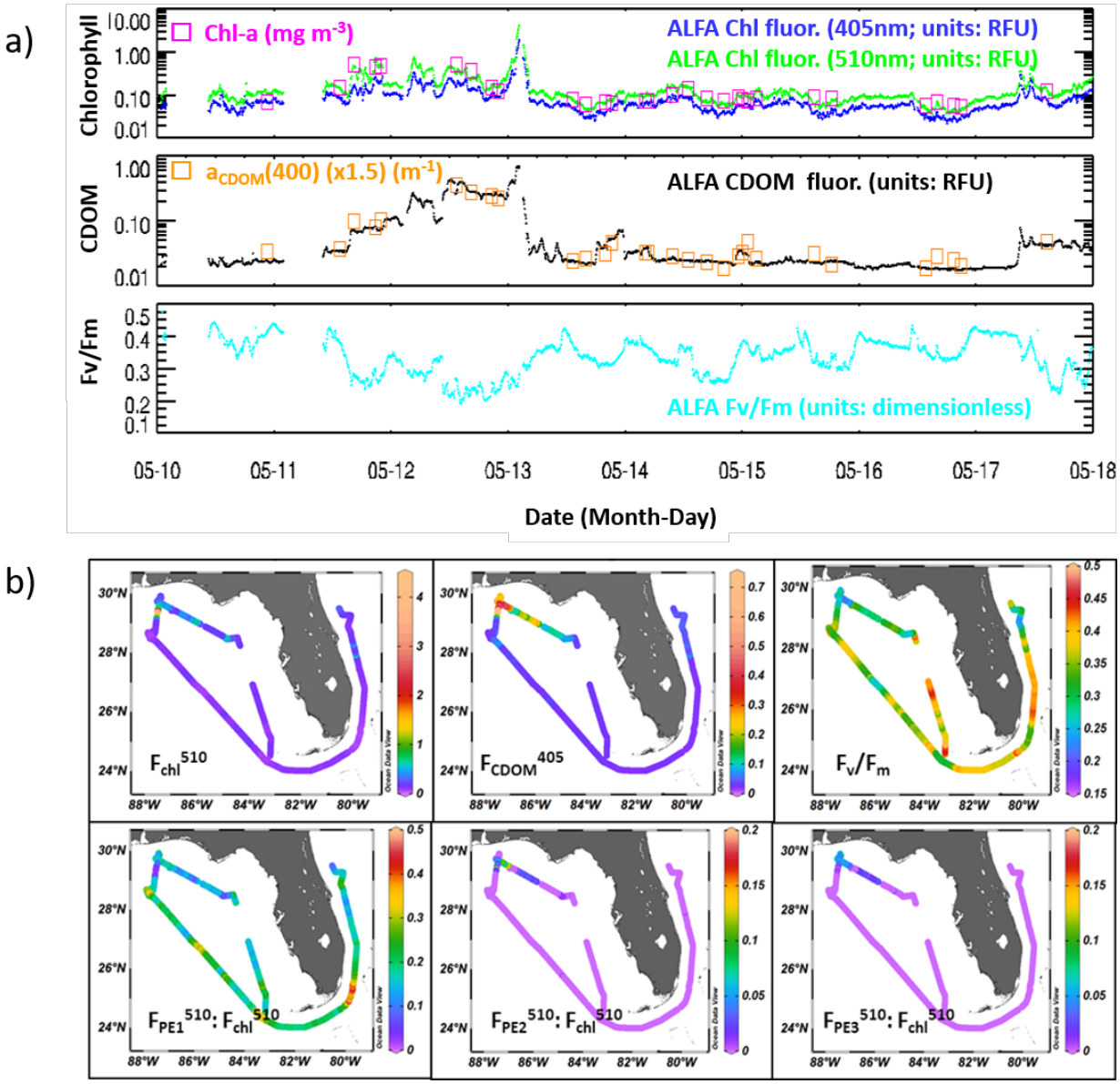

Figure 34. Example of ALFA measurements by USF. a) A time-series of Raman-corrected fluorescence for Chl-*a* using the green and blue lasers, respectively (top), CDOM fluorescence (middle), and F_v/F_m (bottom) b) Examples of the spatial variability of near-surface Raman-corrected Chl-*a* fluorescence (upper left), CDOM fluorescence (upper middle), F_v/F_m (upper right), and fluorescence of PE1 (indicative of oceanic cyanobacteria), PE2 (indicative of coastal cyanobacteria), NS PE3 (indicative of cryptophytes) in the bottom panels.

11.6 NIST—B. Carol Johnson

The NIST blue tile is a reflectance target made from two pieces of 3.8 mm-thick, 16.51 cm square, F65 plate glass. The configuration of the blue tile target was identical to the 2016 cruise [Ondrusek et al., 2017]. Briefly, the surface of one of the glass plates was roughened by sandblasting to create a diffuse surface. Then the two plates were stacked together, with the diffuse surface on the top, and held in a 30.48 cm-square by 2 cm thick-black plastic mounting cell. The glass plates are mounted in a 7.6 cm-deep square area centered in the black plastic cell. This results in the ground optical surface of the blue tile flush with the top of the black plate, see Figure 35. A wooden storage container with a cutout on the

inside of the top lid holds the blue tile and prevents anything touching the optical surface during storage or shipment. The bottom half of the storage container has two cutouts for ease of removal of the blue tile assembly from the storage container. Alignment indicators, labeled “point to Sun” and “90° azimuth” were placed on the surface of the mounting cell prior to the 2015 *Nancy Foster* cruise (blue tape in Figure 35).

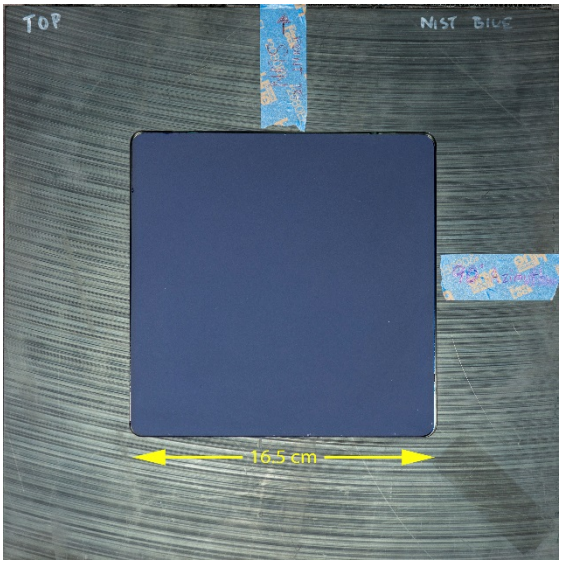

Figure 35. Photograph of the NIST blue tile in its black plastic mounting cell

The NIST blue tile in plane bidirectional reflectance *factor* (BRF) for normal incidence and 45° view from nadir (BRF is equal to π times the BRDF), or BRF(0,45;λ), was measured on a Cary 14 in May 2012 using a white Spectralon plaque as the reference. The reference plaque was calibrated in the NIST Spectral Tri-function Automated Reference Reflectometer (STARR) facility [Proctor and Barnes, 1996]. In October 2014 and February 2015 the BRF(0,45;λ) was determined using STARR, and in April 2018 the NIST Robotic Optical Scatter Instrument (ROSI) did measurements at 410 nm. The results are presented in Figure 36. The gray lines are the $k = 2$ uncertainties for the STARR 2014 data, demonstrating the results agree within their expanded uncertainties. We conclude the reflectance of the blue tile is stable in time.

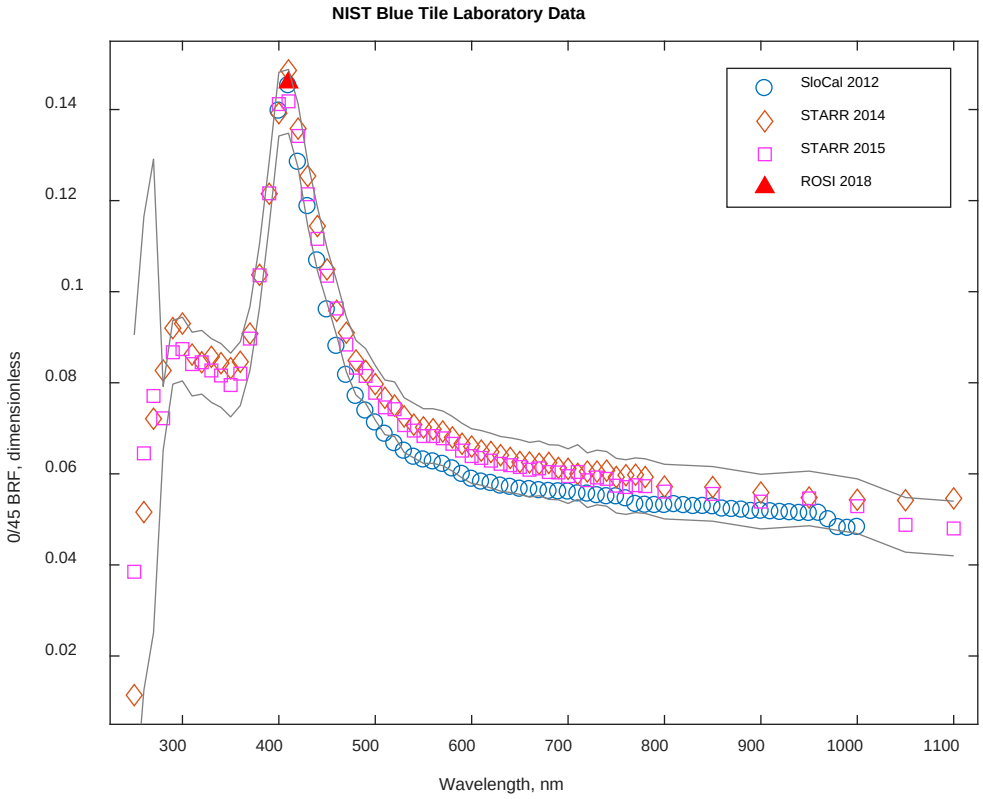

Figure 36. In plane 0/45 BRF data for the NIST blue tile using three different facilities from 2012 to 2018.

The blue tile out-of-plane BRF at 410 nm for a range of incident angles and 45° view angle at relative azimuths of 90° and 135° was determined on ROSI in April 2018. The results are plotted in Figure 37, showing the large departure from Lambertian behavior. The full BRDF, including polarization, for a white sintered PTFE was determined using the Goniometric Optical Scatter Instrument (GOSI) at 532 nm and three other wavelengths [Germer, 2017; Germer and Asmail, 1997]. In 2018, GOSI performed similar measurements at 532 nm for a 50.8 cm diameter, 10% gray Spectralon target. The 45/135 configuration at 532 nm for these two samples is also plotted in Figure 37, but we have scaled the white values by the ratio of the gray and white directional/hemispherical reflectance factors to put them on scale with the gray plaque results. At a relative azimuth of 135°, the white sample is nearly flat with incident angle, decreasing by 6% from 0° to 60° angle of incidence (AOI). The 10% gray increases by 17% from 0° to 60° AOI. The blue tile decreases by 30% from 0° to 60° AOI. Based on these laboratory data, we can develop correction factors for the *Okeanos Explorer* data and compare them to earlier work [Castagna, 2017; English, 2018].

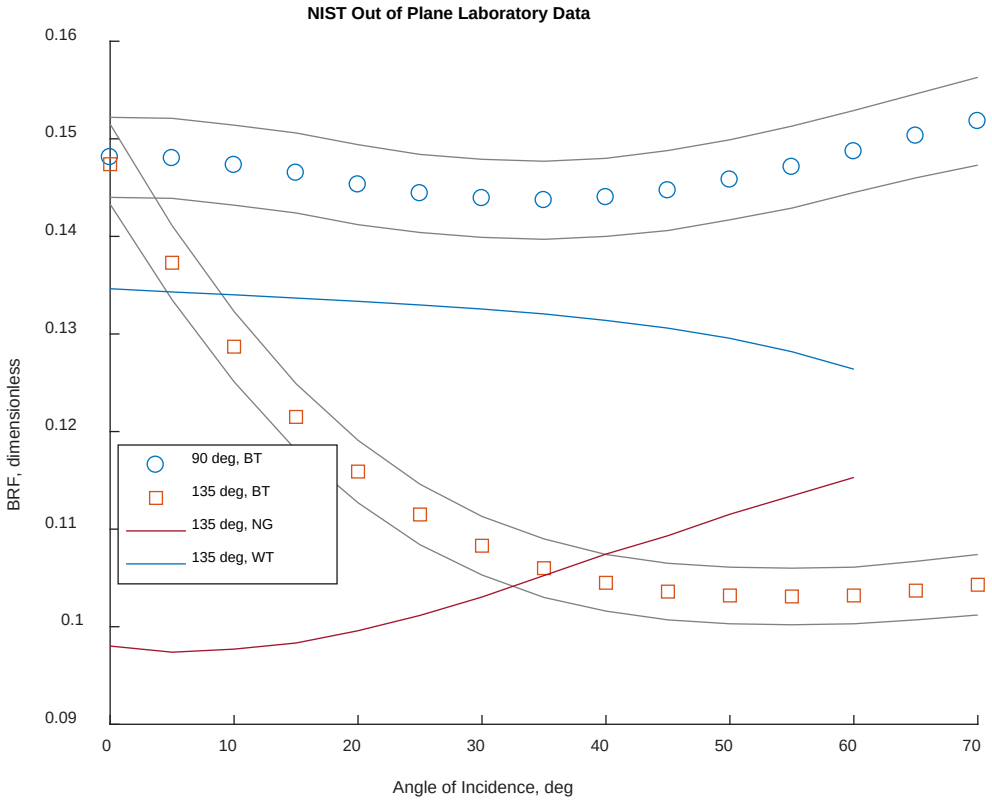

Figure 37. Out of plane BRF data for the blue tile at 410 nm (symbols); at 532 nm, results for a 10% gray Spectralon sample (red line), and the scaled values for a white sintered PTFE sample (blue line) are plotted.

11.7 UMB - Zhongping Lee, Xiaolong Yu, and Zhehai Shang

UMB operated two instruments to measure the R_{rs}, including the RISBA and a Spectral Evolution Spectroradiometer SR-1901. UMB also deployed an IOP package to take measurements of IOP depth profiles. Z_{sd} was recorded at each station in cooperation with Robert Arnone of Stennis/USM.

The main objectives of UMB's participation in the Cal/Val cruise are 1) to acquire measured R_{rs} from the RISBA for instrumental inter-comparison and the validation of $R_{rs}(\lambda)$ products of VIIRS SNPP and VIIRS NOAA-20; 2) to validate VIIRS SNPP and VIIRS NOAA-20 ocean color retrievals with field-measured IOPs and Z_{sd}; 3) to collect above-water measured $R_{rs}(\lambda)$ by handheld spectroradiometer for instrumental inter-comparison; and 4) to investigate the vertical distribution of IOPs in a variety of water types ranging from optically simple oligotrophic waters to optically complex, productive waters.

Instruments and Deployments

UMB primarily deployed four types of intruments on this 2018 VIIRS Cal/Val cruise: the RISBA, Spectral Evolution SR-1901, White Secchi disk with a diameter of 30 cm, and a profiling IOP package consisting of WET Labs ac-s, BB7, and ECO CTD (Figure 38).

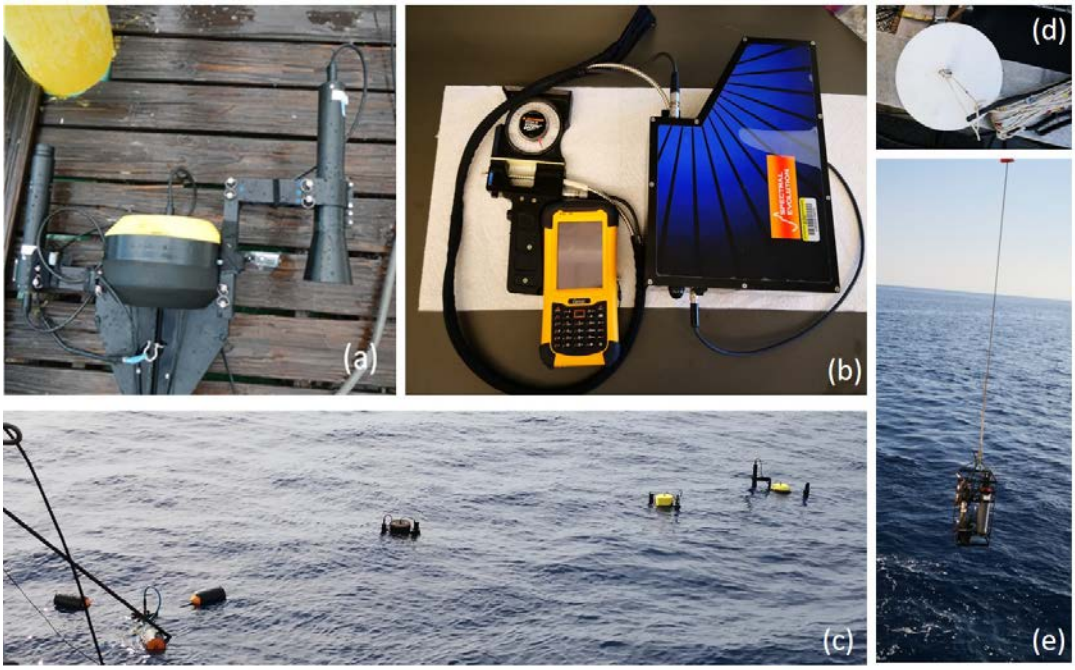

Figure 38. Devices deployed during the VIIRS Cal/Val cruise in May 2018. (a) the RISBA (b) Spectral Evolution SR-1901, (c) deployment of the RISBA (the first one to the right), (d) White Secchi disk with a diameter of 30 cm, (e) deployment of the IOPs package consisting of WET Labs ac-s, BB7, and ECO CTD.

RISBA

UMB measured the L_w directly using the RISBA [Lee et al., 2013]. The RISBA is equipped with one hyperspectral irradiance sensor (HyperOCI, Satlantic Inc.) measuring E_s and one hyperspectral radiance sensor (HyperOCR, Satlantic Inc). As shown in Figure 38a and Figure 38c, the radiance sensor, incorporated with the custom designed cone, can measure water-leaving radiance just above the surface (L_{w0+}) directly by blocking off the surface-reflected skylight. The Satlantic's hyperspectral radiometers are fully digital optical packages. HyperOCR has a FOV of 11.5° in the air (8.5° in water), and measures radiance at ≈3 nm increments from ultraviolet (≈350 nm) to near-infrared (≈800 nm) wavelengths with a wavelength accuracy of ±0.1 nm. Moreover, each spectral band is approximately 10 nm wide. HyperOCI has a cosine response collector and has an accuracy within ±3% for sun angle of 0° to 60° and ±10% for sun angle of 60° to 85°. HyperOCR specifications are adopted from the instrument vendor's calibration certificate.

Both radiometers were calibrated by the manufacturer and further validated at the NOAA/STAR radiometric calibration facilities (see Section 7). During deployment, the instrument package was always kept >20 m away from the ship to minimize ship perturbations. For the measured E_s and L_{w0+} data pairs, only those with an inclination less than 5° were used for further analysis. The E_s was interpolated spectrally to match up with the wavelengths of the L_w data. The instantaneous remote sensing reflectance was first determined as the ratio of instantaneous L_{w0+} to the corresponding E_s.

$$R_{rs}(\lambda,t)=\frac{L_w(0^+,\lambda,t)}{E_s(\lambda,t)} \qquad (6)$$

The first mode of the $R_{rs}(698, t)$ data sequence was located from its probability density function. Further, all those measurements with $R_{rs}(698, t)$ beyond ±15% of the mode were filtered out. This procedure was designed to eliminate those potentially contaminated measurements by sea surface reflection and immersed sensor head at high sea conditions. The remaining $R_{rs}(\lambda, t)$ spectra were used to calculate the

median $R_{rs}(\lambda)$ spectrum at each station. The last step was to correct calculated $R_{rs}(\lambda)$ for self-shading effects introduced by the cone and the floater [Shang et al., 2017].

During the Cal/Val cruise, UMB acquired in situ measured $R_{rs}(\lambda)$ by the RISBA (hereafter denoted as SBA_R_{rs}) at 20 of the 24 scheduled stations. UMB did not take measurements of SBA $R_{rs}(\lambda)$ at stations 4, 9, 16 and 24 because of either rough sea conditions or insufficient time for instrument deployment.

Above-water handheld spectroradiometer

UMB participated in the AWG activities (see Section 8.4). UMB's Spectral Evolution is equipped with a radiance sensor and an irradiance sensor and takes radiometric measurements at a spectral resolution of 4 nm between 350 nm to1000 nm and of 10 nm between 1000 nm and 1900 nm. UMB measured the sky radiance (L_{sky}), L_u and E_s at 20 of 24 stations during the cruise. For each of the radiometric measurement, five to ten consecutive scans were taken, and the averaged data was used for the calculation of R_{rs}. Note that scans were discarded if either of the measurement deviated more than a confidence interval from the median spectrum of the five scans. The confidence intervals for L_u, L_{sky}, and E_s measurements are set to 2 σ, 1.5 σ, and 1 σ, respectively. When measuring L_{sky} and L_u, the radiance sensor was held at between 90° and 135° azimuthal angle to the sun and at a 40° nadir angle to minimize reflected sunlight.

Measured L_u by the Spectral Evolution is the sum of the surface-reflected sky radiance (L_{ref}) and L_w, where L_{ref} can be considered as a fraction (ρ) of the L_{sky}. ρ is equal to the average of Fresnel reflectance (0.023) for a level sea surface and a uniform sky radiance distribution, but in most cases, ρ is significantly larger. The measured $R_{rs}(\lambda)$ by the Spectral Evolution is, therefore, expressed as (omitting wavelength dependence for brevity)

$$R_{rs} = \frac{L_w}{E_s} = \frac{L_u - \rho L_{sky}}{E_s} \quad . \qquad (7)$$

For proper instrumental inter-comparisons, the same protocol was applied to the calculation of $R_{rs}(\lambda)$ from above-water radiometric measurements (Section 8.4), where ρ is determined by given wind speed and solar zenith angle [Mobley, 2015]. The calculated $R_{rs}(\lambda)$ has further corrected for residual surface reflectance by subtracting the average R_{rs} between 750 nm and 850 nm from the whole spectral range. The resultant $R_{rs}(\lambda)$ is hereafter denoted as SEV-Standard.

UMB also employed a semi-analytical (SA) approach to resolve $R_{rs}(\lambda)$ from above-water measurements, where a spectrally dependent scalar offset ($\Delta(\lambda)$) is introduced to correct the residual surface reflectance [Groetsch et al., 2017]. Calculation of $R_{rs}(\lambda)$ by the semi-analytical approach can be expressed as,

$$R_{rs} = \frac{L_u}{E_s} - \rho \frac{L_{sky}}{E_s} - \Delta(\lambda) \qquad (8)$$

where $\Delta(\lambda)$ is determined by spectral optimization. Details regarding this correction approach and the code for data process can be found in [Groetsch et al., 2017]. The resultant $R_{rs}(\lambda)$ by the semi-analytic approach is hereafter denoted as SEV-SA.

UMB submitted measured SEV-Standard $R_{rs}(\lambda)$ data to Ivan Lalovic of OSU, and the instrumental inter-comparison for all handheld spectroradiometers can be found at OSU's section (see Section 11.8). UMB also took measurements of NOAA white plaque and NIST blue tile to test the performance of the above-water radiometers and evaluate the reproducibility of in situ transfers of reflectance scales between reflectance targets. The raw data of UMB measurements were submitted to B. Carol Johnson of NIST, and the evaluation of different above-water radiometers and reflectance targets can be found at NIST's section (see Section 11.6).

IOP package

The UMB IOPs package (Figure 38e) is integrated with one ac-s (WetLabs Inc.), one backscattering meter (BB7FL2, WetLabs Inc.), and an ECO CTD (SeaBird Inc.). The IOPs package was deployed at 20 of the 24 scheduled stations from the surface to a maximum depth of 100 m below the surface.
The ac-s measures hyperspectral non-water attenuation coefficient (c_{nw}) and absorption coefficient (a_{nw}) at 77 wavelengths from 402 nm to 732 nm. Pure water calibration was carried out using Milli-Q water on board before the cruise on 8 May 2018 and post-cruise on 17 May 2018. The BB7FL2 measures b_b at seven wavelengths (412 nm, 440 nm, 488 nm, 532 nm, 595 nm, 695 nm, and 715 nm) and the fluorescence of chlorophyll and CDOM. The BB7FL2 also provides measurements of b_{bp} as the difference between b_b and pure water backscattering (b_{bw}). The ECO CTD measures the water conductivity, temperature, and salinity simultaneously with the ac-s and BB7FL2.
To acquire the measured IOPs and CTD, raw data achieved in the DH4 was first extracted to the individual data file of each instrument using the WET Lab application 'wap425.exe'. These extracted ac-s data were then calibrated by subtracting the pure water calibration data and corrected for salinity and temperature effects using the WET Lab software 'WetView'. For ac-s measured a_{nw}, scattering effects were further accounted for with a baseline correction by subtracting the a_{nw} at 700 nm from the whole spectral range.

For the validation of satellite ocean color products, IOPs of the surface water layer were extracted from the depth profile measurements. Precisely, the median and σ of IOPs at 440 nm were first calculated from all measurements within the water depth range between 1 m and 5 m. The surface IOPs were then obtained by averaging all measured IOPs that within the range of median IOPs value +/- 1 σ. The same approach was applied to the calculation of surface CTD and the fluorescence of CDOM and chlorophyll.

Note that NRL continuously measured the IOPs of flow-through waters pumped from approximate 3 m beneath the surface during the Cal/Val cruise. The inter-comparison of IOPs measured by UMB and NRL will be reported elsewhere after UMB receives the data from NRL. USF collected water samples to determine the a_p and a_{ph} using the quantitative filter pad technique (QFT) [Tassan and Ferrari, 1995] (see Section 11.5). The comparison of non-water absorption coefficients measured by QFT and WET Lab ac-s at surface layer will also be reported elsewhere after the USF data are available.

Preliminary Results

Validation of Satellite R_{rs} products

In total, 13 matchups were retrieved from VIIRS SNPP images that match SBA measurements in location and time, and 12 matchups were obtained from VIIRS NOAA-20 images. The level 2 products (science quality) of both VIIRS SNPP and VIIRS NOAA-20 were downloaded from the NOAA OC science team. The satellite matchups were retrieved as the mean value of a 3×3 pixels box that contains at least 50% valid pixels in the box. Note that pixels flagged as "High Solar Zenith Angle, High Sensor Zenith Angle, and Sun Glint" are considered as invalid retrievals.

The level 2 products of VIIRS SNPP and VIIRS NOAA-20 are the $nL_w(\lambda)$, and therefore need be converted to $R_{rs}(\lambda)$ by dividing by F_0. Both F_0 and SBA_R_{rs} were spectrally weighted to VIIRS SNPP and VIIRS NOAA-20 bands by accounting for their respective relative spectral response functions. Figure 39 presents the validation results of VIIRS SNPP and VIIRS NOAA-20 $R_{rs}(\lambda)$ products at 410 nm, 443 nm, 486 nm and 551 nm. The QA score, a system to evaluate the quality of R_{rs} spectrum [Wei et al., 2016], of satellite-derived $R_{rs}(\lambda)$ is also presented in Figure 39.

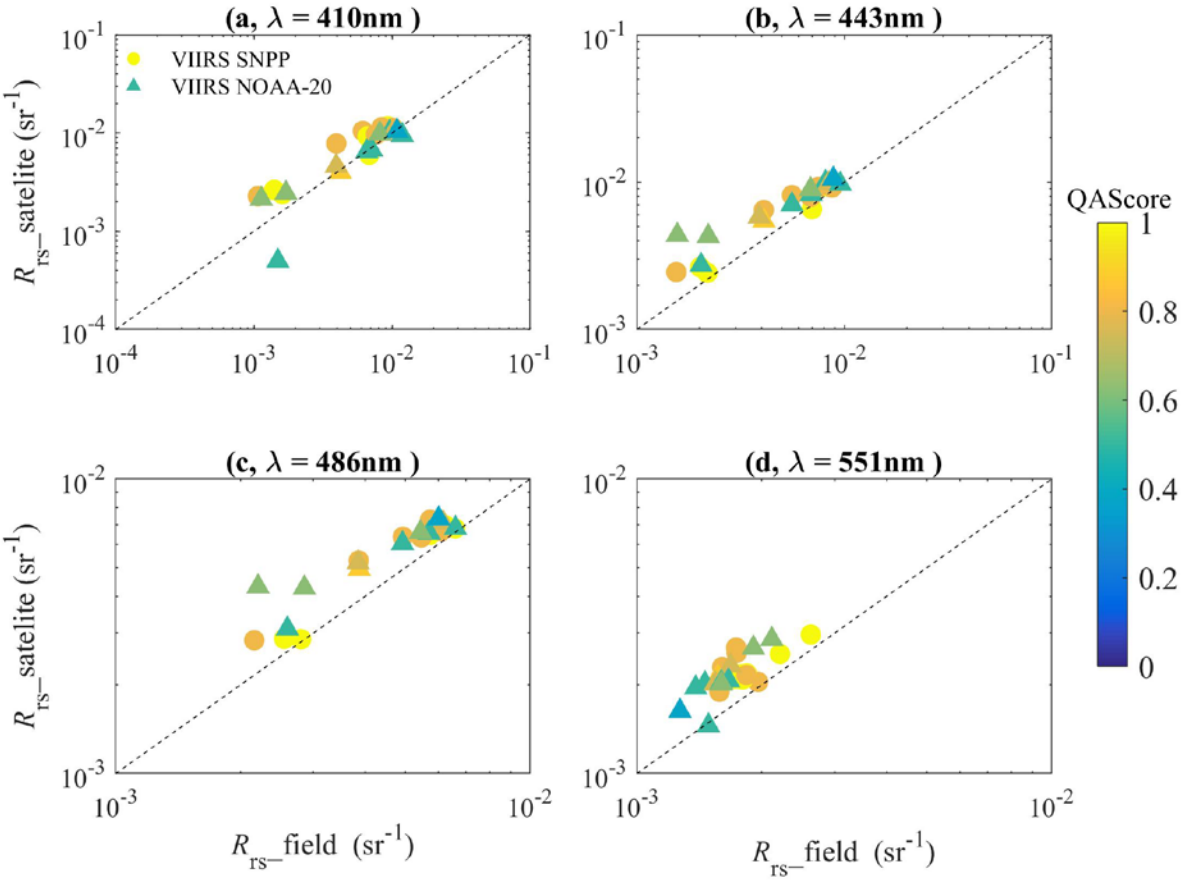

Figure 39. Validation of $R_{rs}(\lambda)$ products of VIIRS SNPP (circles) and VIIRS NOAA-20 (triangles) by field measured SBA_R_{rs} at 410 nm, 443 nm, 486 nm and 551 nm. The scatter color marks the QA score (dimensionless) of each satellite $R_{rs}(\lambda)$ matchup.

As shown in Figure 39, $R_{rs}(\lambda)$ match-ups obtained from VIIRS SNPP and VIIRS NOAA-20 are overall comparable at the four selected wavelengths. However $R_{rs}(\lambda)$ match-ups from VIIRS SNPP agree slightly better than match-ups from VIIRS NOAA-20 when compared with field-measured $R_{rs}(\lambda)$. Statistical results supporting Figure 39 are tabulated in Table 12 and discussed in the next paragraph. Validation result of R_{rs} at the M5 band of VIIRS SNPP and VIIRS NOAA-20 (centered at 671 nm and 667 nm, respectively) is not presented here because of the relatively more considerable uncertainties of the satellite-derived R_{rs} at this band. It is worthy to note that despite the comparable performances of VIIRS SNPP and VIIRS NOAA-20 $R_{rs}(\lambda)$ products, QA scores of the NOAA-20 $R_{rs}(\lambda)$ matchups are significantly lower than the QA scores of VIIRS SNPP $R_{rs}(\lambda)$ matchups. NOAA STAR OCView provides the mapping products of QA score for VIIRS SNPP and NOAA-20 from where we can observe that the poor QA score quality of NOAA-20 $R_{rs}(\lambda)$ products is likely a systematic issue with the satellite data. Addressing the quality issue of the NOAA-20 $R_{rs}(\lambda)$ product is beyond the scope of this report, but comparisons between VIIRS SNPP and NOAA-20 $R_{rs}(\lambda)$ matchups show that the poor QA score of NOAA-20 R_{rs} spectra could probably be related to uncertainties of NOAA-20 R_{rs} at the M1 band centered at 411 nm (figure not shown here).

Statistical parameters between SBA_R_{rs} and satellite $R_{rs}(\lambda)$ matchups are analyzed and tabulated in Table 12. Note that rMAD in Table 12 refers to the relative mean absolute difference, and the slope, intercept, and the correlation coefficient (R^2) were computed using the Type-II regression.

Table 12. Statistics of the validation results for NOAA-VIIRS and NOAA-20 $R_{rs}(\lambda)$ matchups.

	412 nm		443 nm	
	VIIRS SNPP	NOAA_20	VIIRS SNPP	NOAA_20
Slope	1.166	0.939	1.073	0.930
Intercept	0.001	0.000	0.001	0.002
R^2	0.868	0.925	0.914	0.944
rMAD (%)	48.4	23.2	24.6	43.8
	486 nm		551 nm	
	VIIRS SNPP	NOAA_20	VIIRS SNPP	NOAA_20
Slope	1.097	0.900	1.095	1.706
Intercept	0.000	0.002	0.000	-0.001
R^2	0.929	0.909	0.443	0.799
rMAD (%)	16.8	29.1	24.0	30.7

The statistical results show that VIIRS SNPP $R_{rs}(\lambda)$ product has overall better performance compared with NOAA-20 $R_{rs}(\lambda)$ product except for the rMAD for R_{rs} at 412 nm. Field measured $R_{rs}(\lambda)$ by other in-water instruments (floaters and profiles) were also used to validate the two satellite $R_{rs}(\lambda)$ products. The instrumental inter-comparison and validation of VIIRS SNPP and VIIRS NOAA-20 $R_{rs}(\lambda)$ products were summarized by Michael Ondrusek of NOAA (Section 9).

Validation of derived IOPs and Z_{sd} for satellite R_{rs} match-ups

1. Validation of derived a and b_b

Figure 40 presents the measured total non-water absorption coefficients and total backscattering coefficients by WET Labs ac-s and BB7FL2. As shown in Figure 40b, measured b_b at 412 nm and 488 nm are questionable and significantly underestimated, which is probably due to the calibration issue. However, b_b at 412 nm and 488 nm can be recovered by fitting b_b at the other five wavelengths to a power-law function. The measured a_{nw} in Figure 40a show that the water is relatively productive at the three stations close to the Mobile Bay (Stations 6, 7 and 8) with higher a_{nw}, while other stations water are optically simple.

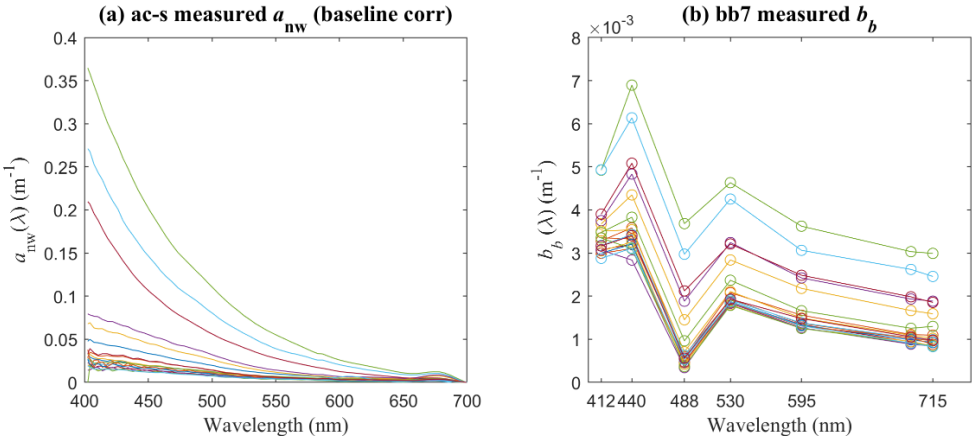

Figure 40. Surface IOPs measured during the Cal/Val cruise. (a) a_{nw} measured by WET Lab ac-s. (b) b_b measured by WET Labs BB7FL2.

UMB employed the QAA model to derive *a* and b_b from $R_{rs}(\lambda)$ [Lee et al., 2002]. The latest version of QAA (v6) is available at http://www.ioccg.org/groups/Software_OCA/QAA_v6_2014209.pdf.

Figure 41 presents the comparison between field-measured a and derived a from SBA_R_{rs} and NOAA-VIIRS and NOAA-20 $R_{rs}(\lambda)$ matchups. Note that ac-s measures only a_{nw}. For a proper comparison, pure water absorption [Lee et al., 2015a] was added to measured a_{nw} to obtain an equivalent to measured a_t. Validation of derived a is presented at four center wavelengths of NOAA-20 (i.e., 411 nm, 445 nm, 489 nm and 556nm (see Figure 41). Note that retrievals from SBA_R_{rs} and VIIRS SNPP $R_{rs}(\lambda)$ are spectrally interpolated to match up with NOAA-20 center bands.

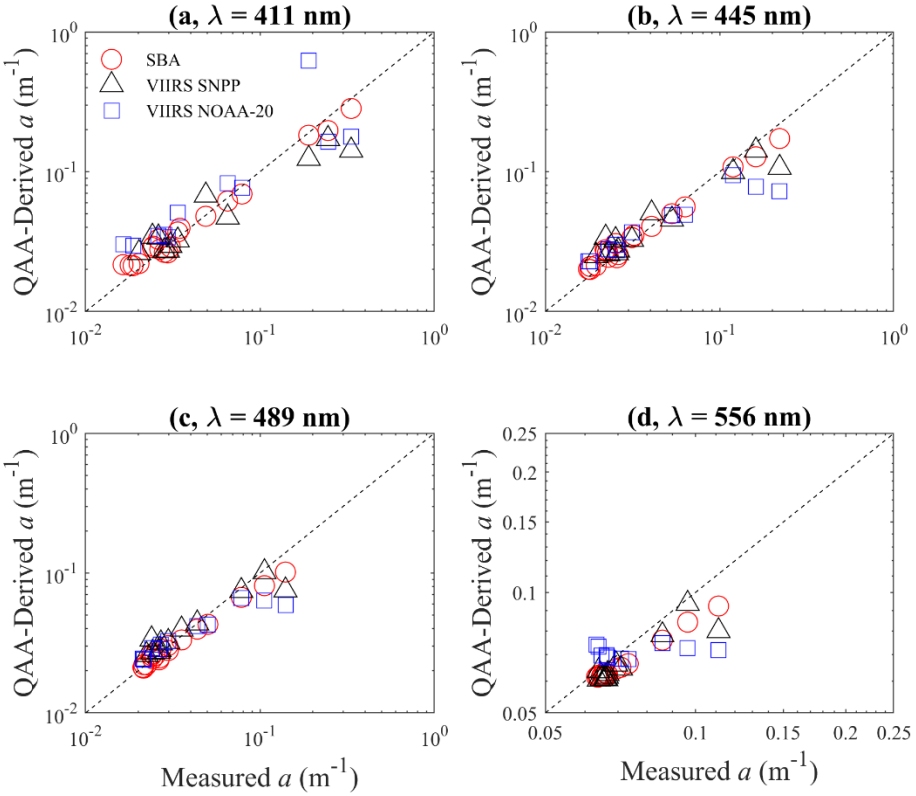

Figure 41. Validation of derived a from SBA-measured $R_{rs}(\lambda)$ and $R_{rs}(\lambda)$ of VIIRS SNPP and VIIRS NOAA-20 matchups.

As shown in Figure 41, a_t derived from SBA_R_{rs} are consistent with ac-s measurements at all four wavelengths. Derived a from VIIRS SNPP and NOAA-20 $R_{rs}(\lambda)$ matchups are overall in good agreement with field measured a for optically simple waters but are underestimated for productive waters, especially for NOAA-20 R_{rs}. Retrieved a from satellite $R_{rs}(\lambda)$ have more substantial uncertainties compared with SBA_ R_{rs}, which mainly because of the uncertainties in satellite $R_{rs}(\lambda)$ products introduced by the atmospheric correction (Figure 39). Note that underestimations of derived a are also observed for SBA retrievals for the productive waters but are significantly smaller.

Considering estimated b_b at 412 nm and 488 nm from power-law fitting will inevitably introduce additional uncertainties, Figure 42 presents only the validation results of derived b_b at two BB7FL2 channels at 440 nm and 530 nm. Derived b_b from SBA_R_{rs} and $R_{rs}(\lambda)$ matchups of VIIRS SNPP and NOAA-20 were interpolated to 440 nm and 530 nm for proper comparison. Validations of derived a and b_b at longer wavelengths are not presented in this report due to the noticeable uncertainties in the satellite $R_{rs}(\lambda)$ products.

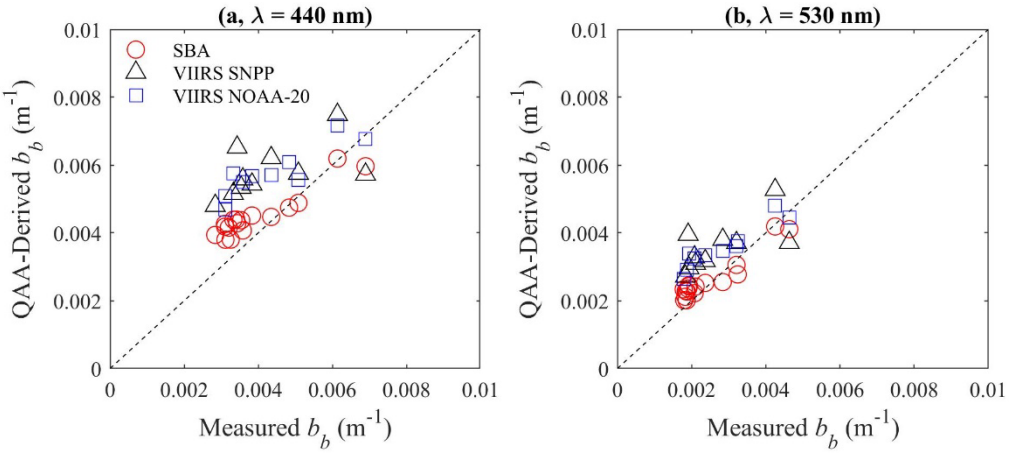

Figure 42. Validation of derived b_b from SBA_R_{rs} and $R_{rs}(\lambda)$ matchups of VIIRS SNPP and VIIRS NOAA-20 at two BB7FL2 channels (440 nm and 530 nm).

Similar to the validation results of derived *a*, derived b_b from SBA_R_{rs} overall matches well with field measured b_b at both 440 nm and 530 nm, despite slight overestimations for optically simple waters. However, derived b_b from VIIRS SNPP and NOAA-20 $R_{rs}(\lambda)$ match-ups are notably overestimated, which could be explained by the overestimation of the satellite-derived R_{rs} (Figure 39). As shown in Figure 42, derived b_b from SBA_R_{rs} has less scatter at 530 nm than retrievals at 440 nm. Therefore, it is reasonable to assume that the measured b_b(440) is potentially underestimated considering the significant underestimation of b_b at 412 and 488 nm (Figure 40b). To conclude, the overall good retrieval of both *a* and b_b from SBA_R_{rs} confirms the high quality of *in-situ* measured $R_{rs}(\lambda)$ and IOPs, as well as the robustness of the QAA model. Also, note that the uncertainties in satellite-derived R_{rs} will be propagated to the retrieved IOPs through the inverse model.

2. Validation of derived Z_{sd}

Z_{sd} was measured at 20 of the 24 scheduled stations, along with the deployment of RISBA. In this report, UMB adopted a semi-analytical model to remotely retrieve Z_{sd} from R_{rs} [Lee et al., 2016; Lee et al., 2015b]. The first step of Lee's model is to determine the diffuse attenuation coefficient (K_d) from R_{rs}-derived IOPs using the QAA_v6 model [Lee et al., 2005b; Lee et al., 2005a]. Z_{sd} can be then estimated from the minimum derived K_d at 443 nm, 486 nm, 530 nm, 551 nm and 671 nm [Lee et al., 2016; Lee et al., 2015b]. Note that K_d(530) is empirically determined from derived K_d at 486 nm and 551 nm for VIIRS SNPP and NOAA-20 $R_{rs}(\lambda)$ matchups [Lee et al., 2016]. Figure 43 compares the derived Z_{sd} from SBA_$R_{rs,}$ and $R_{rs}(\lambda)$ matchups from VIIRS SNPP and NOAA-20 with field measured Z_{sd}.

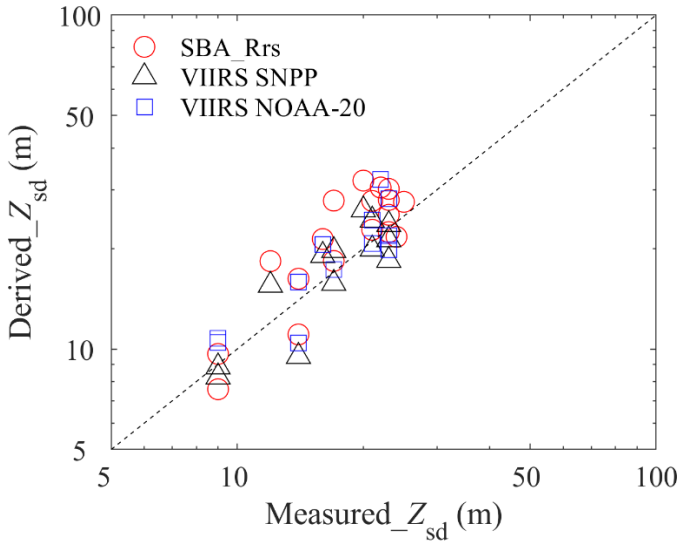

Figure 43. Validation of derived Z_{sd} from SBA_R_{rs} and $R_{rs}(\lambda)$ matchups of VIIRS SNPP and NOAA-20.

Overall, satisfying retrievals of Z_{sd} are obtained from SBA_R_{rs} and $R_{rs}(\lambda)$ of the satellite match-ups. The rMAD of derived Z_{sd} from SBA_R_{rs}, VIIRS SNPP $R_{rs}(\lambda)$ and VIIRS NOAA-20 $R_{rs}(\lambda)$ are 24.5% (n = 20), 15.1% (n = 13), and 17.5% (n = 12), respectively. For rigorous evaluations of the derived Z_{sd} from all three $R_{rs}(\lambda)$ data, rMAD was recalculated exclusively for stations with matchups from both NOAA-VIIRS and NOAA-20 (n = 9). The recalculated rMAD are 15.4%, 13.0% and 14.2%, respectively. Despite the uncertainties in satellite-derived $R_{rs}(\lambda)$ (Figure 39), the comparable estimations of Z_{sd} from SBA_R_{rs} and $R_{rs}(\lambda)$ of VIIRS SNPP and NOAA-20 could be mainly due to the consistent retrievals of a for optically simple waters (Figure 41). Fundamentally, Z_{sd}, approximately the inverse of minimum K_d in the transparent window [Lee et al., 2016; Lee et al., 2015b], is a function of IOPs. Note that b_b in the optically simple waters is about an order of magnitude lower than a (Figure 41 and Figure 42). K_d is therefore, like derived Z_{sd},, primarily determined by a.

As shown in Figure 43, Z_{sd} is slightly overestimated at some of the stations with high water transparency, which could be due to the uncertainties in field-measured Z_{sd}. Field measured Z_{sd} is expected to show some variability, especially for measurements taken under rough sea conditions with strong winds and currents. The quality of field measured Z_{sd} can be later evaluated from field measured K_d because Z_{sd} is roughly the inverse of minimum K_d in the transparent window and field measured K_d can be considered as error-free.

Depth profiles of IOPs and Fluorescence of CDOM and CHL

The vertical variations of temperature, salinity, IOPs, and fluorescence of CDOM and Chl-*a* of the sampling stations can be investigated from the depth profile measurements. Here we select two stations to present the vertical distributions of these parameters in relatively productive waters (Station 6, Figure 44) and optically simple waters (Station 21, Figure 45). Station 6 is close to the Mobile Bay with a water depth of 75 m, while Station 21 is located in the offshore of east Florida coast with a water depth of 754 m. Locations of these two stations can be found in Figure 2 and Table 3.

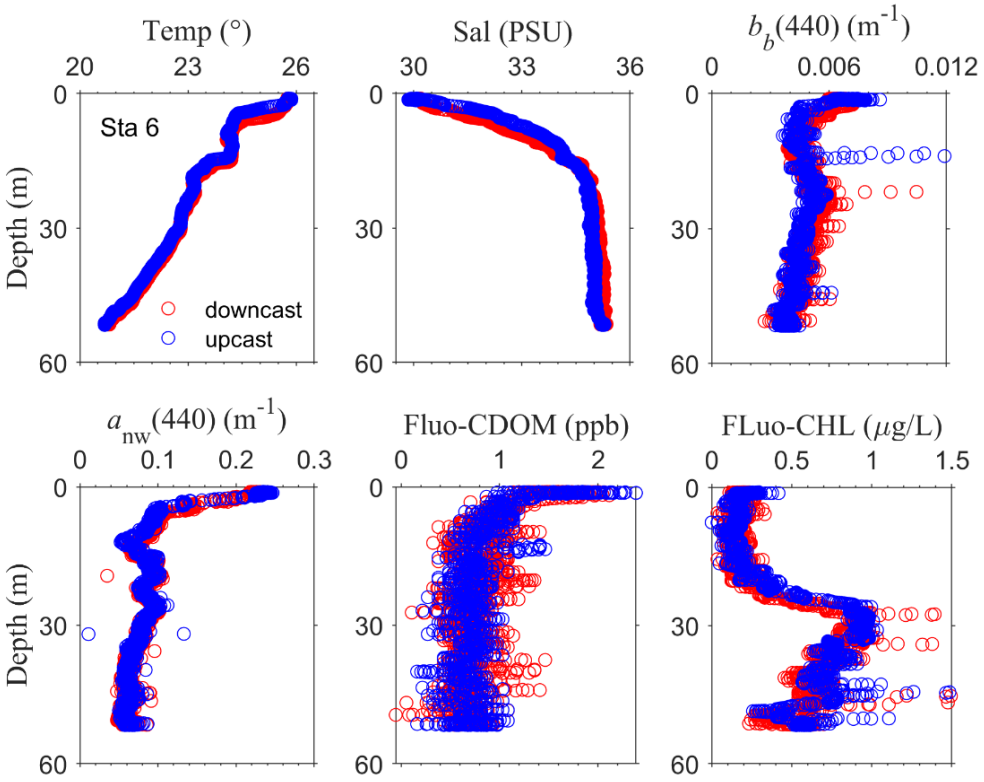

Figure 44. Depth profiles of water temperature (Temp, °C), salinity (Sal, g kg^{-1}), b_b (440), a_{nw} (440), CDOM and Chl-*a* fluorescence (Fluo-CDOM, ng kg^{-1}, and FLuo-CHL, mg m^{-3}, respectively) at Station 6, an example of relatively productive water.

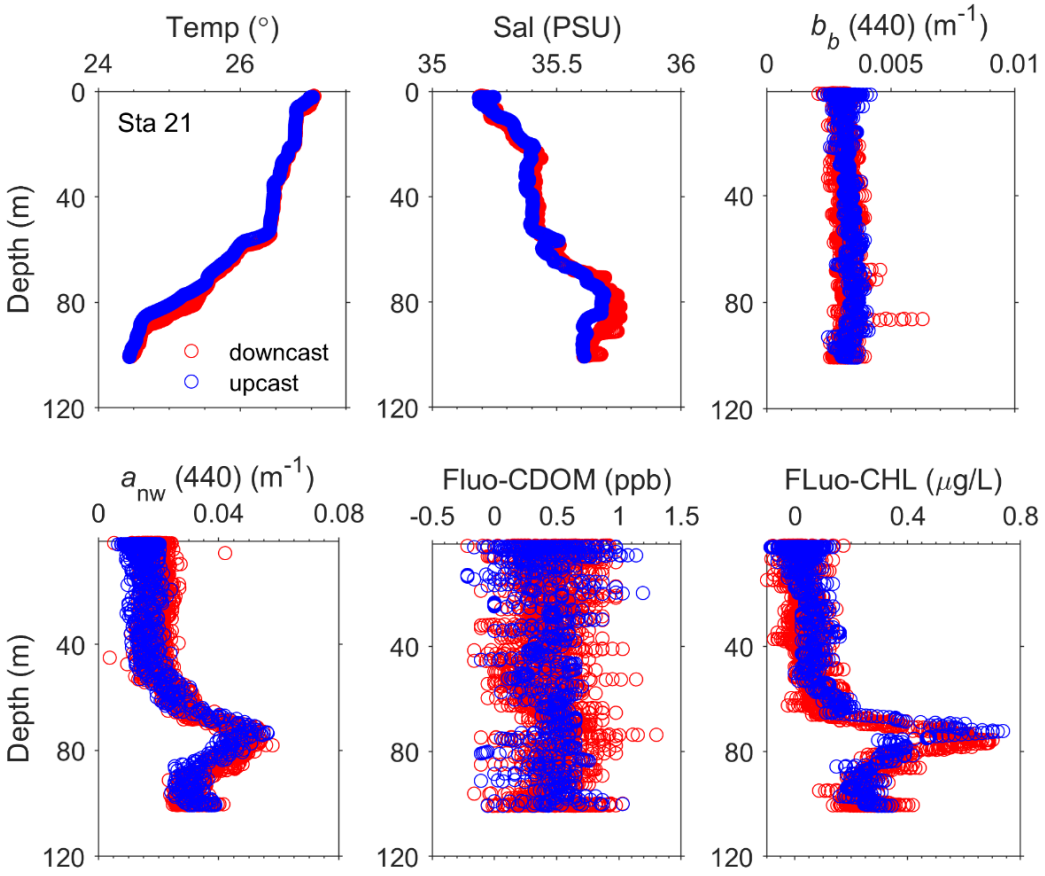

Figure 45. Same as Figure 7, but for Station 21, an example of optically simple water.

As shown in Figure 44 and Figure 45, two different distribution patterns are observed for productive waters compared with optically simple waters. In productive waters (Figure 44), both a_{nw} and b_b decrease rapidly within the first 10 m from the surface and show much-limited variabilities in deeper depths. To the contrary, phytoplankton (as indicated by FLuo-CHL) is stable in the surface layer but starts to increase at 20 m depth to the Chl-*a* maximum layer at an approximate 30 m depth. Vertical distributions of a_{nw} and Chl-*a* fluorescence in Figure 44 suggest that the non-algal particles dominate the total absorption in the productive waters, as no synchronous variation can be found between these two parameters. For the optically simple waters (Figure 45), the water column is generally homogenous within the first 60 m with negligible variations of non-algal particles, CDOM, and Chl-*a*. The vertical variation of a_{nw} covaried with Chl-*a* fluorescence, indicating that phytoplankton is the primary water component that determines these IOPs. Also, the Chl-*a* maximum zone was much deeper at Station 21 compared with Station 6, where the maximum Chl-*a* exhibits at about 80 m below the surface. The two examples show that depth profiles of IOPs and CDOM and Chl-*a* fluorescence allow confident interpretations of the dominant optical compositions of water in different depths.

The CDOM and Chl-*a* fluorescence measured by the BB7FL2 have not been well calibrated yet. However, USF collected water samples to measure the CDOM absorption and Chl-*a* concentrations for surface layer waters (see Section 11.5). UMB will later use USF data to evaluate the quality of the fluorescence data and develop empirical relationships between the fluorescence data and the concentrations of CDOM and Chl-*a*.

Evaluation of above-water measured R_{rs} by the Spectral Evolution

During the Cal/Val cruise, most above-water measurements were made under cloudy conditions (cloud cover > 40%) with wind-roughened sea surface. The inhomogeneous sky radiance distribution and changing illumination conditions will inevitably introduce additional uncertainties to the measured $R_{rs}(\lambda)$ because it is not possible for handheld radiometers to concurrently measure L_u, L_{sky}, and E_s. The roughened sea surface, on the other hand, could introduce more residual surface-reflected sun and sky radiance (such as sun glint and sky reflections) that were not represented by measured L_{sky}. Furthermore, the UMB Spectral Evolution has a typical integration time of 2 s to 3 s for each scan, which is too long to resolve short exposure to sun glint and rule out its contamination even for an optimum viewing geometry. Therefore, a rigorous correction approach for above-water measurement is essential to acquire high-quality $R_{rs}(\lambda)$ data. UMB-measured SEV-R_{rs} were corrected for residual surface reflectance by two approaches, including the standard protocol and a semi-analytical approach. The SBA_R_{rs}, which is resistant to surface reflectance, is adopted to evaluate the performance of the two correction approaches. Figure 46 presents comparisons of measured R_{rs} spectra by the RISBA and the Spectral Evolution with two correction schemes.

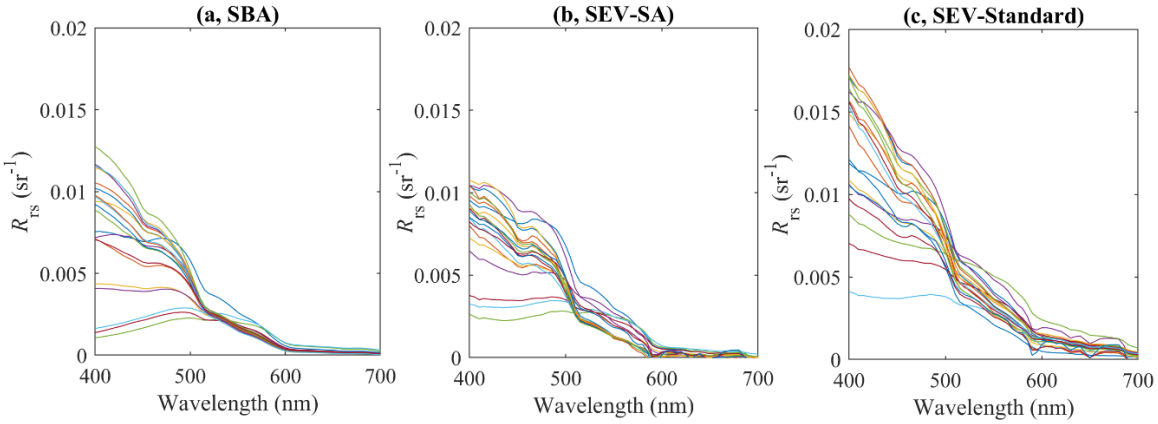

Figure 46. The spectra of field-measured $R_{rs}(\lambda)$ by the RISBA (a) and the Spectral Evolution with residual correction by the semi-analytical approach (b) and the standard protocol (c).

Figure 46 shows that SEV-SA R_{rs} is very consistent with the SBA_R_{rs} regarding both the spectral shape and magnitude of R_{rs}, but the SEV-Standard R_{rs} is significantly overestimated, especially at short wavelengths. It is evident that the quality of SEV-Standard R_{rs} is questionable. For instance, for the three stations close to the Mobile Bay (Stations 6, 7, and 8 in Figure 2), CDOM fluorescence and non-algal particles are present and absorb light strongly in the blue band (*e.g.*, Station 6, Figure 44), but SEV-Standard R_{rs} of these stations still present higher reflectance at 400 nm than 550 nm. The scatter plots between SBA_R_{rs} and two SEV_R_{rs} are also presented in Figure 47 for R_{rs} at 410 nm, 440 nm, 490 nm and 550 nm.

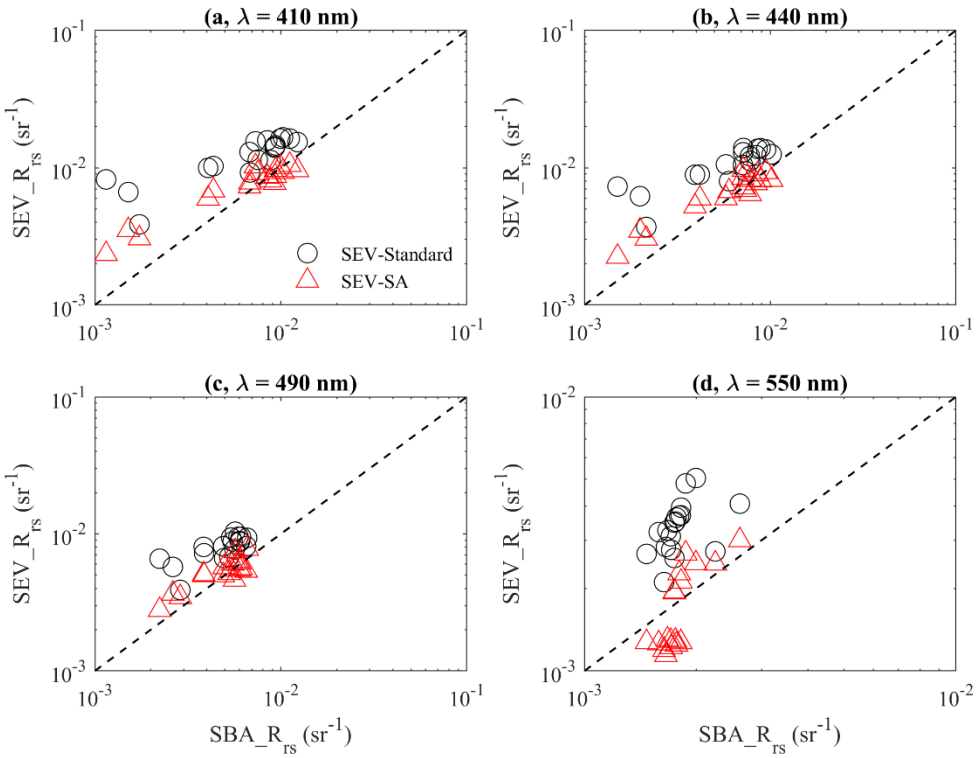

Figure 47. Comparisons of SBA-measured R_{rs} and two SEV-measured R_{rs} (SEV-SA and SEV-Standard) at 410 nm, 440 nm, 490 nm and 550 nm.

As shown in Figure 47, overestimations of SEV-Standard R_{rs} are observed at all the four selected wavelengths, while SEV-SA R_{rs} is overall comparable with SBA_R_{rs}. Note that the SBA R_{rs} was usually measured at least half an hour later than the SEV R_{rs}. During this amount of time, depending on the currents and weather conditions at a given station, the ship could drift kilometers and the sky radiance distribution could be variable during cloudy days. Therefore, the performance of SEV-SA is quite encouraging.

The main difference between the standard protocol and Groetsch's SA approach mentioned earlier is that the latter one assumes a spectral-dependent resolved offset. The standard protocol subtracts the mean R_{rs} between 750 nm and 850 nm, which can be considered as a constant scalar offset correction. The other uncertainties associated to the SEV-Standard R_{rs} is that the ρ, determined for given wind speed and solar zenith angle [Mobley, 2015], is spectrally independent, while many practices have confirmed that ρ should be treated as a function with strong wavelength dependency [Groetsch et al., 2017; Lee et al., 2010; Sokoletsky and Shen, 2014]. The differences in the spectral shapes of SBA_ R_{rs} and SEV-Standard R_{rs} in Figure 46 demonstrate that residual surface reflectance is much stronger in short wavelengths. Nevertheless, evaluation of SEV-Standard R_{rs} and SEV-SA R_{rs} suggests that a spectrally dependent ρ or a spectrally resolved offset is required to correct above-water measured R_{rs}, especially for inhomogeneous sky distribution and roughened sea condition. On the other hand, an adequate correction approach, *e.g.*, the Groetsch's SA approach, could probably relax measurement geometry requirements.

11.8 OSU, Ivan Lalovic and Nicholas Tufillaro

Instruments: Spectral Evolution (PSR-1100) and Satlantic (HyperPro)

OSU operated a Satlantic Free Falling Optical Profiler (Figure 48) for in water radiance measurements, as well as handheld above-water radiance and reflectivity measurements with a Spectral Evolution Field

Spectrometer (Figure 49) PSR-1100-F. The Optical Profiler is also equipped with a Wetlabs ECO Puck, measuring scattering at 470 nm and 700 nm and chlorophyll fluorescence at 470 nm and 695 nm.

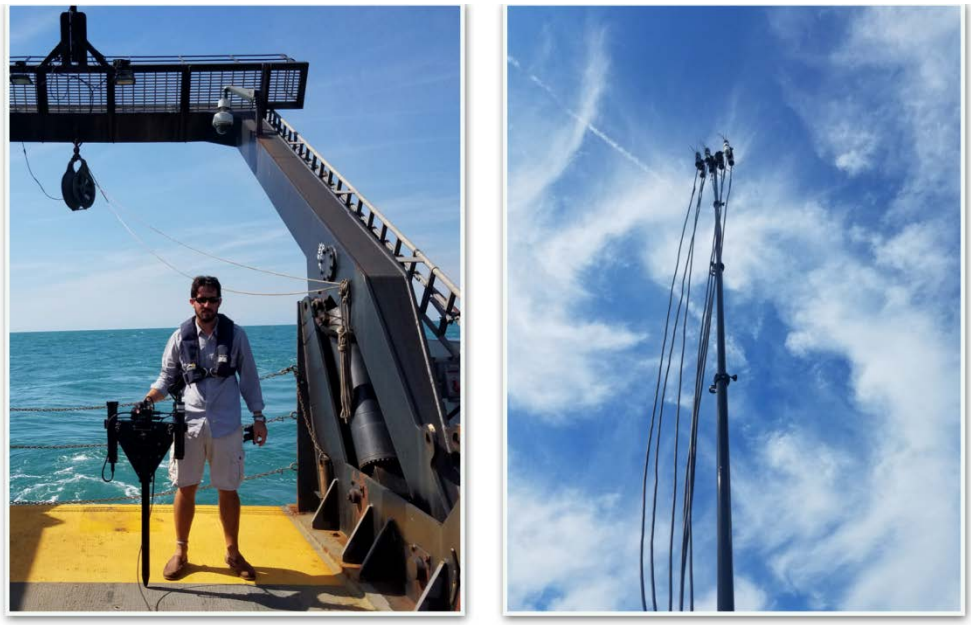

Figure 48. (Left) OSU HyperPro operated by Ivan Lalovic; (Right) Downwelling radiometers mounted on an extendable 'Grappa' pole on the NOAA Ship *Okeanos Explorer*

Figure 49. (Left) Location on Bow of *Okeanos Explorer* where all AWG activities were conducted; (Right) OSU Spectral Evolution PSR-1100 radiometer operated by Dr. Nicholas Tufillaro

Protocols: Satlantic, HyperPro

The Optical Profiler II (aka HyperPro) deployments were done off the stern of the NOAA Ship *Okeanos Explorer* under the direction of Michael Ondrusek of NOAA. The deployment and processing protocols use 'yoyo' casts and Satlantic ProSoft processing. Processing follows protocols by Michael Ondrusek (protocol document via personal communication) and also OSU online Appendix A of the 2018 OSU report: "HyperPro Deployment Protocols" (http://meris.coas.oregonstate.edu/tmp/OSU_NOAA_CRUISE_REPORT_2018_05/OSU_2_REPORT_APPENDIX_A_HyperProDeploymentProtocols_PDF.pdf).

Protocols: Spectral Evolution, PSR-1100-F

The Spectral Evolution spectrometer was first used during the 2015 NOAA VIIRS Cal/Val cruise and is held off the side of the ship in a similar manner as the ASD and other manually-operated above-water radiometers. The measurement protocols are detailed in the OSU 2018 VIIRS Cal/Val cruise report in OSU online Appendix B: "Methods for Measuring Above-water R_{rs}" (http://meris.coas.oregonstate.edu/tmp/OSU_NOAA_CRUISE_REPORT_2018_05/OSU_3_REPORT_APPENDIX_B_MethodsformeasuringRrs_2016-02-16_90%20deg8FOV_WORD.doc).

A sequence of three measurements are made: (1) a standard reflectance plaque, (2) the water reflectance, and (3) the sky radiance. From these, R_{rs} is estimate with the formula:

$$R_{rs} = (S_{W+S} - S_{sky}\,\rho(\theta))/(\,\pi S_p/\mathrm{refl}) \qquad (9)$$

where S_{W+S} is the measured signal from the water and includes both L_w and reflected skylight. S_{sky} is the measured signal from the sky, S_p is the average measured signal from the white Spectralon Plaque, and 'refl' is the reflectivity of the plaque (approximately 99%; actual measured spectral values used in the calculation). 'Pi' (π) converts the reflected radiance values to irradiance for this nearly Lambertian diffuser. The measured sky radiance is multiplied by $\rho(\theta)$ which is the proportionality factor that relates the radiance measured when the detector views the sky to the reflected sky radiance measured when the detector views the sea surface. The value of $\rho(\theta)$ is dependent on wind speed and direction, detector FOV, and sky radiance distribution. Only in the case of a level sea surface and a uniform sky radiance distribution does $\rho(\theta)$ equal the average of the Fresnel reflectance over the detector FOV. For our measurement angles under nominal sky and wind conditions, we calculate $\rho(\theta)$ using data from Mobley [Mobley, 2015]. Note that these values are always significantly higher than the value 0.023 used for conditions of complete overcast.

As part of our NOAA supported work, we continued the development of an automated software program to perform quality control and the computation of $R_{rs}(\lambda)$ for the Spectral Evolution radiance data. Figure 50 and Figure 51 show the graph outputs from the software. The stand-alone program automatically removes outliers after setting threshold variance levels for rejection (typically 2 σ), and computes R_{rs} using the remaining data. We recently also implemented computation of maximum and minimum R_{rs} spectra calculated from the ensemble of plaque, sky and water measurements. An optical 'red end' constant base-line subtraction is included as an initial solution for removing residual surface reflectance (glint) contributions and is computed independently for the maximum, minimum and mean R_{rs}.

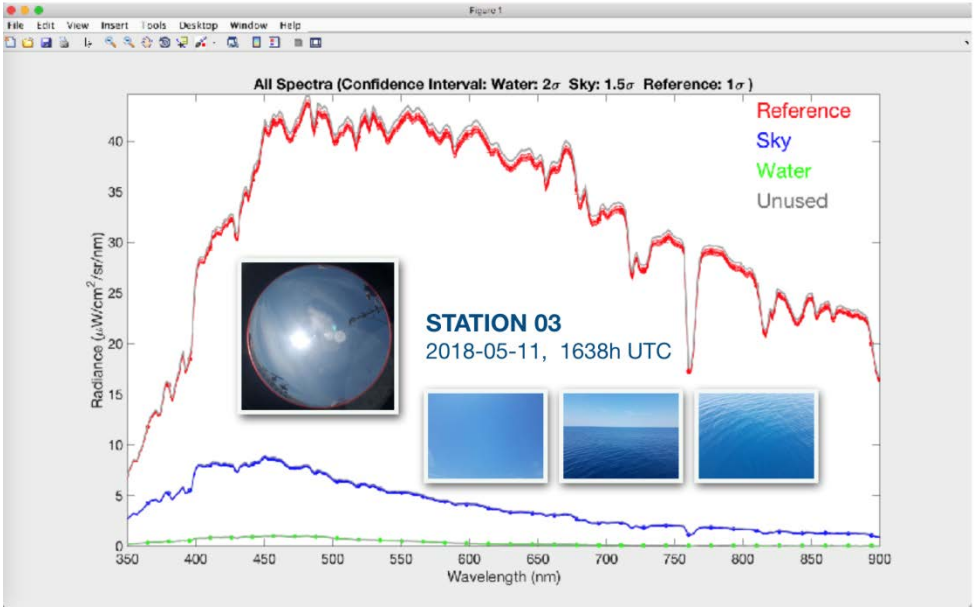

Figure 50. Plot outputs of automated processing software to compute $R_{rs}(\lambda)$ from Spectral Evolution above water measurements. The 'red' reference plot is the 99% reflectance plaque, the 'blue' sky is the downwelling sky radiance, and 'green' spectra is the water radiance. The 'gray' spectra are data that fall outside of a 2 σ, 1.5 σ, and 1 σ variance windows for water, sky and reference respectively and are not used in calculation of R_{rs}.

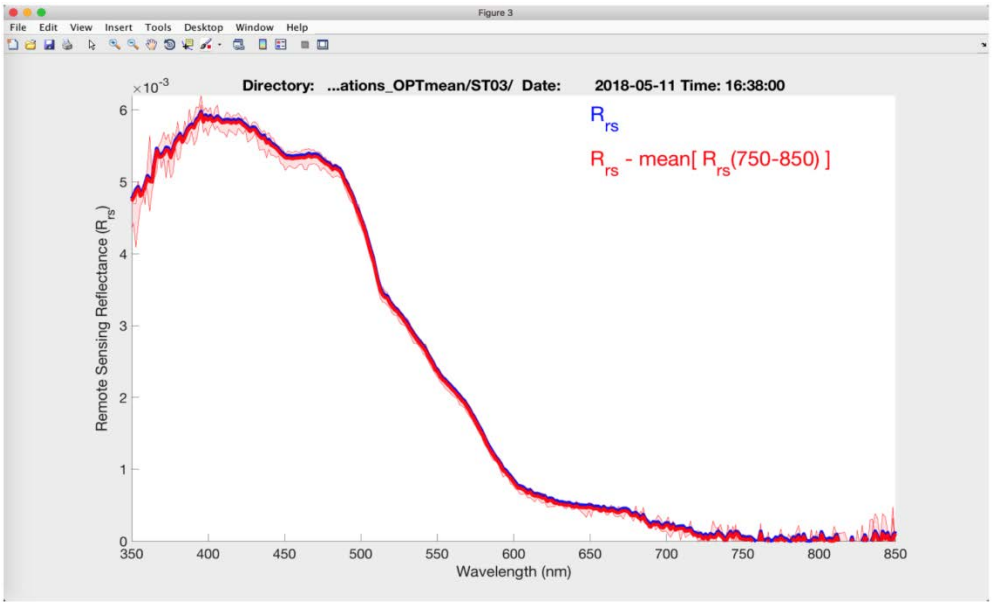

Figure 51. $R_{rs}(\lambda)$ for Station 03 computed from Spectral Evolution Spectrometer measurements after automated removal of outliers and a subtraction in the red end of the spectrum (above 750 nm); the light red shading shows the results of maximum and minimum $R_{rs}(\lambda)$ computation.

Data and Results Summary

The OSU station notes for the data logging are in OSU online Appendix C (http://meris.coas.oregonstate.edu/tmp/OSU_NOAA_CRUISE_REPORT_2018_05/OSU_4_REPORT_A

PPENDIX_C_OSU_STATION_LOG_TXT.txt). The logs include stations times, measurement sequence, observed conditions and sampling locations as close as practical prior to the OSU above-water radiometry. The profiling radiometry was often conducted within 30 min to an hour of the above-water measurements, except when sea-state, excessive wind or sky conditions prevented instrument deployment. Stations 02 through 17 are in the Gulf of Mexico, while Stations 18 through 24, as well as Station 01 (just South of the departure point in Key West), are in the Atlantic Ocean on the Florida Shelf. Figure 52and Figure 53 show the summary of $R_{rs}(\lambda)$ results for all measured stations using the OSU Spectral Evolution (above-water) and HyperPro (profiling) instruments respectively.

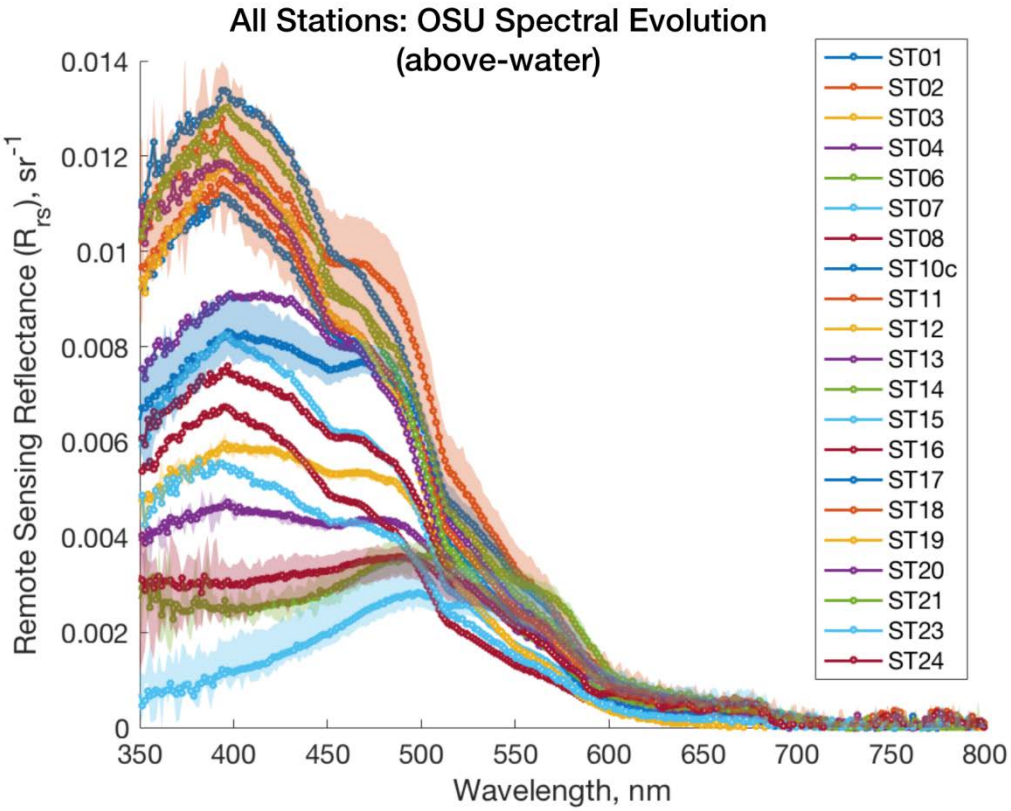

Figure 52. Spectral Evolution $R_{rs}(\lambda)$ above-water results for all stations obtained by OSU aboard the NOAA Ship *Okeanos Explorer* during the May 2018 VIIRS Cal/Val Cruise

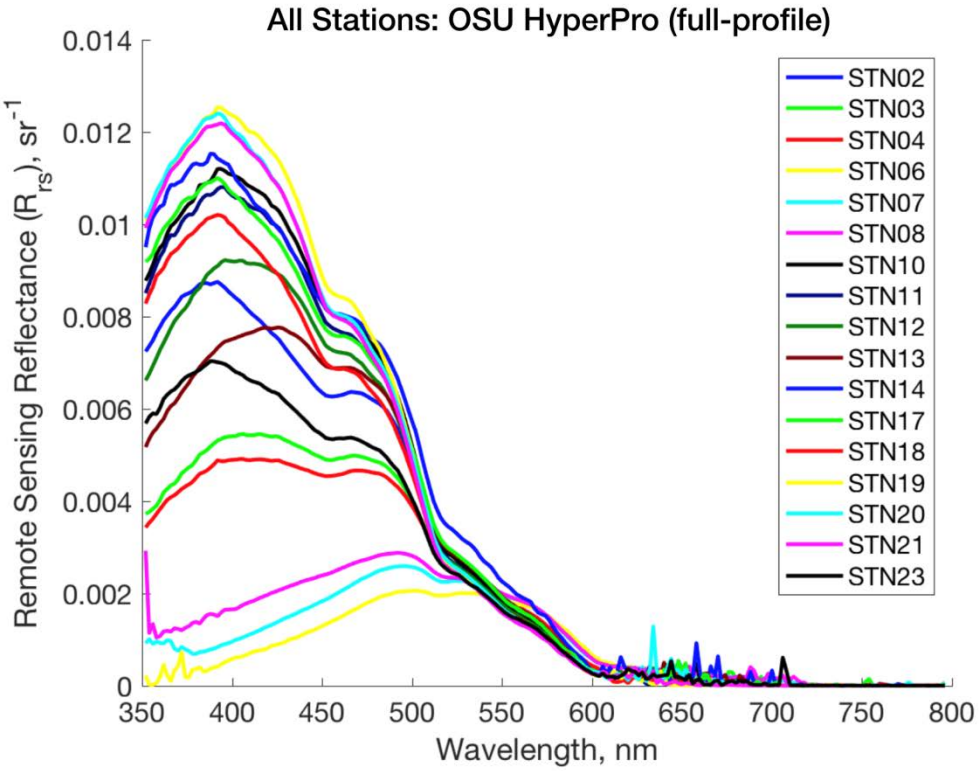

Figure 53. HyperPro $R_{rs}(\lambda)$ profiling results for all stations obtained by OSU aboard the NOAA Ship *Okeanos Explorer* during the May 2018 VIIRS Cal/Val Cruise

A majority of the spectra show uniformly blue water in the Gulf of Mexico and the Florida Shelf with a peak in the reflectance spectra around 400 nm. Stations 06, 07 and 08 show more CDOM and more biomass toward the approach to the Mississippi River with peak reflectance around 500 nm. Stations 10, 12 and 13 are more mixed water types, with observations of sargassum, bird and marine sea-life, including remoras and dogfish and nurse-sharks noted in the station log at the interface of eddies in the 'Loop Current'. All of the individual station results for the OSU HyperPro measurements from this cruise are plotted in OSU online Appendix D (http://meris.coas.oregonstate.edu/tmp/OSU_NOAA_CRUISE_REPORT_2018_05/OSU_5_REPORT_APPENDIX_D_OSU_HYPERPRO_RRS_PLOTS_PDF.pdf) and also OSU Spectral Evolution above-water measurement are in OSU online Appendix E (http://meris.coas.oregonstate.edu/tmp/OSU_NOAA_CRUISE_REPORT_2018_05/OSU_6_REPORT_APPENDIX_E_OSU_SEV_RRS_PLOTS_AND_COMPARISONS.pdf), which includes an measurement of error contributions from sky-view obscurations, and provides more direct comparisons with the OSU profiling HyperPro measurements for individual stations.

We quantified the correlation between the $R_{rs}(\lambda)$ from the above-water and from the profiling measurement methods deployed by OSU across the VIIRS spectral bands for all stations in Figure 54 (left). Here the error bars represent the measurement variability across all measurement samples at that station. In the case of the profiling HyperPro measurement, this includes the multiple 'yoyo' casts at each station. For the above-water Spectral Evolution R_{rs}, the maximum and minimum at each station are obtained by selecting the appropriate combination of maximum and minimum spectra for water, sky and plaque obtained at each station and which are not rejected by the outlier removal method discussed earlier. The same comparison is shown in Figure 54 (right), but here the stations with low sun-angle, variable sky illumination conditions are removed, showing improved agreement between the two methods

when optimal conditions are met. Thresholds for data exclusion include: above water data taken at stations with solar azimuth greater than approximately 65 degrees, scattered (and fast-moving) clouds exceeding 20% cover, or unusually high resulting measurement variability.

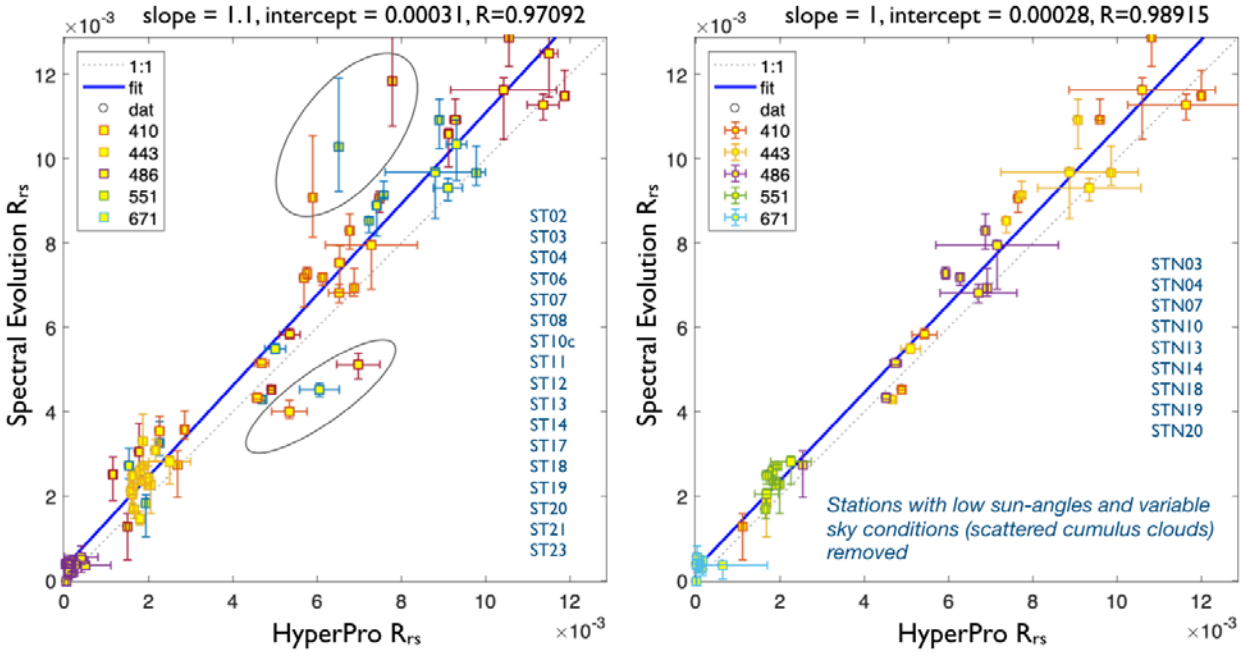

Figure 54. (Left) HyperPro profiling and Spectral Evolution above-water $R_{rs}(\lambda)$ comparisons across VIIRS bands for all stations. (Right) Same comparison performed after removing stations with variable sky illumination angles and low-sun angles

This analysis was also performed for OSU measurements carried out during the prior VIIRS Cal/Val cruise in October 2016 on the heels of Hurricane Matthew [Ondrusek et al., 2017]. The result is shown in Figure 55 for all stations at which measurements were taken during that cruise. The agreement between the two measurement methods is comparable to results for all stations of the 2018 cruise and shows that both measurements produce a similar level of measurement variability. This provides us with confidence that both methods are suitable for satellite calibration and validation if carried out according to our measurement protocols, described previously in this section.

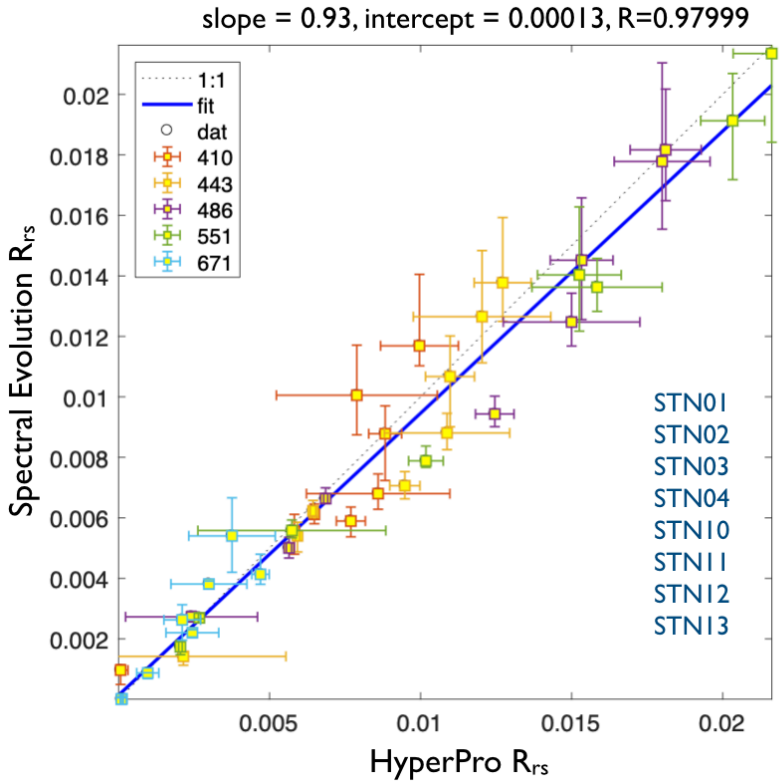

Figure 55. In-water (profiling) and above-water $R_{rs}(\lambda)$ comparisons across VIIRS bands for all stations during 2016 VIIRS Cal/Val Cruise from Charleston, South Carolina

Plaque Comparison Studies

Above water $R_{rs}(\lambda)$ measurements conducted by the teams during the VIIRS Cal/Val cruises use different instruments and slight differences in measurement protocols. In particular, multiple plaques are used including several Spectralon 'white' 99% reflectance plaques and 'gray' 10% reflectance plaques. During the 2018 cruise and attempt was made to compare the remote sensing reflectance uncertainty contributions from the use of different plaques, by having teams perform measurements of a single 99% reflectance plaques alongside their standard protocols. The NOAA 'white' 25 cm x 25 cm plaque located on a bollard on the foredeck of the *Okeanos Explorer* was used as the reference and is shown in Figure 56. The plaque orientation with respect to the solar azimuth was periodically adjusted by Carol Johnson of NIST if the ship's heading altered significantly during the measurements on station.

Figure 56. NOAA ‘white’ 99% reflectance plaque on a mooring bollard of the *Okeanos Explorer* foredeck

To compare the measurement results of the OSU above-water $R_{rs}(\lambda)$ protocol to other methods, we performed additional measurements of the NOAA 'white’ plaque reflectance for several stations. Care was taken to measure the NOAA and the OSU smaller format 12.7 cm x 12.7 cm ‘white’ plaque from consistent orientations relative to the solar azimuth and as close in time as practical. Additionally, measurements were taken at 90° and 135° relative to solar azimuth at several stations. $R_{rs}(\lambda)$ results processed using the different plaque measurements are shown in Figure 57. The same sky and water spectra obtained at that station were used, and results show very small measurement differences due to plaque orientation and choice of ’white’ 99% reflectance plaque.

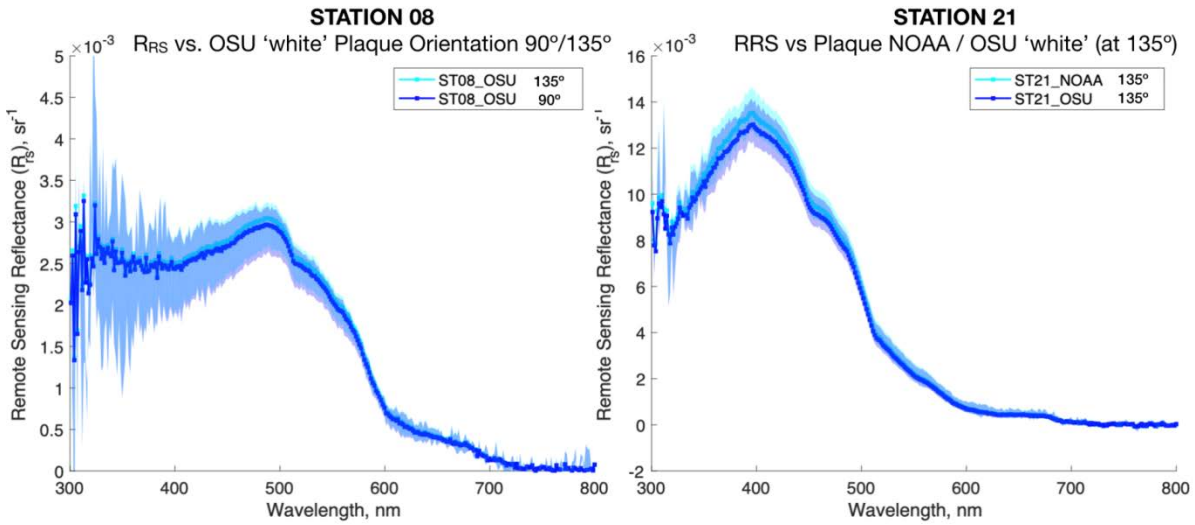

Figure 57. $R_{rs}(\lambda)$ as a function of plaque orientation for Station 08 (left) and vs Spectralon plaque type OSU ‘white’ vs. NOAA ‘white’ for Station 21 (right)

OSU protocol also requires the measurement of the OSU plaque to be done at the same measurement location where water and sky spectra are collected, and in the case of the *Okeanos Explorer*, the optimal location was on either side of the bow depending on the ship's heading relative to the solar azimuth. Extending on our direct field comparisons between different plaque measurements done in prior cruises, here we processed the $R_{rs}(\lambda)$ results using the OSU plaque measurement using the standard method and compared this result to processing using the plaque measurement the NOAA 'white' target in its 'standard' location in the middle of the fore-deck, as shown previously in Figure 56. Due to the differences in plaque location and height above deck, the main difference comes from the sky viewing geometry (illumination) differences due to obscurations and additional reflectances arising from the ship's superstructure. The $R_{rs}(\lambda)$ and normalized $R_{rs}(\lambda)$ results for these measurements for Stations 04, 06 and 07 are shown in Figure 58, while the sea and sky conditions for these stations is documented in Figure 59.

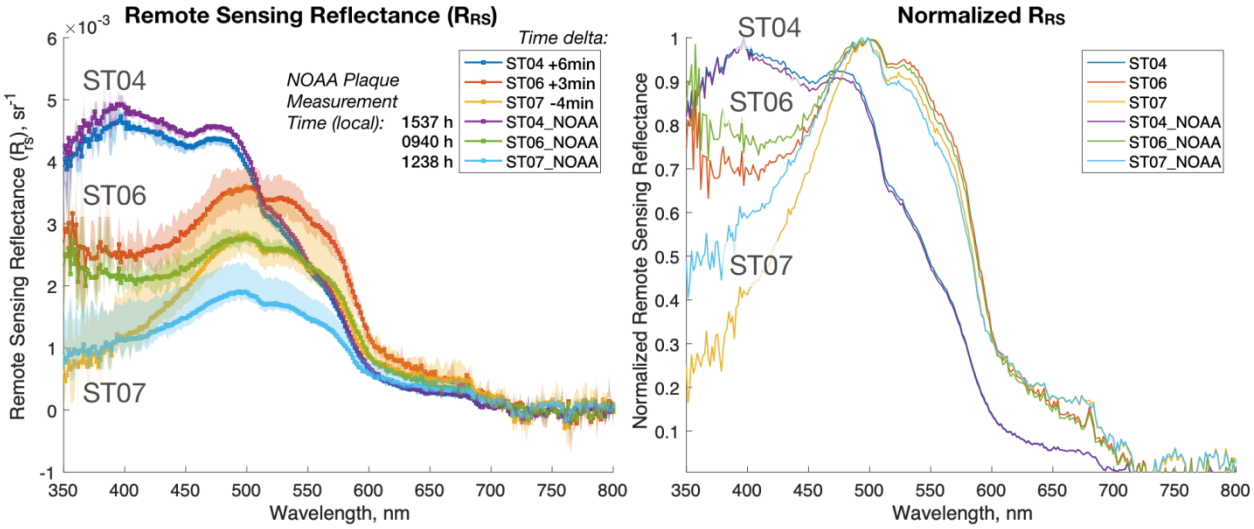

Figure 58. $R_{rs}(\lambda)$ comparison between NOAA white, plaque on foredeck of *Okeanos Explorer* vs. OSU standard protocol for three stations (left). Plot on right hand side shows normalized spectral shape differences for the same measurements.

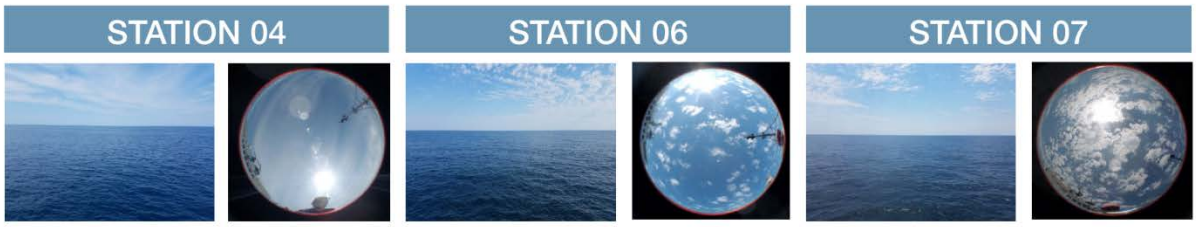

Figure 59. Images documenting the sea and sky illumination (cloud cover and sun angle) conditions for the three stations in the plaque comparison study

Here we see that even though the OSU plaque measurement was carried out with minimal delay (within less than 6 min) from the measurement of the NOAA plaque, the discrepancies in the R_{rs} spectra are more significant. The discrepancies are both spectrally dependent, particularly in the blue part of the electromagnetic spectrum (<450 nm), and contain a broad (spectrally-independent) radiance offset between the 'white' plaque measurements. We attribute both differences primarily to the shipboard location of the two plaque measurements. The $R_{rs}(\lambda)$ differences are largest for Stations 06 and 07, when the sky illumination is inhomogeneous and solar angles are lower.

OSU Summary

$R_{rs}(\lambda)$ was obtained for all stations with good matches between HyperPro and Spectral Evolution measurements, particularly for stations with clear skies and high solar elevation. We quantitatively compared the agreement between our two in situ methods for this cruise, and benchmarked this against the regressions obtained from the 2016 VIIRS cruise [Ondrusek et al., 2017]. For both cruises, we obtain R^2 coefficient values above 0.95 even when including measurements from all stations. We continue to work on methods to reduce the experimental measurement uncertainty for both methods. We show evidence that plaque illumination obscurations and additive reflectances from the ship's superstructure are more significant sources of error compared to plaque-to-plaque differences and the angular (BRDF) response of the 'white' Spectralon plaque. Therefore, shipboard measurement locations need to be better controlled for the group to reduce the above-water measurement variations. For above-water measurements, the overall experimental sources of uncertainty need to be better quantified to develop a model for the comprehensive error budget (work under discussion currently with NIST), followed by more systematically implementing protocol modifications to minimize the largest error contributions.

Finally, we continue to refine our above-water $R_{rs}(\lambda)$ processing software and have made improvements in measurement uncertainty analysis. Several teams in the NOAA VIIRS Ocean Color Cal/Val program are now successfully using our codes for above-water processing, most notably NRL and UMB. We have added initial flexibility to process above-water results for multiple radiometric instruments, including SpectraVista GER and Malvern Panalytical ASD spectrometers and are currently in the process of comparing above-water results from multiple instruments for a subset of the stations from this cruise. These results are posted here: (http://meris.coas.oregonstate.edu/tmp/OSU_NOAA_CRUISE_REPORT_2018_05/http://meris.coas.oregonstate.edu/tmp/OSU_NOAA_CRUISE_REPORT_2018_05/OSU_7_REPORT_APPENDIX_F_OSU_AWG_3STATION_COMPARISON.pdf). Other data, results and reports are included in the OSU reports archive for this project. (http://meris.coas.oregonstate.edu/tmp/OSU_NOAA_CRUISE_REPORT_2018_05/).

11.9 U. Miami – Kenneth J. Voss

NuRads measurements of the BRDF or Radiance Distribution

NuRads measures the spectral upwelling radiance distribution [Voss and Chapin, 2005]. The upwelling light field from the same water type in the ocean varies with the illumination geometry and the measurement geometry. Almost all in situ measurements of the upwelling radiance used for satellite validation/calibration are made in the nadir direction (instrument looking straight down, light coming straight up), however the satellite views the ocean at different angles, depending on where the specific pixel is in the satellite scan line. To relate the measurement made on the ground to what the satellite is viewing requires information on the variation of the radiance with direction, which is the radiance distribution. The shape of the radiance distribution also changes spectrally, so the spectral variation of the radiance distribution must also be determined. This is exactly the parameter that NuRads measures.

The model currently used in the data reduction process of satellite data is provided in Morel et al., 2002. This model has been validated several times [Gleason et al., 2012; Voss et al., 2007; Voss and Morel, 2005], but the model is aimed at Case I waters (i.e., open ocean, oligotrophic; water parameters determined by a statistical relationship with Chl-*a*), and breaks down in coastal waters. While we have taken a considerable amount of open ocean radiance distribution data, and some coastal radiance distribution data, because of the variability of the water properties in the coastal area it is reasonable to expand the data set and to take radiance distribution data along with other validation data when doing experiments such as this.

The NuRads instrument was calibrated following previously published protocols [Voss and Chapin, 2005; Voss and Zibordi, 1989]. During the May 2018 cruise, NuRads was deployed by NOAA personnel. When deployed, floats are attached to the instrument and it is floated 20 m to 50 m away from the ship, at the surface (measurement depth is 0.75 m). When deployed, the instrument measures the upwelling radiance continuously, cycling through the six different wavelengths and associated dark measurements. NuRads measurements were made at Stations 1, 2, 3 and 4. The data have been reduced and processed and quality control is currently being conducted.

12 Conclusion

The 2018 dedicated VIIRS Cal/Val cruise aboard the NOAA Ship *Okeanus Explorer* took place in the Gulf of Mexico and Atlantic coastal waters of Florida. In situ AOP radiometry and IOP optical measurements were made with multiple instruments deployed in several modes (e.g., profiling, flow-through, etc.) and water samples were collected for later processing to provide measurements of additional ocean properties. Uncertainties in the in situ and satellite validation measurements will be estimated by utilizing pre- and post-cruise calibrations of instruments, simultaneous measurements of parameters utilizing multiple techniques and instruments and evaluation of data processing techniques.

Furthermore, the cruise presented the opportunity to optically characterize the Gulf of Mexico Loop Current. Oceanic processes will be investigated using multiple platform techniques, which include near-real time satellite measurements, in situ flow-through, profiling, and above-water data. Spatial gradients will be studied using in situ data and compared with VIIRS data to assess the ability of VIIRS to capture the scales and magnitude of naturally occurring variability in dynamic coastal waters.

In summary, observations from this cruise along with those from the three previous dedicated VIIRS Cal/Val cruises [Ondrusek et al., 2017; Ondrusek et al., 2016; Ondrusek et al., 2015] have added a significant number of validation-quality in situ match-ups for a comprehensive evaluation of VIIRS performance validation techniques and various ocean color applications.

13 Cruise Data Access

All data collected on this cruise will be formally archived with NOAA/NCEI according to their guidelines and will also be publicly accessible through NOAA CoastWatch/OceanWatch. Data users are strongly urged to communicate with cruise investigators for appropriate collaborations and citations. Some data from this cruise have been or will be submitted to the NASA SeaBASS archive.

14 Acknowledgments

Funding for this project was provided as follows: JPSS VIIRS Ocean Color Cal/Val funding supported most of the science groups' participation; NOAA/NESDIS/STAR Product Development, Readiness and Application (PDR&A)/Ocean Remote Sensing (ORS) program provided additional support to assist in LDEO participation. Groups external to the JPSS VIIRS Ocean Color Cal/Val team also provided their own support. NOAA/OMAO awarded ship time and crew support and we thank the crew of the NOAA Ship *Okeanos Explorer* for their support in making data collection possible. NASA/GSFC will perform laboratory analyses on discrete water samples for some parameters. We are grateful to Catherine Cooksey, Thomas Germer, Heather Patrick, and Howard Yoon for their measurements of the blue tile and white and gray sintered PTFE, and Georgi Georgiev of NASA/GSFC for BRDF measurements of the blue tile. We thank Alexandre Castagna for many useful discussions, for including the blue tile in the COSBY cruise, and for assistance with the GOSI data. NOAA supported the NIST work through Interagency Agreement IAA number NOAA2015-11-0000-0002. NOAA VIIRS SNPP ocean color satellite data were obtained through NOAA CoastWatch/OceanWatch/PolarWatch. We thank David W. Allen and an anonymous reviewer, both from NIST, for their comments and edits. The views, opinions, and findings contained in this report are those of the authors and should not be construed as an official NOAA or US Government position, policy, or decision.

15 References Cited

Arnone, R., M. Fargion, P. Martinolich, S. Ladner and e. al. (2012), Validation of the VIIRS Ocean color, *Proc. SPIE 8372, Ocean Sensing and Monitoring IV, 83720G*, doi: http://dx.doi.org/10.1117/12.922949.

Arnone, R., R.A. Vandermeulen, S. Ladner, J. Bowers, P. Martinolich, M. Fargion and M. Ondrusek (2014), Sensitivity of calibration "gains" to ocean color processing in coastal and open waters using ensembles members for NPP- VIIRS, *Proc. SPIE 9111, Ocean Sensing and Monitoring VI, 911105.* , doi: http://dx.doi.org/10.1117/12.2053409.

Bibby, T.S., M.Y. Gorbunov, K.W. Wyman and P.G. Falkowski (2008), Photosynthetic community responses to upwelling in mesoscale eddies in the subtropical North Atlantic and Pacific Oceans, *Deep Sea Research Part II: Topical Studies in Oceanography*, *55*(10–13), 1310-1320, doi: 10.1016/j.dsr2.2008.01.014.

Booth, B.C. (1993), *Estimating cell concentration and biomass of autotrophic plankton using microscopy.*, Lewis Publishers, Boca Raton, Florida, USA.

Carder, K.L. and R.G. Steward (1985), A remote-sensing reflectance model of a red-tide dinoflagellate off West Florida, *Limnol. Oceanogr.*, *30*(2), 286-298.

Castagna, A. (2017), *Personal Communication*.

Castagna, A., W. Vyverman, K. Sabbe, B.C. Johnson, H. Patrick, T.A. Germer, K. Voss, H. Dierssen and Z. Shang (2019), Irradiance estimates with the plaque method, *Appl. Optics, Submitted*.

Chekalyuk, A. and M. Hafez (2008), Advanced laser fluorometry of natural aquatic environments, *Limnology and Oceanography: Methods*, *6*(11), 591-609, doi: doi:10.4319/lom.2008.6.591.

Chekalyuk, A.M., M.R. Landry, R. Goericke, A.G. Taylor and M.A. Hafez (2012), Laser fluorescence analysis of phytoplankton across a frontal zone in the California Current ecosystem, *J. Plankton Res.*, *34*(9), 761-777, doi: 10.1093/plankt/fbs034.

Clark, D.K., H.R. Gordon, K.J. Voss, Y. Ge, W. Broenkow and C. Trees (1997), Validation of atmospheric correction over the oceans, *J. Geophys. Res.-Atmos.*, *102*(D14), 17209-17217, doi: 10.1029/96jd03345.

English, D. (2018), In situ gray plaque correction factors, *Personal Communication*.

EPA (1971), Methods for chemical analysis of water and wastes, EPA-NERL: 160.2, US Environmental Protection Agency.

Georgiev, G.T. and J.J. Butler (2008), BRDF study of gray-scale Spectralon, *Proc. SPIE*, *7081*, 708107.

Germer, T.A. (2017), Full four-dimensional and reciprocal Mueller matrix bidirectional reflectance distribution function of sintered polytetrafluoroethylene, *Appl. Optics*, *56*(33), 9333 - 9340, doi: 10.1364/AO.56.009333.

Germer, T.A. and C.C. Asmail (1997), A goniometric optical scatter instrument for bidirectional reflectance distribution function measurements with out-of-plane and polarimetry capabilities, *Proc. SPIE*, *3141*, 220 - 231, doi: 10.1117/12.279240.

Gilerson, A., C. Carrizo, R. Foster and T. Harmel (2018), Variability of the reflectance coefficient of skylight from the ocean surface and its implications to Ocean Color, *Optics Express*, *26*(8), 9615-9633.

Gleason, A.C.R., K.J. Voss, H.R. Gordon, M. Twardowski, J. Sullivan, C. Trees, A. Weidemann, J.F. Berthon, D. Clark and Z.P. Lee (2012), Detailed validation of the bidirectional effect in various Case I and Case II waters, *Optics Express*, *20*(7), 7630-7645, doi: 10.1364/oe.20.007630.

Goes, J.I., H.d.R. Gomes, E.M. Haugen, K.T. McKee, E.J. D'Sa, A.M. Chekalyuk, D.K. Stoecker, P.J. Stabeno, S.-I. Saitoh and R.N. Sambrotto (2014a), Fluorescence, pigment and microscopic characterization of Bering Sea phytoplankton community structure and photosynthetic competency in the presence of a Cold Pool during summer, *Deep Sea Research Part II: Topical Studies in Oceanography*, *109*(0), 84-99, doi: 10.1016/j.dsr2.2013.12.004.

Goes, J.I., H.d.R. Gomes, A.M. Chekalyuk, E.J. Carpenter, J.P. Montoya, V.J. Coles, P.L. Yager, W.M. Berelson, D.G. Capone, R.A. Foster, D.K. Steinberg, A. Subramaniam and M.A. Hafez (2014b), Influence of the Amazon River discharge on the biogeography of phytoplankton communities in

the western tropical north Atlantic, *Prog. Oceanogr.*, *120*(0), 29-40, doi: 10.1016/j.pocean.2013.07.010.
Gorbunov, M.Y. and P.G. Falkowski (2004), Fluorescence induction and relaxation (FIRe) technique and instrumentation for monitoring photosynthetic processes and primary production in aquatic ecosystems, (ed.), *Proceedings of Photosynthesis: Fundamental Aspects to Global Perspectives"-Proc. 13th International Congress of Photosynthesis, Montreal, Aug*.
Gordon, H.R. (2010), Some reflections on thirty-five years of ocean-color remote sensing, in *Oceanography from Space: Revisited*, Edited by Barale, V., Gower, J.F.R. and Alberotanza, L., 289-305, Springer Netherlands.
Gordon, H.R., D.K. Clark, J.L. Mueller and W.A. Hovis (1980), Phytoplankton Pigments from the Nimbus-7 Coastal Zone Color Scanner: Comparisons with Surface Measurements, *Science*, *210*(4465), 63-66, doi: 10.2307/1684604.
Gould, R.W., R.A. Arnone and M. Sydor (2001), Absorption, scattering; and remote-sensing reflectance relationships in coastal waters: Testing a new inversion algorithm, *J. Coast. Res.*, *17*(2), 328-341.
Groetsch, P.M., P. Gege, S.G. Simis, M.A. Eleveld and S.W. Peters (2017), Validation of a spectral correction procedure for sun and sky reflections in above-water reflectance measurements, *Optics express*, *25*(16), A742-A761.
GUM (1995), Evaluation of measurement data - Guide to the expression of uncertainty in measurement (ed.), http://www.bipm.org/en/publications/guides/gum.html. http://www.bipm.org/en/publications/guides/gum.html.
Holm-Hansen, O. and B. Riemann (1978), Chlorophyll a determination: improvements in methodology, *Oikos*, *30*, 438-447.
Hovis, W.A., D.K. Clark, F. Anderson, R.W. Austin, W.H. Wilson, E.T. Baker, D. Ball, H.R. Gordon, J.L. Mueller, S.Z. El-Sayed, B. Sturm, R.C. Wrigley and C.S. Yentsch (1980), Nimbus-7 Coastal Zone Color Scanner: System Description and Initial Imagery, *Science*, *210*(4465), 60-63, doi: 10.2307/1684603.
Hunter, C. (2006), Particulate organic carbon, nitrogen and total suspended matter. Methodologies, protocols and analyses used in the development of ocean color product algorithms., Technical Publication 06–1 (ed.), Moss Landing Marine Laboratories.
IOCCG (2018), Protocols for Satellite Ocean Color Data Validation: In situ Optical Radiometry. (ed.), *IOCCG Protocol Series*, No. in preparation, International Ocean Colour Coordinating Group, Dartmouth, NS, Canada.
Johnson, B.C., J. Rice, H. Yoon and A. Parr (2014), Principles of optical radiometry, in *Optical radiometry for ocean climate measurements*, edited by Zibordi, G., Donlon, C. and Parr, A., pp. 13-67, Academic Press, Waltham, MA.
Kishino, M., M. Takahashi, N. Okami and S. Ichimura (1985), Estimation of the spectral absorption coefficients of phytoplankton in the sea, *Bulletin of Marine Science*, *37*(2), 634-642.
Lee, Z., Y.-H. Ahn, C. Mobley and R. Arnone (2010), Removal of surface-reflected light for the measurement of remote-sensing reflectance from an above-surface platform, *Optics Express*, *18*(25), 26313-26324.
Lee, Z., S. Shang, L. Qi, J. Yan and G. Lin (2016), A semi-analytical scheme to estimate Secchi-disk depth from Landsat-8 measurements, *Remote Sensing of Environment*, *177*, 101-106.
Lee, Z., J. Wei, K. Voss, M. Lewis, A. Bricaud and Y. Huot (2015a), Hyperspectral absorption coefficient of "pure" seawater in the range of 350–550 nm inverted from remote sensing reflectance, *Applied Optics*, *54*(3), 546-558.
Lee, Z., S. Shang, C. Hu, K. Du, A. Weidemann, W. Hou, J. Lin and G. Lin (2015b), Secchi disk depth: A new theory and mechanistic model for underwater visibility, *Remote Sensing of Environment*, *169*, 139-149.
Lee, Z.P., K.L. Carder and R.A. Arnone (2002), Deriving inherent optical properties from water color: a multiband quasi-analytical algorithm for optically deep waters, *Appl. Optics*, *41*(27), 5755-5772, doi: 10.1364/ao.41.005755.

Lee, Z.P., K.P. Du and R. Arnone (2005a), A model for the diffuse attenuation coefficient of downwelling irradiance, *Journal of Geophysical Research-Oceans*, *110*(C2), C02017, doi: Doi 10.1029/2004jc002275.

Lee, Z.P., N. Pahlevan, Y.-H. Ahn, S. Greb and D. O'Donnell (2013), Robust approach to directly measuring water-leaving radiance in the field, *Appl. Optics*, *52*(8), 1693-1701.

Lee, Z.P., K.L. Carder, R.G. Steward, T.G. Peacock, C.O. Davis and J.L. Mueller (1997), *Remote-sensing reflectance and inherent optical properties of oceanic waters derived from above-water measurements*, 160-166 pp., Spie - Int Soc Optical Engineering, Bellingham, doi: 10.1117/12.266436.

Lee, Z.P., M. Darecki, K.L. Carder, C.O. Davis, D. Stramski and W.J. Rhea (2005b), Diffuse attenuation coefficient of downwelling irradiance: An evaluation of remote sensing methods, *Journal of Geophysical Research-Oceans*, *110*(C2), C02016, doi: Doi 10.1029/2004jc002573.

MacIssac, E.A. and J.G. Stockner (1993), Enumeration of phototrophic picoplankton by autofluorescence microscopy., in *Handbook of Methodology in Aquatic Microbial Ecology*, Edited by Kemp.P.F., Sherr, B.F., Sherr, E.B. and J., C.J., 187-197, Lewis Publishers, Boca Raton, Florida, USA.

Mikelsons, K. and M. Wang (2019), Optimal satellite orbit configuration for global ocean color product coverage, *Opt. Express*, *in press.*

Mobley, C.D. (1999), Estimation of the remote-sensing reflectance from above-surface measurements, *Appl. Optics*, *38*(36), 7442-7455, doi: 10.1364/ao.38.007442.

Mobley, C.D. (2015), Polarized reflectance and transmittance properties of windblown sea surfaces, *Appl. Optics*, *54*(15), 4828-4849, doi: 10.1364/ao.54.004828.

Morel, A., D. Antoine and B. Gentili (2002), Bidirectional reflectance of oceanic waters: accounting for Raman emission and varying particle scattering phase function, *Appl. Optics*, *41*(30), 6289-6306, doi: 10.1364/ao.41.006289.

Mueller, J.L., C.O. Davis, R. Arnone, R. Frouin, K. Carder, Z.P. Lee, R.G. Steward, S.B. Hooker, C.D. Mobley and S. McLean (2003a), Above-water radiance and remote sensing reflectance measurement and analysis protocols, in *Ocean Optics Protocols For Satellite Ocean Color Sensor Validation, Revison 4, Volume III: Radiometric Measurements and Data Analysis Protocols*, Edited by Mueller, J.L., Fargion, G.S. and Mcclain, C., NASA/TM-2003-21621/Rev4-Vol III, p.^pp. 21 - 31, Goddard Space Flight Center, National Aeronautics and Space Administration, Greenbelt, Maryland.

Mueller, J.L., A. Morel, R. Frouin, C. Davis, R. Arnone, K. Carder, Z.P. Lee, R.G. Steward, S. Hooker, C.D. Mobley, S. McLean, B. Holben, M. Miller, C. Pietras, K.D. Knobelspiesse, G.S. Fargion, J. Porter and K. Voss (2003b), *NASA Tech. Memo. 2003-21621/Rev-Vol III*, Ocean optics protocols for satellite ocean color sensor validation, revision 4, Ocean optics protocols for satellite ocean color sensor validation, Mueller, J.L., Fargion, G.S. and Mcclain, C.R. (ed.), NASA Goddard Space Flight Center, Greenbelt, Maryland.

Nicodemus, F.E., J.C. Richmond, J.J. Hsia, I.W. Ginsberg and T. Limperis (1977), *Geometrical Considerations and Nomenclature for Reflectance*, 34 plus appendices pp., Washington, D. C. 20402.

Ondrusek, M., E. Stengel, C.S. Kinkade, R.L. Vogel, P. Keegstra, C. Hunter and C. Kim (2012), The development of a new optical total suspended matter algorithm for the Chesapeake Bay, *Remote Sensing of Environment*, *119*, 243-254, doi: 10.1016/j.rse.2011.12.018.

Ondrusek, M., E. Stengel, V.P. Lance, M. Wang, K. Voss, G. Zibordi, M. Talone, Z. Lee, J. Wei, J. Lin, et al. (2015), Report for Dedicated JPSS VIIRS Ocean Color Calibration/Validation Cruise, NOAA/NESDIS Technical Report #146, Lance, V.P. (ed.) 60 pp, National Oceanic and Atmospheric Administration, US Department of Commerce, Washington, DC. doi: 10.7289/V52B8W0Z.

Ondrusek, M., V.P. Lance, M. Wang, E. Stengel, C. Kovach, R. Arnone, S. Ladner, W. Goode, A. Gilerson, S. Ahmed, et al. (2017), Report for Dedicated JPSS VIIRS Ocean Color Calibration/Validation Cruise October 2016 NOAA/NESDIS Technical Report #151, Lance, V.P.

(ed.) 75 pp, National Oceanic and Atmospheric Administration, US Department of Commerce, Washington, DC. doi: doi:10.7289/V5/TR-NESDIS-151.

Ondrusek, M., V.P. Lance, E. Stengel, M. Wang, R. Arnone, S. Ladner, W. Goode, R. Vandermeulen, S. Freeman, C.J. E., et al. (2016), Report for Dedicated JPSS VIIRS Ocean Color Calibration/Validation Cruise December 2015 NOAA/NESDIS Technical Report #148, Lance, V.P. (ed.) 66 pp, National Oceanic and Atmospheric Administration, US Department of Commerce, Washington, DC. doi: doi:10.7289/V5/TR-NESDIS-148.

Patrick, H.J., C.J. Zarobila and T.A. Germer (2013), The NIST Robotic Optical Scatter Instrument (ROSI) and its application to BRDF measurements of diffuse reflectance standards for remote sensing, *Proc. SPIE*, *8866*, 886615-886611 886615-886612.

Pope, R.M. and E.S. Fry (1997), Absorption spectrum (380-700 nm) of pure water .2. Integrating cavity measurements, *Appl. Optics*, *36*(33), 8710-8723, doi: 10.1364/ao.36.008710.

Proctor, J.E. and P.Y. Barnes (1996), NIST high accuracy reference reflectometer-spectrophotometer, *J. Res. NIST*, *101*(5), 619 - 627.

Ruddick, K. (2018), Measurement Requirements and Protocols when Operating Fiducial Reference Measurement (FRM) Ocean Colour Radiometers (OCR) used for Satellite Validation, FRM4SOC-TR1 Technical Report TR- 1 (ed.), in preparation.

Satlantic (2003), Operation Manual for Profiler II (ed.), Satlantic Incorporated, Halifax, Nova Scotia.

Satlantic (2004), SatView Data Logging / Display Program Users Guide; Version 2.8 (ed.), Satlantic Incorporated, Halifax, Nova Scotia.

Satlantic (2012), Operation Manual for Profiler II (ed.), Satlantic Incorporated, Halifax, Nova Scotia.

Shang, Z., Z. Lee, Q. Dong and J. Wei (2017), Self-shading associated with a skylight-blocked approach system for the measurement of water-leaving radiance and its correction, *Applied Optics*, *56*(25), 7033-7040.

Sokoletsky, L.G. and F. Shen (2014), Optical closure for remote-sensing reflectance based on accurate radiative transfer approximations: the case of the Changjiang (Yangtze) River Estuary and its adjacent coastal area, China, *International Journal of Remote Sensing*, *35*(11-12), 4193-4224.

Tassan, S. and G.M. Ferrari (1995), An alternative approach to absorption measurements of aquatic particles retained on filters, *Limnol. Oceanogr.*, *40*(8), 1358-1368, <Go to ISI>://000167854100002.

Tomas, C.R. (1997), *Identifying marine phytoplankton*, Academic press.

Van Heukelem, L. and C.S. Thomas (2001), Computer-assisted high-performance liquid chromatography method development with applications to the isolation and analysis of phytoplankton pigments, *Journal of Chromatography A*, *910*(1), 31-49, doi: 10.1016/s0378-4347(00)00603-4.

Voss, K.J. and G. Zibordi (1989), Radiometric and geometric calibration of a spectral electro-optic “fisheye" camera radiance distribution system, *J. Atmosph. and Ocean. Techn.*, *6*, 652-662.

Voss, K.J. and A.L. Chapin (2005), Upwelling radiance distribution camera system, NURADS, *Optics Express*, *13*(11), 4250-4262, doi: 10.1364/opex.13.004250.

Voss, K.J. and A. Morel (2005), Bidirectional reflectance function for oceanic waters with varying chlorophyll concentrations: Measurements versus predictions, *Limnol. Oceanogr.*, *50*(2), 698-705.

Voss, K.J., A. Morel and D. Antoine (2007), Detailed validation of the bidirectional effect in various Case 1 waters for application to ocean color imagery, *Biogeosciences*, *4*(5), 781-789.

Wang, M., S. Son and W. Shi (2009), Evaluation of MODIS SWIR and NIR-SWIR atmospheric correction algorithms using SeaBASS data, *Remote Sensing of Environment*, *113*(3), 635-644, doi: 10.1016/j.rse.2008.11.005.

Wang, M., X. Liu, L. Jiang and S. Son (2017), The VIIRS Ocean Color Product Algorithm Theoretical Basis Document, National Oceanic and Atmospheric Administration, National Environmental Satellite and Data Information Service, 68 pp., doi: TBD.

Wang, M., X. Liu, L. Tan, L. Jiang, S. Son, W. Shi, K. Rausch and K. Voss (2013), Impact of VIIRS SDR performance on ocean color products, *J. Geophys. Res. Atmos.*, *118*, 10347–10360, doi: doi:10.1002/jgrd.50793.

Wang, M., X. Liu, L. Jiang, S. Son, J. Sun, W. Shi, L. Tan, P. Naik, K. Mikelsons, X. Wang and V. Lance (2014), Evaluation of VIIRS Ocean Color Products, *Proc. SPIE 9261*, *92610E*, doi: 10.1117/12.2069251.

Wei, J.W., Z.P. Lee and S.L. Shang (2016), A system to measure the data quality of spectral remote-sensing reflectance of aquatic environments, *J. Geophys. Res.-Oceans*, *121*(11), 8189-8207, doi: 10.1002/2016jc012126.

Welschmeyer, N.A. (1994), Fluorometric analysis of chlorophyll-*a* in the presence of chlorophyll-*b* and pheopigments, *Limnol. Oceanogr.*, *39*(8), 1985-1992, <Go to ISI>://A1994QG41300020.

WETLabs (2011), ac meter protocol document, ac meter protocol (acprot); Revision Q 20 April 2011 (ed.).

Zaneveld, J.R.V., J.C. Kitchen and C.C. Moore (1994), Scattering error correction of reflecting-tube absorption meters, (ed.), *Proceedings*, doi: 10.1117/12.190095.

Zibordi, G. and K.J. Voss (2014), In situ Optical Radiometry in the Visible and Near Infrared, *Experimental Methods in the Physical Sciences*, *47*, 247-304.

Appendix

Table A- 1. Notations, descriptions and units if applicable.

Abbreviation	Description	Typical Units (if applicable)
A	Absorption coefficient	m^{-1}
a_{CDOM}	Absorption coefficient due to CDOM	m^{-1}
a_d	Absorption coefficient of detrital matter	m^{-1}
a_{nw}	Non-water absorption coefficient	m^{-1}
AOP	Apparent optical property	
a_p	Absorption due to particles	m^{-1}
a_{pg}	Absorption due to particles plus gelbstoff (detrital matter)	m^{-1}
a_{ph}	Phytoplankton pigment absorption coefficient	m^{-1}
a^*_{ph}	Chlorophyll-specific phytoplankton absorption coefficient	$m^2\ mg^{-1}$
a_t	Total absorption (all components)	m^{-1}
B	Scattering coefficient (in any/all directions)	m^{-1}
b_b	Backscattering (scattering in the backwards direction) coefficient	m^{-1}
b_{bp}	Particulate backscattering coefficient	m^{-1}
b_{bw}	Backscattering coefficient of pure water	
BRDF	Bi-directional reflectance distribution function	
C	Attenuation coefficient	m^{-1}
Cal/Val	Calibration and Validation	
CCNY	City College of New York	
CDOM	Chromophoric dissolved organic material	ppb
CEOS	Committee on Earth Observation Satellites	
Chl-*a*	Chlorophyll *a* concentration	$mg\ m^{-3}$
c_{nw}	Non-water attenuation coefficient	m^{-1}
CZCS	Coastal Zone Color Scanner instrument aboard the NIMBUS-7 satellite	
E_d	Downwelling irradiance	$mW\ cm^{-2}\ \mu m^{-1}$
EDIS	Environmental Data Information Service	
EDR	Environmental Data Record	
EDS	Environmental Data Service	
EPA	US Environmental Protection Agency	
E_s	Downwelling irradiance from above-water reference sensor	$mW\ cm^{-2}\ \mu m^{-1}$
ESSA	Environmental Science Services Administration	
EST	Eastern Standard Time	
FAFOV	Full Angle Field of View	
FEL	Lamp type designation assigned by the American National Standards Institute (not an acronym)	
F_L	Unknown spectral response calibration factor	
F_0	Extraterrestrial solar irradiance at mean Earth-Sun distance	$mW\ cm^{-2}\ \mu m^{-1}$
FOV	Field of view	
F_v/F_m	Photosynthetic efficiency	dimensionless
FWHM	Full width half maximum	
GCOM-C	Global Climate Observation Mission-Climate	
HPLC	High Pressure Liquid Chromatography	
IFCB	Imaging Flow CytoBot instrument (see Table B2)	
I_f	Immersion factor accounting for the change in responsivity of the sensor when immersed in water with respect to air	
I_i	integration time used for that reading	s
I_N	normalized integration time	s
INSITU-OCR	International Network for Sensor Inter-comparison and Uncertainty assessment for Ocean Color Radiometry	
IOCCG	International Ocean Colour Coordinating Group	
JPSS	Joint Polar Satellite System (program)	
JPSS-1; JPSS-2	Joint Polar Satellite System -1 -2 (future satellite missions)	
K_d	Downwelling diffuse attenuation coefficient	m^{-1}
K_{Lu}	Upwelling radiance diffuse attenuation coefficient	m^{-1}
L	Radiance	$mW\ cm^{-2}\ \mu m^{-1}\ sr^{-1}$
L_d	Downwelling radiance	$mW\ cm^{-2}\ \mu m^{-1}\ sr^{-1}$
LDEO	Lamont-Doherty Earth Observatory at Columbia University	
LISCO	Long Island Sound Coastal Observatory	
L_{ref}	Radiance of reference	$mW\ cm^{-2}\ \mu m^{-1}\ sr^{-1}$

Abbreviation	Description	Typical Units (if applicable)
L_{sky}	Radiance of sky	mW cm^{-2} μm^{-1} sr^{-1}
L_t	Total radiance	mW cm^{-2} μm^{-1} sr^{-1}
L_u	Upwelling radiance	mW cm^{-2} μm^{-1} sr^{-1}
$L_u(0^-, \lambda)$	Spectral upwelling radiance just below water surface	mW cm^{-2} μm^{-1} sr^{-1}
L_w	Water-leaving radiance	mW cm^{-2} μm^{-1} sr^{-1}
min	minutes	
MIN	Minimum	
MOBY	Marine Optical BuoY	
MSL12	Multi-Sensor Level-1 to Level-2 processing system	
N	number (count)	
n/a	Not available	
NASA	National Aeronautics and Space Agency	
NASA/GSFC	NASA/Goddard Space Flight Center	
NCEI	National Centers for Environmental Information	
NCOM	Navy Coastal Ocean Model	
NESC	National Environmental Satellite Center	
NESDIS	National Environmental Satellite, Data, and Information Service	
NESS	National Environmental Satellite Service	
NIR	Near infrared	
NIST	National Institute of Standards and Technology	
nL_w	Normalized water-leaving radiance	mW cm^{-2} μm^{-1} sr^{-1}
NOAA	National Oceanic and Atmospheric Administration	
NOAA/STAR	NOAA/Center for Science tech, algorithm, research	
NRL	Naval Research Laboratory	
NURADS	New Upwelling Radiance Distribution camera System	
n_w	Refractive index of seawater	
OCR-VC	Ocean Colour Radiometry Virtual Constellation	
OLCI	Ocean and Land Colour Instrument	
OMAO	Office of Marine and Air Operations	
OSU	Oregon State University	
PAR	Photosynthetically Active Radiation	
PI	Principal Investigator	
POC	Particulate Organic Carbon	mmol C m^{-3}
PON	Particulate Organic Nitrogen	mmol N m^{-3}
PSU	Practical salinity unit	g kg^{-1}
RFU	Relative fluorescence units	
R_g	Bi-directional reflectance of gray plaque	
R_{rs}	Remote sensing reflectance	sr^{-1}
R_{tile}	Reflectance of the NIST blue tile	
s/n	Serial number	
S	Radiometric spectrum measurement	
SeaWiFs	Sea-viewing Wide Field-of-view Sensor	
S_g	Radiometric spectrum measurement of gray plaque	
SGLI	Second Generation Global Imager	
SNPP	Suomi National Polar-orbiting Partnership	
S_{sfc}	Radiometric spectrum measurement of surface water	
S_{sky}	Radiometric spectrum measurement of sky	
SST	Sea surface temperature	°C
STARR	NIST Spectral tri-function automated reference reflectometer	
S_{tile}	Radiometric spectrum measurement of the NIST blue tile	
SPM	Suspended Particulate Material	mg L^{-1}
T	Time	s
U. Miami	University of Miami	
UMB	University of Massachusetts – Boston	
USF	University of South Florida	
USM	University of Southern Mississippi	
UTC	Coordinated Universal Time	
UV	Ultraviolet	
VIIRS	Visible Infrared Imaging Radiometer Suite	
β	Total volume scattering	m^{-1}

Abbreviation	Description	Typical Units (if applicable)
β_p	Particulate volume scattering	m^{-1}
$\Delta\phi$	Relative azimuth between the sun and the instrument viewing direction	°
$\Delta(\lambda)$	spectrally dependent scalar offset	
Λ	Wavelength	nm
ϕ_i	Scatter azimuth, incident	°
ϕ_r	Scatter azimuth, reflective	°
Φ	Relative azimuth of the sensor to the sun	°
P	Reflectance	Sr^{-1}
$\rho(\lambda, \theta)$	Fresnel reflectance factor of seawater	
θ	Angle	°
θ_g	Sensor zenith angle for gray plaque	°
θ_i	Sensor zenith angle, incident	°
θ_r	Sensor zenith angle, reflective	°
θ_{sfc}	Sensor zenith angle for water surface	°
θ_{sky}	Sensor zenith angle for sky	°
σ_{PSII}	Functional absorption cross-section of Photosystem II	$Å^2$ quanta^{-1} or 10^{-10} m^2 electron^{-1}
σ	Standard deviation	

Table A- 2. Instrument shorthand, description and manufacturer with modifications when applicable

Instrument Shorthand	Full Identification/Purpose	Manufacturer or Citation
ac-s	In situ spectrophotometer – high spectral resolution	WET Labs
ADCP	Acoustic Doppler Current Profiler	Teledyne RD Instruments
ALF	Advanced Laser Fluorometer	WET Labs
AlgaeOnlineAnalyser	Spectral fluorometer	bbe Moldeanke
ASD	Analytical Spectral Device; HandHeld2-Pro visible and near infrared spectrophotometer	Analytical Spectral Devices, Inc., a Malvern Panalytical company, Boulder, CO, USA.
BB3	Backscatter – 3 channels	
BB7FL2	Backscatter – 7 channels, Fluorescence – 2 channels	WET Labs
CTD	Conductivity, Temperature, Depth	Generic, various manufacturers
ECO BB9	Backscatter – 9 channels	WET Labs
DH4	Data logger	WET Labs
ECO-Puck Triplet Fluorometer	Fluorescence at 3 channels for determining chlorophyll, CDOM and phycoerythrin	WET Labs
ECO-Puck Triplet Scatterometer	Scatter – 3 channels (443, 550, 860)	WET Labs
FIRe	Variable fluorescence	Satlantic
FlowCam	Dynamic imaging particle analysis for species composition and size measurements	Fluid Imaging Technologies, Inc.
FRRF	Fast Repetition Rate Fluorometer	Generic
Garmin GPSMAP 78sc	Global positioning mapping instrument	Garmin International, Inc., Olathe, KS, USA.
GER	Field portable spectroradiometer	Spectra Vista Corporation, Poughkeepsie, NY, USA.
HyperOCI	Hyperspectral irradiance sensor	Satlantic LP
HyperOCR	Hyperspectral radiance sensor	Satlantic LP
HyperPro, HyperPro-II	Free-falling hyperspectral optical profiler	Satlantic LP
HyperTSRB	Hyperspectral radiometer configured to float on the sea surface	Satlantic LP
Imaging Flow CytoBot (IFCB)	Automated microscopic imaging instrument	McLane Research Labs
Microtops	Handheld sun photometer (atmospheric aerosols and optical depth)	Solar Light Company
NuRads	Upwelling Radiance Distribution Camera System	Voss and Chapin, 2005

RISBA	Radiometer Incorporating the Sky Blocking Approach	Lee et al. 2013
Sartorius CPA 2250	Balance	Sartorius
SBE 49	Conductivity, Temperature, Depth	SeaBird Scientific
Spectralon	White material (used for AWG reference plaques)	Labsphere, Inc., North Sutton, NH, USA.
Snapshot Hyperspectral Imager, UHD285	Above water snapshot imaging spectrometer	Cubert GmbH, Germany
SR1900 (Spectral Evolution)	Spectroradiometer, handheld	Spectral Evolution, Inc., Lawrence, MA, USA.
VSF-9	Volume scattering function – 9 channels	WET Labs
Zenith Light	White material (used for AWG reference plaques)	Sphere Optics GmbH, Herrsching, Germany